PRECIPITATION BEHAVIOUR AND ITS EFFECT ON MECHANICAL PROPERTIES OF ALLOY 693

By

SHABANA KHAN

Enrollment No: ENGG01200904050

Indira Gandhi Centre for Atomic Research, Kalpakkam

A thesis submitted to the
Board of Studies in Engineering Sciences
In partial fulfillment of requirements
for the Degree of

DOCTOR OF PHILOSOPHY

of

HOMI BHABHA NATIONAL INSTITUTE

February, 2019

Homi Bhabha National Institute

Recommendations of the Viva Voce Committee

As members of the Viva Voce Committee, we certify that we have read the dissertation prepared by **Shabana Khan** entitled "**Precipitation Behaviour and its Effect on Mechanical Properties of Alloy 693**" and recommend that it may be accepted as fulfilling the thesis requirement for the award of Degree of Doctor of Philosophy.

Chairman	**Prof. S. Banerjee**	Srikumar Banerjee	**Date:** 14 Jan 2019
Guide / Convener	**Prof. J.B. Singh**	JB Singh	**Date:** 14 Jan 2019
Examiner	**Prof. Satyam Suwas**	Satyam Suwas	**Date:** 14 Jan 2019
Member 1	**Prof. G.K. Dey**	Goutam Kumar Dey	**Date:** 14 Jan 2019
Member 2	**Prof. S.B. Roy**		**Date:** 14 Jan 2019
Member 3	**Prof. N.K. Maheswari**	Naresh Kr. Mahesh	**Date:**

Final approval and acceptance of this thesis is contingent upon the candidate's submission of the final copies of the thesis to HBNI.

I/We hereby certify that I/we have read this thesis prepared under my/our direction and recommend that it may be accepted as fulfilling the thesis requirement.

Date: 14/1/2019

Place: Mumbai

JB Singh

Prof. J.B. Singh

(Guide)

STATEMENT BY AUTHOR

This dissertation has been submitted in partial fulfilment of requirements for an advanced degree at **Homi Bhabha National Institute (HBNI)** and is deposited in the Library to be made available to borrowers under rules of the HBNI.

Brief quotations from this dissertation are allowable without special permission, provided that accurate acknowledgement of source is made. Requests for permission for extended quotation from or reproduction of this manuscript in whole or in part may be granted by the Competent Authority of HBNI when in his or her judgment the proposed use of the material is in the interests of scholarship. In all other instances, however, permission must be obtained from the author.

Shabana Khan

SHABANA KHAN

DECLARATION

I, hereby declare that the investigation presented in the thesis has been carried out by me. The work is original and has not been submitted earlier as a whole or in part for a degree / diploma at this or any other Institution / University.

Shabana Khan

SHABANA KHAN

LIST OF PUBLICATIONS ARISING FROM THE THESIS

International Journals

1. "Age hardening behaviour of Alloy 693", **S. Khan**, J.B. Singh, A. Verma; Materials Science and Engineering: A, 697 (2017) 86-94.

2. "Precipitation of a chromium-rich α-phase in Alloy 693 and its effect on tensile properties", **S. Khan**, J.B. Singh, A. Verma, M. Karri; Materials Science and Engineering: A, 686 (2017) 176-183.

3. "Lattice parameter instabilities during multi-phase precipitation in Alloy 693", **S. Khan**, S.D. Kaushik, A. Verma, J.B. Singh, V. Siruguri, D. Srivastava; Journal of Alloys and Compounds, 700 (2017) 149-154.

4. "Precipitation behaviour of γ' phase in Alloy 693", **S. Khan**, J.B. Singh, A. Verma; Materials Characterization, 119 (2016) 24-33.

Conference/Symposium

1. "Structure Property correlation of Alloy 693", **S. Khan**, J. B. Singh, J. K. Chakravartty-Poster presentation at EMSI 2015.

2. "Precipitation of γ' in Alloy 693 and its Effect on Mechanical Properties", **S. Khan**, J. B. Singh, A. Verma, J. K. Chakravartty - Oral presentation at NMD ATM 2014.

Shabana Khan

SHABANA KHAN

DEDICATIONS

Dedicated to SAM & My Brothers

ACKNOWLEDGEMENTS

I express my sincere gratitude to my Ph.D. guide Dr. J.B. Singh for his guidance and support throughout my dissertation work.

I am thankful to Homi Bhabha National Institute for giving me opportunity to register for Ph.D. and dean engineering sciences for administrative formalities.

I would like to pay my gratitude to committee chairman Dr. S. Banerjee (Chancellor HBNI, former AEC chairman), committee members Dr. G.K. Dey (former Director Materials Group, BARC), Dr. S.B. Roy (former Director Chemical Engineering Group, BARC) and Dr. N.K. Maheswari (Outstanding Scientist, Advanced Heavy Water Reactor Division, BARC) for their apt evaluation of my progress and for their invaluable suggestions during the course of my Ph.D.

I would like to pay my thankfulness to my Ph.D. thesis examiners for their valuable comments and suggestions, which were helpful to learn different nitty-gritties of my Ph.D. work. Recommendations about my Ph.D. thesis by them were gratefully appreciated.

I am thankful to Dr. J.K. Chakravartty (former Director Materials Group, BARC), Dr. M. Vijayalakshmi (former Associate Director Physical Metallurgy Group, IGCAR), and Dr. R. Divakar (Head Post Irradiation Examination Division, IGCAR) for their constant encouragement and support during my dissertation work.

I would like to express my gratitude to my colleague Dr. Amit Verma for his invaluable suggestions and discussions in my Ph.D.

I would also like to thank Dr. S. Neogy and Dr. Vishwanadh B. (Materials Group BARC, for microstructural characterization), Dr. V. Siruguri and Dr. S.D. Kaushik (UGC-DAE consortium for scientific research Mumbai centre BARC, for neutron diffraction studies), Dr. S.N. Achary (Chemistry Division BARC, for helping me to understand Rietveld refinement), Dr. Swain K.K., Ms. Avanti Singh, Ms. Smita S., Mr. Bhupesh and Mr. Chandramouleeswaran (Analytical Chemistry Division BARC, for chemical analysis), Mr. B.K. Kumawat, Mr. Shembe P.S., Mr. M. Pramod (Mechanical Metallurgy Division BARC, for tensile tests), Mr. Gaonkar K.B. (Post Irradiation Examination Division BARC, for Charpy tests), Mr. Hankare R.D. and Mr. Raju Rajagopalan R. (Materials Science Division BARC, for general help), Dr. B.C. Maji, Mr. Hatwar R.V., Mr. Shubham C., Mr. Senthil Kumar K.R. and Mr. Arjune M.T. (Glass & Advanced Materials Division BARC, for fabrication and sealing) & Mrs. Kailasa G.S. (Technical Physics Division, BARC, for coating my test samples).

I thankfully acknowledge the help, suggestions and cooperation given by my colleagues Dr. Rajeev Kapoor, Dr. P. Sengupta, Dr. Arpan Das, Dr. Apu Sarkar, Mr. A.K. Bind, Dr. A.N. Behera, Mr. Saurav Sunil, Mrs. Rumu B.H., Mr. Avinash G., Dr. Harshit K.K., Mr. Manoj Thota, and Mr. Sandeep K. during the course of my Ph.D. thesis.

I would also like to thank staff members of Dean Engineering Sciences Mr. Rajagopalan M., Ms. Suparna N.B. and Ms. Kishori K. as well as Mr. Rajeev P. from Committee chairman office for their help in fulfilling administrative formalities.

I sincerely express my gratitude towards my friends Twin, Raazi sir, Vandana Mum, Rajini Chaichi, Akshita Di, Shubhra Di, Girish and Arun K. Rai sir for their morale boosting words and support during the course of the work.

Finally, I am grateful to my parents and sisters for their immense support and love. Especially, the blessings of my parents have always shielded me from any difficulties during this journey. I owe special distinction to SAM and my brothers who stood behind me in all perspective and always encouraged me during ups and downs of my Ph.D. tenure.

All those whose mention might have missed by me, deserve my sincere gratitude for their direct or indirect help in this pursuit.

CONTENTS

SYNOPSIS

1. Introduction:

Alloy 693 is a newly developed precipitation hardened *Ni*-base superalloy. It is derived from the solid solution strengthened Alloy 690 by the addition of *Al, Ti* and *Nb* elements (see Table 1) [1, 2]. Presence of *Al* and *Ti* induces the formation of coherent ordered $L1_2$ type γ'-phase precipitates of $Ni_3(Al,Ti)$ stoichiometry in the γ-matrix (*fcc* structure). Addition of *Al, Ti* and *Nb* also improves corrosion, sulfidation and oxidation resistance, surface stability and mechanical strength of the alloy [3]. The alloy finds applications in places, such as, management of high level nuclear waste [4] and petrochemical processing industry [2]. It is also a candidate material for high temperature waste and biomass incinerators and for high temperature fuel cells involved in synthetic gas production (*e.g.,* fuel cells to power automobiles) and with potential to induce metal dusting [2].

2. Motivation:

Morphology and volume fraction of the hardening phase are important parameters which govern the strength of a precipitation hardened alloy. Morphology of γ'-precipitates is known to evolve continuously, from simple spherical to cuboidal and octocuboidal, and to complex structures, such as dendritic or octodendritic. Such morphological evolution occurs as anisotropic elastic strain energy starts dominating over the isotropic interfacial energy. Size of precipitates is another important parameter as the mechanism of strengthening depends upon it. When the size of γ'-precipitates is small, dislocations overcome precipitates by shearing them which requires additional energy to create extra surface during shearing. On the other hand, when the size of precipitates is large, additional stress is required to make dislocations expand and bend between particles. These changes, therefore, play important roles in deciding structural stability of *Ni*-base superalloys during service. Furthermore, multi component alloys like Alloy 693 are often designed on the basis of model systems and other (minor) elements are added to impart desired properties. However, addition of minor elements makes their overall composition rather complex, which may disturb equilibrium states of the model system and destabilize otherwise equilibrium phase. For instance, solubility of *Cr* in *Ni*-solid solution is found to decrease with addition of *Al* and *Ti* [5-8]. As mentioned earlier, since Alloy 693 is a modified version of Alloy 690, addition of *Al* and *Ti* in the latter may alter solubility of *Cr* in the former.

3. Objectives:

Aims of this dissertation are to study:

i) Precipitation behaviour of γ'-precipitates in Alloy 693.

ii) Microstructural stability of Alloy 693 at elevated temperatures.

iii) Room temperature mechanical properties of aged Alloy 693.

4. Experiment and Analysis:

Table 1 gives chemical composition of the alloy studied, which was within the range of nominal composition (also given in the Table 1) of an Alloy 693. Samples were isothermally annealed at 800-950°*C* temperatures for a series of time intervals ranging from 0.5-100*h* followed by water quenching. Prior to annealing, all samples were solution treated (*ST*) at 1100°*C* for 2.0*h* followed by water quenching to create same initial microstructure. All samples subjected to heat treatments were sealed in quartz ampoules filled with high purity *He* gas at a pressure of about 150*mm* of *Hg*. Phase identification and microstructural characterization were carried out using *X*-ray diffraction (*XRD*), scanning electron microscope (*SEM*) and transmission electron microscope (*TEM*), respectively. Chemical compositions of phases were determined using energy dispersive spectroscopy (*EDS*) analysis employing Oxford spectrometers attached to electron microscopes.

Table 1. Chemical composition (*wt.%*) of Alloy 690 and Alloy 693[1, 2].

Ni	*Cr*	*Fe*	*Al*	*Nb*	*Mn*	*Ti*	*C*	*S*	*N*
Nominal Composition of Alloy 690									
Bal.	27-31	7-11	-	-	0.5 *max.*	-	0.05 *max.*	0.015 *max.*	-
Nominal Composition of Alloy 693									
Bal.	27-31	2.5-6.0	2.5-4.0	0.5-2.5	1.0 *max.*	1.0 *max.*	0.15 *max.*	0.01 *max.*	-
Composition of Alloy 693 under study									
58.42 ±2.92	31.26 ±1.56	3.98 ±0.20	3.94 ±0.20	1.53 ±0.08	0.20 ±0.01	0.34 ±0.02	0.083± ($1.38x10^{-4}$)	0.006± ($6x10^{-4}$)	0.015± ($7.5x10^{-4}$)

Sample preparation for microstructural characterization was carried out by polishing samples on different grades of *SiC* papers (up to 2400 grit size) followed by final surface polishing using oxide polishing suspension. γ'-precipitates were revealed by electrochemical etching of polished samples at room temperature using $5V$ *DC* voltage and a solution containing 8*g* CrO_3 and 5*ml* H_2SO_4 in 85*ml* H_3PO_4 acid. Size of precipitates were measured using the freeware image analysis software *ImageJ* [9]. *TEM* specimens were prepared by thinning samples up to about 100μm thickness and punching out 3*mm* discs from thinned foils. 3*mm* discs were then electropolished to perforation using *DC* voltage of about $20V$ in a dual jet Tenupol electro-polishing unit using an electrolyte containing 20% perchloric acid ($HClO_4$) in ethanol (C_2H_5OH) maintained at about -40°*C* temperature. Second phase particles mainly comprised of carbides and α-phase particles were electrolytically extracted out of the bulk samples by selective dissolution of the matrix in an electrolyte solution containing 10% *HCl* and 1% tartaric acid in methanol using $15V$ *DC* voltage and 1*A* current at about 5°*C* temperature [10]. Microhardness measurements were carried out using a Vicker's hardness tester with a load of 1.0*kgf* for a dwell time of 10*s*. Reported microhardness values are averages of 10 independent readings for each measurement. Room temperature tensile properties were evaluated using round tensile specimens (*M 8*.0 x 1.*25*) of 4.0*mm* diameter and about 20*mm* gauge length as per *ASTM E8* standard [11] in an Instron (Model-1185) machine, using a constant strain rate of $0.98 \times 10^{-4} s^{-1}$. Sub-sized *V*-notch specimens as per *ASTM E23* standard [12] were used for impact energy studies. Reported tensile and impact properties are averages for two independent tensile and impact tests for each sample condition. Fractography of the fractured surfaces were carried out using *SEM*. Microstructural modifications during deformation were studied in-situ during deformation of tensile samples inside the SEM using a Kammrath and Weiss microtest stage. In-situ tensile experiments were carried out using 1.0*mm* thick flat tensile samples of gauge dimensions 5.0*mm* x 25*mm* at a strain rate of $4.0 \times 10^{-4} s^{-1}$.

5. Results and Discussion:

5.1. Precipitation behaviour of γ'-precipitates in Alloy 693 :

ST-alloy exhibited the presence of fine precipitates (~10*nm*) of γ'-phase distributed homogeneously within matrix (Figure 1), which was in agreement with results reported earlier by Singh et *al.* [13] for a similar alloy. These precipitates grew and/or coarsened during ageing whose temporal evolution at temperatures from 800-950°*C* for 0.5, 2.0 and 100*h* is shown in Figure 2.

Average sizes of γ'-precipitates at different temperatures and times are given in Table 2, where as their number density (ρ) and volume fractions (f) are given in Table 3. At 800°*C*, samples exhibited nearly fixed number density of γ'-particles but their volume fraction increased monotonically indicating the particles remained in the growth stage till 100*h* at this temperature (see Figure 2(a) –2(c)).This behaviour was also consistent with the increase of hardness and yield strength (*YS*) at this temperature presented later. Precipitates remained spherical during the entire ageing period at this temperature. At higher temperatures, precipitates grew to larger sizes (Table 2) and tend to change their morphologies to cuboidal having their facets approximately parallel to {100} planes (Figure 2), which is known for these particles [14, 15].

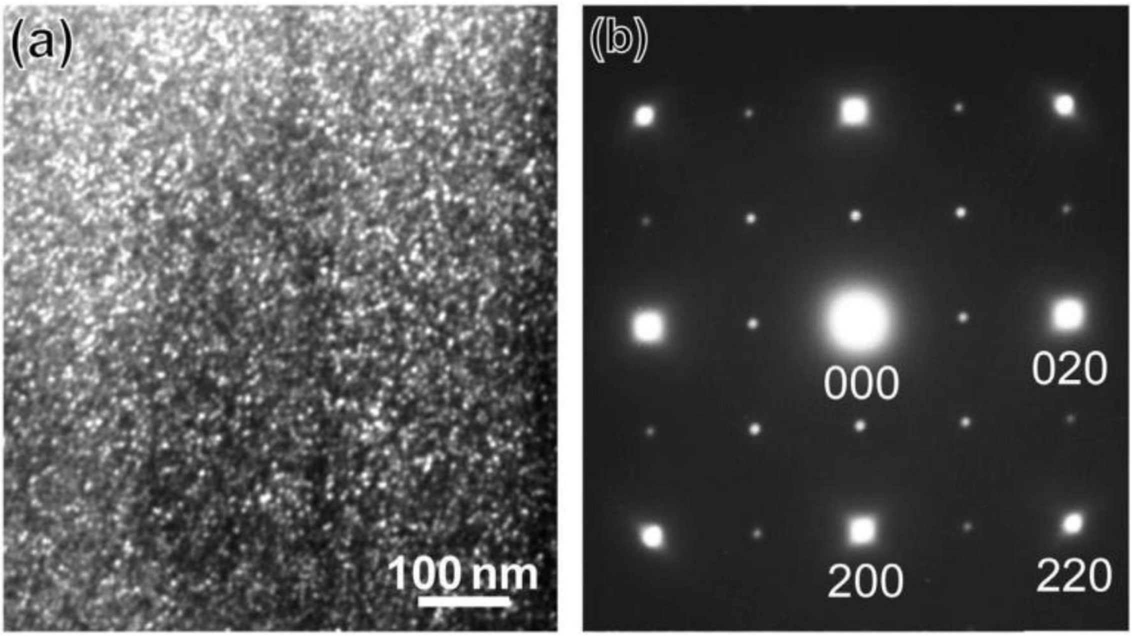

Figure 1.(a) Dark field *TEM* micrograph of *ST*-sample, showing distribution of fine γ'-precipitates; (b) *SAED* pattern along [001] zone axis, showing characteristic superlattice reflections of γ'-precipitates at {100} and {110} positions.

At these temperatures number density (ρ) of precipitates reduced with ageing as well as temperature (Table 3), which could be attributed to coarsening of precipitates [16]. Alloy aged at 875°*C* exhibited almost constant values of f though the values of ρ decreased with time, suggesting of coarsening stage of precipitates at this temperature. Interestingly, samples aged at 900°*C* and 950°*C* temperatures exhibited higher values of f initially which reduced to stabilize at lower values after certain time (Table 3). Reduction in volume fraction of precipitates could be attributed to under-saturated state of the γ-matrix (with respect to γ'-forming solutes) at these temperatures. Due to under-saturated state of the γ-matrix, dissolution of γ'-phase precipitates, that were already present in the starting microstructure, would take place and dissolve till composition of the γ-matrix saturates at respective temperatures. This was confirmed on the basis of variation in lattice parameter of the γ-matrix during isothermal annealing at these temperatures and has already been reported [17]. Fixed volume fraction of precipitates, concomitant with decrease in their number density, after 2.0*h* of ageing at 950°*C* indicated of their coarsening stage. Attempts were also made to delineate growth and coarsening stages of γ'-precipitates on the basis of change in lattice parameter of the γ-phase. However, this data could not be utilized due to the precipitation of an α-phase, which also decreased lattice parameter of the matrix [18], during periods that overlapped with coarsening stages of γ'-precipitates. Precipitation behaviour of the α-phase is discussed in Section 5.2.

Table 2. Average sizes of γ'-precipitates in aged specimens.

Time (*h*)	**Average size of γ'-precipitates (*nm*)**			
	800°*C*	**875°*C***	**900°*C***	**950°*C***
0.5	8.3 ± 2.3	24.1 ± 8.5	27.9 ± 9.2	43.9 ± 10.0
2.0	18.5 ± 6.8	41.5 ± 10.1	47.0 ± 13.5	78.3 ± 17.1
100.0	81.2 ± 21.4	152.9 ± 43.1	203.2 ± 5.6	341.2 ± 4.2

Table 3. Number density (ρ) and volume fraction (f) of γ'-precipitates in aged specimens.

Time (*h*)	**No. density of γ'-precipitates (ρ -number.nm^{-2}); volume fraction (f)**							
	800°*C*		**875°*C***		**900°*C***		**950°*C***	
	$\rho*10^{-4}$	f	$\rho*10^{-4}$	f	$\rho*10^{-4}$	f	$\rho*10^{-4}$	f
0.5	6.79	0.52±0.04	2.38	0.49±0.04	1.54	0.43±0.04	0.85	0.32±0.02
2.0	7.02	0.53±0.07	1.57	0.50±0.04	1.21	0.43±0.05	0.30	0.19±0.03
100.0	7.05	0.78±0.04	0.09	0.62±0.09	0.05	0.37±0.05	0.01	0.19±0.03

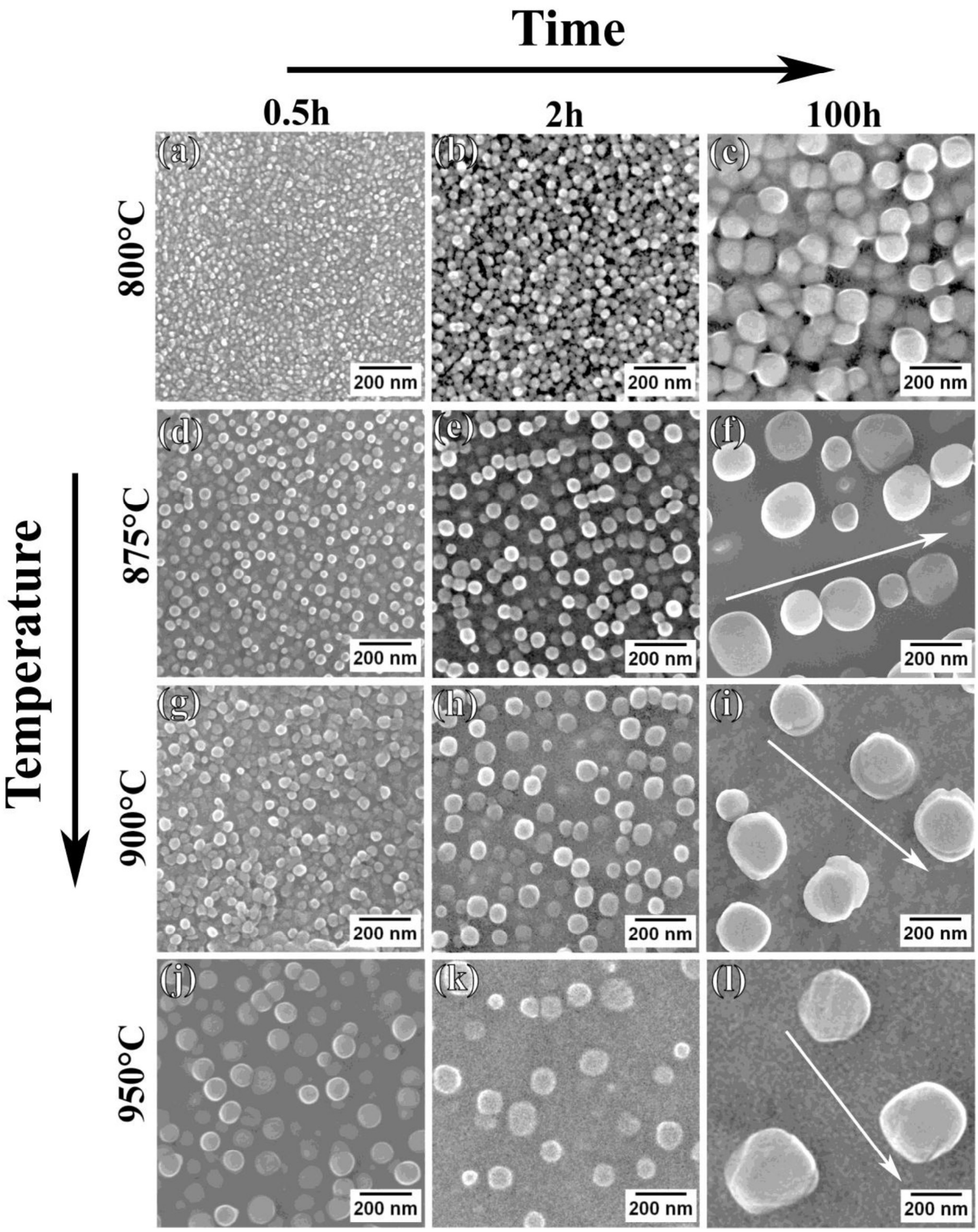

Figure 2: *FEG-SEM* micrographs, secondary electron images depict temporal evolution of γ'-precipitates during isothermal ageing at temperatures ranging from 800 to 950°*C*: (a) 0.5*h* at 800°*C*; (b) 2.0*h* at 800°*C*; (c) 100*h* at 800°*C*; (d) 0.5*h* at 875°*C*; (e) 2.0*h* at 875°*C*; (f) 100*h* at 875°*C*; (g) 0.5*h* at 900°*C*; (h) 2.0*h* at 900°*C*; (i) 100*h* at 900°*C*; (j) 0.5*h* at 950°*C*; (k) 2.0*h* at 950°*C*; (l) 100*h* at 950°*C*.

Coarsening of γ'-precipitates was found to follow a matrix diffusion controlled growth behavior , $r^3 = K.t$, where r is the average radius of precipitates at ageing time t and K is constant, in agreement with Lifshitz-Slyozov-Wagner (*LSW*) theory [19, 20]. During coarsening, morphology of precipitates appeared to change from spherical to cuboidal and they tended to align themselves along directions marked by arrows (see Figure 2(f, i, l)), which are elastically soft <100> directions [14]. This was consistent with other studies on γ'-precipitates bearing superalloys [21, 22] and has been associated with the dominance of interfacial energy over elastic strain energy during later stages of transformation [23].

5.2. Microstructural stability of Alloy 693 at elevated temperatures:

Alloy exhibited a phase separation tendency at higher temperatures to form a *Cr*-rich α-phase (*bcc* structure) along with γ'-phase. Volume fraction of this phase appeared to increase with ageing temperature as well as time. Figure 3(a-c) shows *SEM* micrographs depicting evolution of the α-phase within ($\gamma+\gamma'$)-phase regions during isothermal annealing at 950℃. The α-phase initially had a lath morphology but later transformed into a needle shape. α-precipitates were always enveloped by regions depleted in chromium but enriched with aluminum with respect to the surrounding matrix (Figure 3d). Aluminum enrichment could be attributed to its rejection from α-forming regions. Chemical composition of α-precipitates was found to be 95*Cr*-3.1*Ni*-1.9*Fe* (in *at.%*) on the basis of *EDS* analysis of extracted α-phase precipitates (shown in Figure 3(e)).

XRD analysis of extracted α-phase particles confirmed their body centered cubic (*bcc*) crystal structure. *TEM* analysis of α-precipitates was consistent with *XRD* results. Figure 4(a) depicts a region of a grain containing γ- and γ'-phases within which α-phase precipitates surrounded by the enveloped phase designated as 'e_p-phase' had formed. Figure 4(b) shows composite *SAED* pattern taken from α- and e_p-phases (from encircled region in Figure 4(a)), and a key to Figure 4(b) is shown in Figure 4(c). Presence of superlattice reflections of γ'-

phase at {100} and {110} positions in *SAED* suggested that the enveloped region (e_p-phase) contained a mixture of γ_d- and γ'_d- phases (subscript '*d*' is used to represent that chemical compositions of the γ_d- and γ'_d- phases were different from those of otherwise mentioned γ- and γ'-phases due to the formation of former in chromium depleted regions). However, γ'-particles within the enveloped region could not be resolved by dark-field *TEM* imaging suggesting of their smaller sizes. Nonetheless, mottled contrast observed within the enveloped region in the bright-field image (see Figure 4(a)) was consistent with the presence of fine γ'-precipitates in it. TEM analysis also established a Kurdjumov-Sachs (*KS*) type orientation relationship (*i.e.*, $(111)_\gamma \| (110)_\alpha$ and $[\bar{1}10]_\gamma \| [\bar{1}11]_\alpha$) between α-phase and the surrounding matrix [18]. Formation of the α-phase has been explained on the basis of thermodynamic stability of phases involved [24].

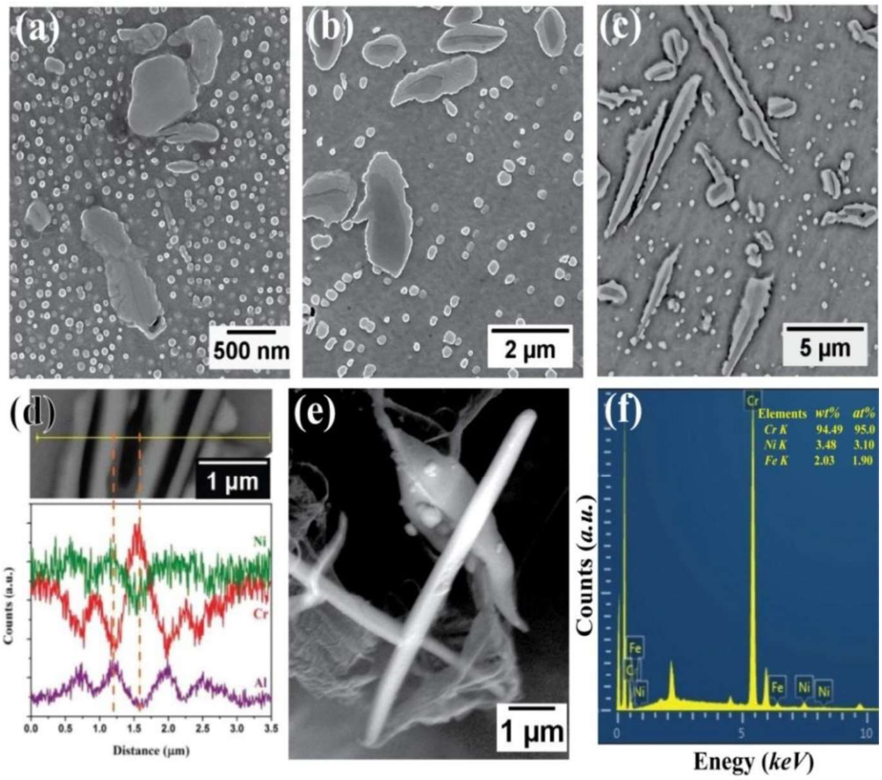

Figure 3. *SEM* micrographs depicting temporal evolution of needle shape particles in Alloy aged at 950°*C* for: (a) 0.5*h*; (b) 20*h*; (c) 100*h*; (d) *EDS* line scan over the needle particles; (e) secondary electron image of extracted needle particles; and (f) *EDS* spectrum from an extracted particle.

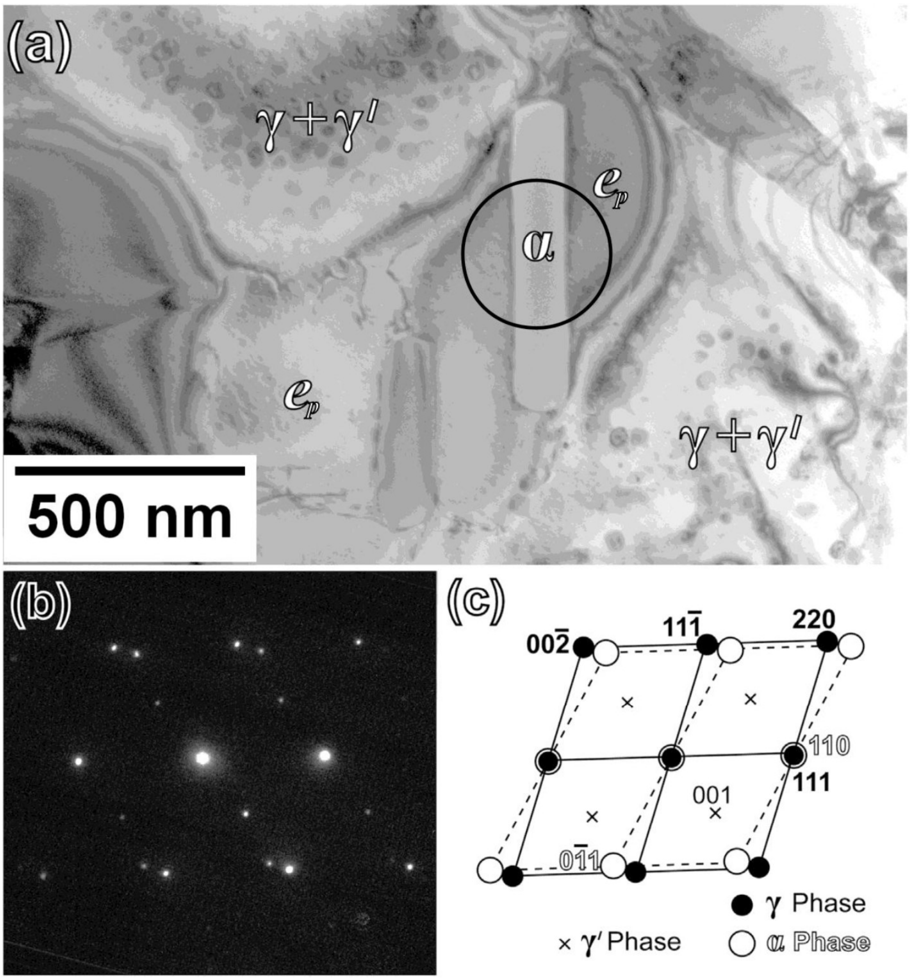

Figure 4. (a) Bright field *TEM* micrograph of sample aged at 950°*C* for 100*h*. Different phases, namely α, e_p, γ' and γ are marked in the figure. (b) *SAED* pattern taken from an encircled region containing α- and e_p-phases. This diffraction pattern could indexed as a superimposed diffraction pattern corresponding to $[\bar{1}10]_\gamma$ // $[\bar{1}11]_\alpha$ zone axes of γ- and α-phases (see key to (b) in (c)). Superlattice reflections of the γ'-phase, at {100} and {110} could also be noticed.

5.3. Effect of precipitation on mechanical properties of the alloy:

Effect of precipitation behaviour on mechanical properties of the alloy was understood on the basis of combined studies of hardness values, tensile properties and Charpy energies of samples tested at room temperature.

5.3.1. Effect of γ'-precipitation:

Precipitation of γ'-precipitates had a pronounced effect on hardness and tensile properties of the alloy. *ST*-alloy exhibited hardness value of 253.8±7.4*Hv*, which was attributed to the presence of fine γ'-precipitates in the γ-matrix (Figure 1). Corresponding yield strength and ductility (measured as total percentage elongation) were about 400*MPa* and 44%, respectively.

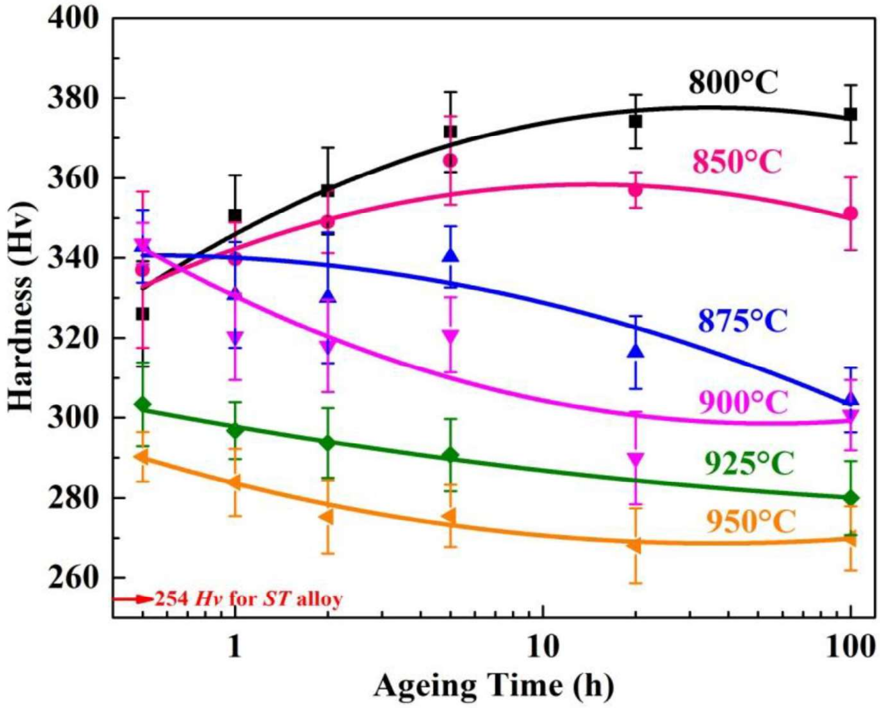

Figure 5. Variation in hardness with ageing time (0.5-100*h*) for alloys aged at 800-950°*C*temperatures.

Samples aged at 800°*C* and 850°*C* exhibited *a* monotonous increase in hardness and strength with concomitant decrease in ductility with ageing time (Figures 5 and 6(a)). Impact energies of aged samples were consistent with decreasing ductility trend with ageing time. The hardness value tended to reach a plateau during prolonged ageing. This behaviour could be rationalized on the basis of continuous growth and precipitation of γ'-phase particles observed at 800°*C* (Figure 2). Hardness and strength of alloy aged at 875-950°*C* temperatures first increased up to $0.5h$ ageing followed by a monotonous decrease till a plateau is reached (Figures 5 and 6(b-d)). Initial increase in strength could be correlated with increase in volume fraction of γ'-particles due to growth of fine γ'-particles present in starting ST-alloy. Beyond $0.5h$ of ageing, coarsening of γ'-particles resulted in decrease in hardness/strength of alloy [25, 26]. Interestingly, alloy did not exhibit concomitant increase in ductility as normally observed with decrease in strength due to particle coarsening and found to lose its ductility. This unusual drop in ductility was attributed to the precipitation of α-phase, which precipitated out during coarsening periods of γ'-precipitates.

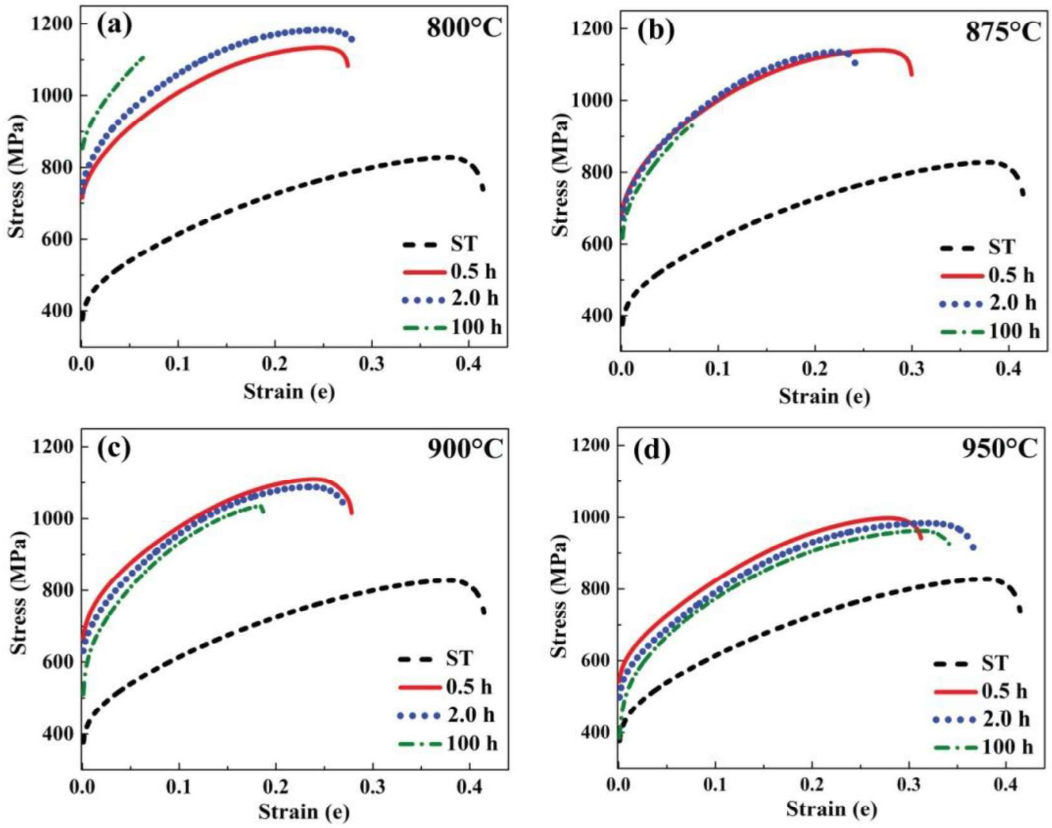

Figure 6. Room temperature engineering stress versus engineering strain behaviour of Alloy 693 in solution treated state as well as after ageing for 0.5, 2.0 and $100h$ at temperatures ranging from $800°C$ to $950°C$: (a) at $800°C$; (b) at $875°C$; (c) at $900°C$; (d) at $950°C$.

5.3.2. Effect of α-phase precipitation:

Precipitation of the α-phase particles appeared to have reduced ductility of alloy. This was supported by fractography of fractured surfaces, which revealed the presence of many particles that had broken (cleaved) during deformation (see marked in Figure 7).

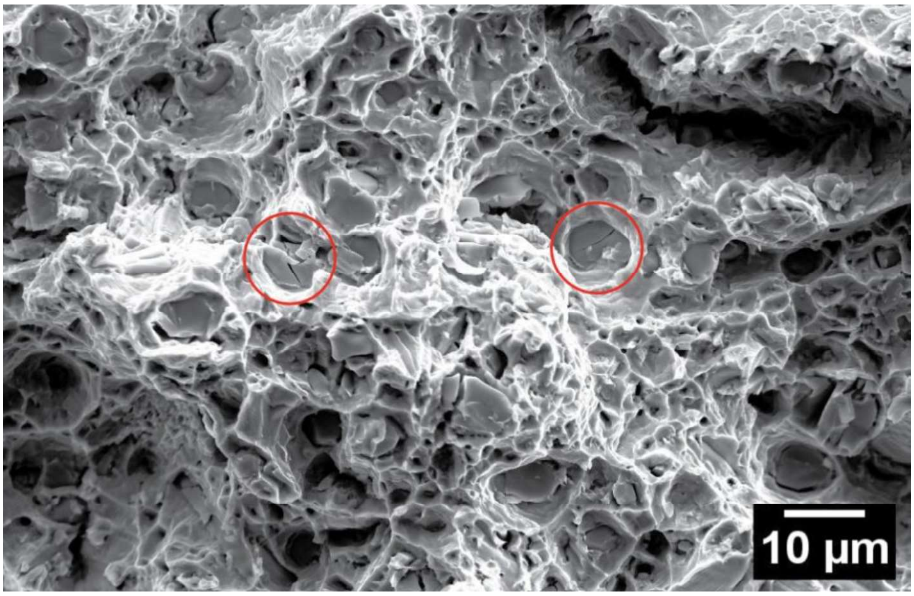

Figure 7. *SEM* fractograph of fractured surface of room temperature tensile tested sample aged at 950°*C* for 100*h* (broken particles are marked).

EDS analysis of broken particles confirmed them to be *Cr*-rich. Brittle nature of α-precipitates was further confirmed by in-situ examination of an aged sample (950°*C*-100*h*) inside *SEM* during straining. In-situ straining experiment confirmed the development of cracks within α-phase particles within about 3% straining. This was found to be consistent with the brittle nature of *Cr*, whose maximum strength at room temperature is reported to be 282*MPa* with nil ductility [27], which was lower than yield strength of aged alloy. Appearance of internal cracks due to fracture of α-precipitates would limit the ductility and promote easy fracture.

5.3.3. Mechanisms responsible for strengthening of aged Alloy 693:

Strengthening by ordered particles can be attributed to three mechanisms depending upon their size and volume fractions: (i) shearing by pairs of weakly coupled dislocations (*WCDs*); (ii) shearing by pairs of strongly coupled dislocations (*SCDs*); and (iii) Orowan looping. Among these three mechanisms the one with the least critical resolved shear stress (*CRSS*) value would be active.

Owing to continuously changing microstructural condition of aged alloy, the active mechanisms were identified on the basis of comparison of theoretical estimation of the *CRSS* for above mentioned mechanisms when the alloy contained the varying volume fraction of particles of different sizes (considered upto 350*nm*). Representative plots of theoretically estimated *CRSS* values [17] for three competing mechanisms for different volume fractions, f = 0.2, 0.55 and 0.8 of particles are shown in Figure 8. From Figure 8 (a) it was evident that, for lower volume fractions of precipitates (*i.e.*, $f \leq 0.20$) shearing by *WCDs* was the main operative mechanism till particles grew up to an average size of 50*nm* beyond which the Orowan bowing would dominate. However, for $f > 0.20$ (Figure 8(b-d)), shearing by *SCDs* would dominate until particles became very large in size at which Orowan bowing would become active. Size of particles beyond which the Orowan mechanism would become active was quite sensitive of volume fraction of particles. For $f = 0.50$ (Figure 8(b)), Orowan mechanism would dominate only when the size of particles d >250*nm*, while it would dominate for d > 350*nm* if the volume fraction is increased to 0.55 (Figure 8(c)). On the basis of this analysis, it could be concluded that, when the volume fraction is low, for example, $f <$ 0.20 (Figure 8(a)), *WCDs* mechanism of shearing of small particles would be directly taken over by the Orowan looping when particles grew beyond 50*nm*.

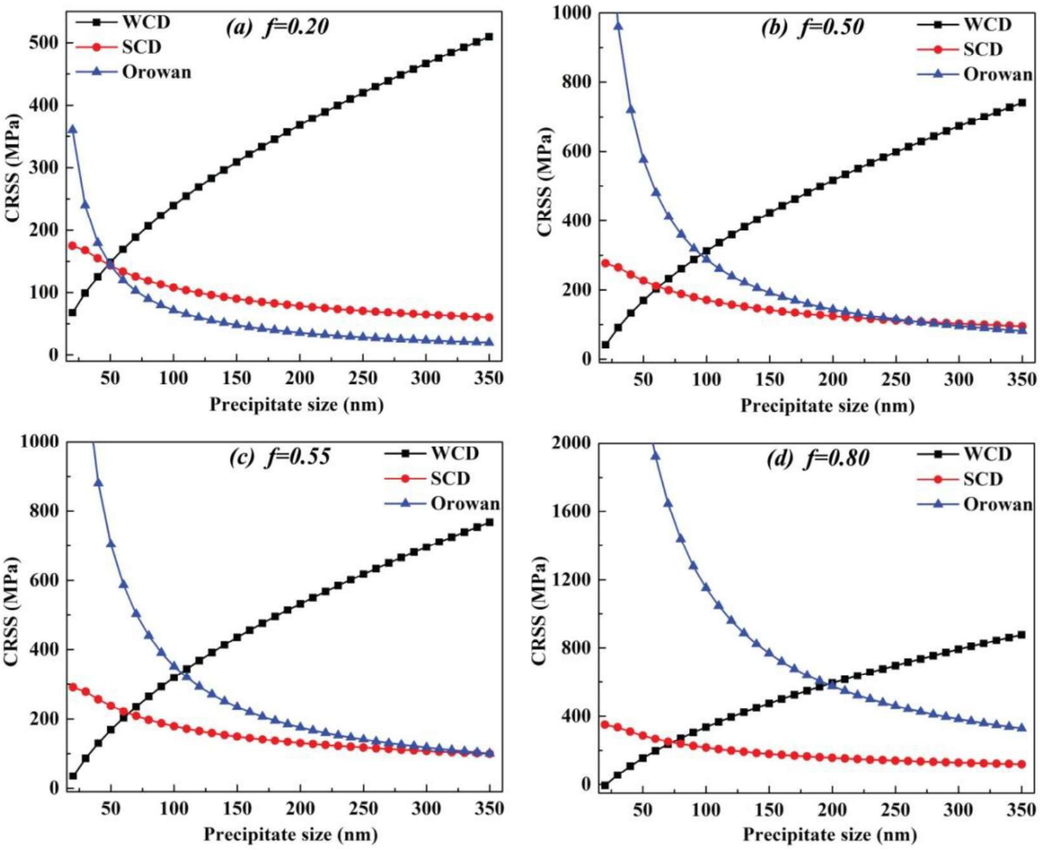

Figure 8. Shows variation in empirically calculated *CRSS* values as a function of precipitate size for competing strengthening mechanisms involving shearing by weakly coupled pairs of dislocations, shearing by strongly coupled pairs of dislocations and Orowan bowing. Figure shows representative plots for volume fraction: (a) f =0.2; (b) f =0.50; (c)f =0.55and (d) f =0.8.

Table 4. Empirically identified strengthening mechanisms, to be active in alloys with different ageing treatments.

Alloy state	**Ageing Time (*h*)**		
Aged Temperature (°*C*)	**0.5**	**2.0**	**100**
800	*WCD*	*WCD*	*SCD*
875	*WCD*	*WCD*	*SCD*
900	*WCD*	*WCD*	*Orowan*
950	*WCD*	*Orowan*	*Orowan*

However, when the volume fraction is large (Figure 8(b-d)), shearing by *SCDs* would dominate mostly. The minimum size of particles beyond which Orowan looping mechanism would dominate over shearing by *SCD* would increase with increase in volume fraction of particles. Though for very larger volume fraction strengthening would be practically always governed by *SCD* mechanism of shearing (Figure 8(d)). On the basis of this analysis, active mechanisms of hardening in different aged alloys were identified and are listed in Table 4.

5.3.4. Work hardening behaviour of Alloy 693:

In general, strain hardening arises due to obstacles in the path of dislocation motion. These obstacles can be grain boundaries, subgrain boundaries, dislocation tangles, second phase particles, etc. Lattice misfit (ϵ) between matrix and second phase would also indirectly affect work hardening properties of alloys as stress required for the passage of dislocations across precipitate/matrix interfaces would depend on it. Hence, overall work hardening in an alloy with complex microstructure would be a net result of factors mentioned above.

In the present case, work hardening is considered to have occurred mainly due to γ'-precipitates. This behaviour was analyzed on the basis of strain hardening exponent (n) obtained by fitting experimentally observed true stress (σ_t)–true plastic strain (ε_t) flow curves to work hardening relationships [28-32], which establish analytical relationship between true stress (σ_t) and true strain (ε_t). Based on the goodness of fit (sum of residual squares-χ^2 values), flow relationship is chosen, and Ludwik flow relationship [30] gave best fit out of all relationships. Ludwik relationship is given by: $\sigma = \sigma_0 + \kappa.\varepsilon_t^n$, where, σ_0 is true stress at $\varepsilon_t = 0$ and κ is a constant called strength factor. Fitted values of σ_0, κ and n are given in Table 5. *ST*-alloy containing fine γ'-particles exhibited highest value of n, which was close to values reported for other *Ni*-base superalloys hardened by similar sized coherent particles [33]. These particles were characterized by easy shearing by dislocations and provide low resistance shear bands for subsequent dislocations. High value of n in such cases could thus be attributed to dislocation-dislocation interactions within these bands. Value of n decreased in aged alloys. In general, n value decreases as volume fraction (f) increases for a given particle size (d), and it decreases with decreasing d when f is fixed. However, in the present work, f and d both changed simultaneously in most of the cases (Tables 2 and 3). Above arguments are therefore not valid when microstructures changes continuously. For such cases, Zhang et *al*. [34] have demonstrated that the inter-particle spacing (λ) relates better to n as the value of n increases linearly with increase in λ, irrespective of volume fraction. Observed values of n in aged samples were thus in conformity with Zhang et *al.* in most of the cases. Deviations observed in some cases, as in samples aged for long durations at 900$°C$ and 950$°C$, could be attributed to the precipitation of α-phase precipitates. Precipitation of α-precipitates appeared to have reduced value of n. This effect was evident when one compares hardening behaviour of sample aged at 950$°C$ for 0.5h with that of sample aged at 900$°C$ for 100h. Volume fractions of γ'-precipitates in two samples were nearly similar (Table 3), while average sizes of particles are about 45nm and 203nm, respectively (Table 2). The observed values of n for the two cases were 0.77 (950$°C$-0.5h) and 0.62 (900$°C$-100h) (Table 5), while it was expected to be higher for the later. This variance of observed values could be attributed to the presence of α-particles in the 900$°C$-100h as that is the only other difference between two microstructures. Decrease in hardening coefficient due to the presence of α-particles could be related to their brittle nature, shown earlier. These particles acted as crack initiation sites, which would limit the strength of the material. During deformation tearing of these particles take place away from the matrix.

Table 5. Work hardening parameters obtained by fitting *RT* flow stress curves of alloys with different ageing treatments to Ludwik equation [30].

Alloy state		Work hardening parameters		
Ageing temperature (°*C*)	**Ageing time (*h*)**	σ_0 **(*MPa*)**	κ **(*MPa*)**	***n***
ST		411.81	1930.12	0.84
800	**0.5**	707.24	2053.62	0.69
	2.0	724.94	2036.40	0.65
	100.0	846.18	2620.43	0.74
875	**0.5**	676.88	2047.38	0.68
	2.0	665.71	2176.36	0.67
	100.0	615.85	2204.51	0.66
900	**0.5**	676.74	2117.33	0.71
	2.0	614.98	2111.27	0.67
	100.0	518.21	2141.67	0.61
950	**0.5**	554.32	2173.56	0.77
	2.0	496.64	2084.32	0.72
	100.0	437.72	1982.08	0.64

6. Conclusion:

i. Precipitation and coarsening behaviour of γ'-precipitates in Alloy 693 followed a behaviour similar to other γ'-precipitate bearing alloys [21, 22, 26, 35, 36]. Precipitates always maintained coherency with the matrix.

ii. The alloy exhibited a tendency to phase separation and formed a chromium rich α-phase at elevated temperatures. The α-phase maintained a Kurdjumov-Sachs type orientation relationship-$(111)_\gamma \| (110)_\alpha$ and $[\bar{1}10]_\gamma \| [\bar{1}11]_\alpha$ with γ-matrix.

iii. Precipitation of γ'-particles enhance strength of alloy significantly. The alloy exhibited anomalous decrease in ductility during coarsening of γ'-particles, which was attributed to Cr-rich α-particles that precipitated during γ'-particles coarsening period. Ageing of the alloy at $875°C$ for $0.5h$ gave best combination of strength and ductility.

iv. Precipitation of the Cr-rich α-phase embrittled the alloy as its precipitates acted as sites for easy crack initiation due to their inherent brittle nature.

7. Future Work:

- ✓ Mechanical properties studies of the Alloy 693 at high temperatures.
- ✓ Corrosion studies of aged Alloy 693 in different environment.
- ✓ Slow strain rate testing (*SSRT*) to evaluate the susceptibility of the alloy against environmental cracking.
- ✓ Creep behaviour of Alloy 693.

8. References:

[1] http://www.specialmetals.com/assets/documents/alloys/inconel/inconel-alloy-690.pdf.

[2] http://www.specialmetals.com/assets/documents/alloys/inconel/inconel-alloy-693.pdf.

[3] J. H. Hsu, J. W. Newkirk, C. W. Kim, C. S. Ray, R. K. Brow, M. E. Schlesinger, D. E. Day, "Corrosion of Inconel 690 and Inconel 693 in an iron phosphate glass melt", Corrosion Science, 75 (2013) 148-157.

[4] D. Zhu, C. W. Kim, D. E. Day, "Corrosion behavior of Inconel 690 and 693 in an iron phosphate melt", Journal of Nuclear Materials, 336 (2005) 47-53.

[5] A. Taylor, R.W. Floyd, "The constitution of nickel-rich alloys of the nickel chromium aluminium system", Journal of the Institute of Metals, 81 (1952-1953) 451-464.

[6] D. West, "Ternary equilibrium diagrams", Springer Science & Business Media, (1982) 94-99.

[7] N. Dupin, I. Ansara, B. Sundman, "Thermodynamic re-assessment of the ternary system Al-Cr-Ni", Calphad, 25 (2001) 279-298.

[8] L. Kaufman, H. Nesor, "Calculation of superalloy phase diagrams: Part I", Metallurgical Transactions, 5 (1974) 1617-1621.

[9] http://rsbweb.nih.gov/ij/.

[10] R.C. Reed, M.P. Jackson, Y.S. Na, "Characterization and modeling of the precipitation of the sigma phase in UDIMET 720 and UDIMET 720Li", Metallurgical and Materials Transactions A, 30 (1999) 521-533.

[11] ASTM E8M-04, "Standard Test Methods for Tension Testing of Metallic Materials", ASTM International, West Conshohocken PA , USA (2004).

[12] ASTM E23-05, "Standard Test Methods for Notched Bar Impact Testing of Metallic Materials", ASTM International, West Conshohocken PA , USA (2005).

[13] J.B. Singh, A. Verma, M.K. Thota, J.K. Chakravartty, "Brittle failure of Alloy 693 at elevated temperatures", Materials Science and Engineering: A, 616 (2014) 88-92.

[14] Shabana Khan, J.B. Singh, A. Verma, "Precipitation behaviour of γ′ phase in Alloy 693", Materials Characterization, 119 (2016) 24-33.

[15] R.C. Reed, "The superalloys: fundamentals and applications", Cambridge university press, (2008) 33-120.

[16] D.A. Porter, K.E. Easterling, Phase Transformations in Metals and Alloys, (Revised Reprint), VNR International, 1989, p. 46.

[17] Shabana Khan, J.B. Singh, A. Verma, "Age hardening behaviour of Alloy 693", Materials Science and Engineering: A, 697 (2017) 86-94.

[18] Shabana Khan, J.B. Singh, A. Verma, M. Karri, "Precipitation of a chromium-rich α-phase in Alloy 693 and its effect on tensile properties", Materials Science and Engineering: A, 686 (2017) 176-183.

[19] I.M. Lifshitz, V.V. Slyozov, "The kinetics of precipitation from supersaturated solid solutions", Journal of Physics and Chemistry of Solids, 19 (1961) 35-50.

[20] C. Wagner, "Theorie der Alterung von Niederschlägen durch Umlösen (Ostwald-Reifung)", Zeitschrift für Elektrochemie, Berichte der Bunsengesellschaft für physikalische Chemie, 65 (1961) 581-591.

[21] R.A. Ricks, A.J. Porter, R.C. Ecob, "The growth of γ′ precipitates in nickel-base superalloys", Acta Metallurgica, 31 (1983) 43-53.

[22] M. Doi, T. Miyazaki, "γ′ precipitate morphology formed under the influence of elastic interaction energies in nickel-base alloys", Materials Science and Engineering, 78 (1986) 87-94.

[23] S. Meher, S. Nag, J. Tiley, A. Goel, R. Banerjee, "Coarsening kinetics of γ′ precipitates in cobalt-base alloys", Acta Materialia, 61 (2013) 4266-4276.

[24] S.M. Merchant, M.R. Notis, "A review: Constitution of the Al-Cr-Ni system", Materials Science and Engineering, 66 (1984) 47-60.

[25] S. Zhao, X. Xie, G.D. Smith, S.J. Patel, "Microstructural stability and mechanical properties of a new nickel-based superalloy", Materials Science and Engineering: A, 355 (2003) 96-105.

[26] H.-y. Li, X.-p. Song, Y.-l. Wang, G.-l. Chen, "Coarsening and age hardening behaviors of γ′ particles in GH742 during high temperature treatment", Journal of Iron and Steel Research, International, 16 (2009) 81-86.

[27] J.H. Westbrook, "Chromium and chromium alloys", in Kirk-Othmer Encyclopedia of Chemical Technology, 3rd ed. (M. Grayson, Ed.), John Wiley and Sons, New York, 6 (1979) 54-62.

[28] J.H. Hollomon, "Tensile deformation", AIME Transactions, 12 (1945) 1-22.

[29] D. Ludwigson, "Modified stress-strain relation for FCC metals and alloys", Metallurgical and Materials Transactions B, 2 (1971) 2825-2828.

[30] P. Ludwik, "Elemente der technologischen Mechanik", Springer-Verlag, 2013.

[31] E. Voce, "The relationship between stress and strain for homogeneous deformation", J Inst Met, 74 (1948) 537-562.

[32] H.W. Swift, "Plastic instability under plane stress", Journal of the Mechanics and Physics of Solids, 1 (1952) 1-18.

[33] M. Sundararaman, P. Mukhopadhyay, S. Banerjee, "Deformation behaviour of γ″ strengthened Inconel 718", Acta Metallurgica, 36 (1988) 847-864.

[34] Z. Fan, H. Mingzhi, S. Deke, "The relationship between the strain-hardening exponent n and the microstructure of metals", Materials Science and Engineering: A, 122 (1989) 211-213.

[35] H. Kim, S. Chun, X. Yao, Y. Fang, J. Choi, "Gamma prime (γ′) precipitating and ageing behaviours in two newly developed nickel-base superalloys", Journal of Materials Science, 32 (1997) 4917-4923.

[36] T. Wang, G. Sheng, Z.-K. Liu, L.-Q. Chen, "Coarsening kinetics of γ′ precipitates in the Ni–Al–Mo system", Acta Materialia, 56 (2008) 5544-5551.

LIST OF ABBREVIATIONS

AFC	Aged and Furnace Cooled
APBs	Anti-phase Boundaries
bcc	Body Centred Cubic
bct	Body Centred Tetragonal
BF	Bright Field
BSE	Back Scattered Electron
CRSS	Critical Resolved Shear Stress
DF	Dark Field
DS	Directional Solidification
EDS	Energy Dispersive Spectroscopy
e/a ratio	Free Electrons Per Atom
fcc	Face Centred Cubic
FESEM	Field Emission Scanning Electron Microscope
FFT	Fast Fourier Transformation
hcp	Hexagonal Closed Pack
HRTEM	High Resolution Transmission Electron Microscope
ICP-OES	Inductive Coupled Plasma Optical Emission Spectroscopy
JCPDS	Joint Committee on Powder Diffraction Standards
KS	Kurdjumov-Sachs
LCF	Low Cycle Fatigue
LSW Model	Lifshitz and Slyozov and Wagner Model
MLSW Model	Modified Lifshitz and Slyozov and Wagner Model
NW	Nishiyama-Wasserman
ODS	Oxide Dispersion Strengthened
OM	Optical Microscope
OR	Crystallographic Orientation Relationship
ppm	Parts Per Million
P/M	Powder Metallurgy
PSD	Position Sensitive Detector
RT	Room Temperature
SAED	Selected Area Electron Diffraction
SC	Single Crystal
SCDs	Strongly Coupled Dislocations

SE	Secondary Electron
SEM	Scanning Electron Microscope
SiC	Silicon Carbide
SS	Supersaturated Solid Solution
SSRT	Slow strain Rate Testing
ST	Solution Treatment
TCP	Topologically Close Packed
TEM	Transmission Electron Microscope
TIDC	Trans-interface Diffusion Controlled
TTT	Time Temperature Transformation
UTS	Ultimate Tensile Strength
WCDs	Weakly Coupled Dislocations
XRD	*X*-ray Diffraction
YS	Yield Strength (calculated as 0.2% proof strength)

LIST OF SYMBOLS

a_{γ}	Lattice parameter of disordered *Ni*-matrix (γ-phase)
$a_{\gamma'}$	Lattice parameter of ordered γ'-phase
at.%	Atomic Fraction
A	Numerical factor dependent upon the morphology of particles
b	Burgers vector of dislocations
$C_{\gamma,T}$	Concentration of γ'-forming solutes in the γ-matrix at temperature T
ΔC	Degree of supersaturation
d	Particle size
e_p	Enveloped phase
e	Engineering plastic strain
ε_t	True plastic strain
E	Elastic modulus
E_{int}	Elastic interaction energy between particles
E_{str}	Elastic strain energy between precipitate and matrix due to lattice mismatch
E_{surf}	Surface energy of particle
f	Volume fraction
G	Shear strength of obstacles
ΔG_V	Change in volume free energy associated with the nucleation event
J	Nucleation rate
K	Coarsening rate constant
κ	Strength factor
k	Boltzmann constant
β	Temporal exponent
n_0	Total number of potential nucleation sites
n	Strain hardening exponent
N_v	Particles number density
r_0	Average radius of particles at time t_0 (beginning of the coarsening stage)
r	Average radius of particles at a time t
s	Engineering stress
T_l	Line tension of dislocations
T	Temperature
T_e	Equilibrium solvus temperature
ΔT_c	Critical under cooling

τ_{ss}	Critically resolved shear stress
$\Delta\tau_{ss}$	Change in Critically resolved shear stress value
υ	Poisson's ratio
wt.%	Weight Fraction
χ^2	Sum of residual squares calculated for a given equation to fit a curve
γ_s	Composition of the saturated γ-phase
γ_{ss1}	Composition of super saturated solid solution state of the disordered alloy
γ_{ss2}	Composition of super saturated solid solution state of the alloy after partial precipitation of the γ'-phase during water quenching
Z	Zeldovich factor
β^*	Represents rate at which a single atom joins a critical nucleus to make it supercritical
α_T	Thermal expansion coefficient
σ_t	True stress
ϵ	Lattice misfit
λ	Inter particle spacing
λ_{WL}	Wavelength of radiation (*X*-ray/ neutron) source
τ	Incubation time
Γ	*APB* energy on {111} plane of the γ'-precipitates

LIST OF FIGURES

LIST OF TABLES

CHAPTER 1

INTRODUCTION

1.1. Background:

Alloy 693 is a newly developed precipitation hardened *Ni*-base superalloy. It is derived from solid solution strengthened Alloy 690 by the addition of *Al, Ti* and *Nb* elements (see Table 1.1) [1, 2]. Presence of *Al* and *Ti* induces the formation of coherent ordered $L1_2$ type γ'-phase precipitates of $Ni_3(Al,Ti)$ stoichiometry in the γ-matrix (*fcc* structure). Addition of *Al, Ti* and *Nb* also improves corrosion, sulfidation and oxidation resistance, surface stability and mechanical strength of the alloy [3]. The alloy finds applications in places, such as, nuclear waste management plants [4] and petrochemical processing industry [2]. It is also a candidate material for high temperature waste and biomass incinerators, and for high temperature fuel cells involved in synthetic gas production (*e.g.,* fuel cells to power automobiles) with potential to induce metal dusting [2].

Table 1.1. Nominal compositions (*wt.*%) of Alloy 690 and Alloy 693 [1, 2].

Ni	***Cr***	***Fe***	***Al***	***Nb***	***Mn***	***Ti***	***C***	***S***
Alloy 690								
Bal.	27-31	7-11	-	-	0.5 max	-	0.05 max	0.015 max
Alloy 693								
Bal.	27-31	2.5-6.0	2.5-4.0	0.5-2.5	1.0 *max.*	1.0 *max.*	0.15 *max.*	0.01 *max.*

1.2. Motivation:

Presence of *Al* and *Ti* plays a pivotal role in the formation of ordered $L1_2$ type γ'-phase particles with $Ni_3(Al,Ti)$ stoichiometry in Alloy 693. These hardening γ'-precipitates are coherent with γ-phase (*fcc* structure) matrix and impart strength to the alloy. In general, mechanical properties of such precipitation hardened alloys are governed by its microstructure such as size, size distribution, lattice misfit, morphology and volume fraction of the hardening phase. Morphology of γ'-precipitates evolves continuously, from simple spherical to cuboidal and octocuboidal, and to complex structures, such as dendritic or octodendritic. Such morphological evolution occurs as anisotropic elastic strain energy starts dominating over the isotropic interfacial energy. Size of precipitates is another important parameter and plays an important role in the strength of the alloy. When the size of γ'-precipitates is small, dislocations overcome precipitates by shearing them which requires additional energy to create extra surface during shearing. On the other hand, when the size of precipitates is large, additional stress is required to make dislocations expand and bend between particles. These size and morphological changes, therefore, play important roles in deciding structural stability and properties of the alloy during service. It has been reported in literature by Singh et *al.* [37] that initial heat treatment and subsequent processing and servicing conditions can affect properties of alloys by varying size and size distribution of the ordered phase. For instance, microstructures containing multi-modal distribution of precipitating particles have been reported in many *Ni*-base alloys which were induced to form by two step annealing and/or cooling at different rates [38-41]. Often these distributions are desired to strengthen alloys by simultaneous action of different strengthening mechanisms.

Furthermore, multi-component alloys like Alloy 693 are often designed on the basis of model systems and other (minor) elements are added to impart desired properties. However, addition of minor elements makes their overall composition rather complex, which may disturb equilibrium states of the model system and destabilize otherwise equilibrium phase. For instance, *Cr* solubility in *Ni*-solid solution is found to decrease with addition of *Al* and *Ti* [5-8]. As mentioned earlier, since Alloy 693 is a modified version of Alloy 690, addition of *Al* and *Ti* in the latter may alter solubility of *Cr* in the former. Phase transformations and relevant equilibrium states are, however, difficult to predict due to lack of reliable experimental data on equilibrium states specially for their prolonged usage at elevated temperatures.

There appears to be no report on the influence of ageing at elevated temperatures on microstructural stability, precipitation behaviour of the γ'-phase and its effect on mechanical behaviour of Alloy 693. Limited literature available on this alloy pertains the effect of solution annealing conditions on microstructure and mechanical properties of the alloy [13, 42] and its resistance to metal dusting attack [43]. The present study is an attempt to understand these aspects of Alloy 693.

1.3. Objectives:

Aims of this dissertation is to study:

i) Precipitation behaviour of γ'-precipitates in Alloy 693.

ii) Effect of *Al / Ti* addition on the stability of *Ni-Cr* solid solution in Alloy 693.

iii) Mechanical behaviour of aged Alloy 693.

1.4. Layout of thesis:

This thesis contains seven chapters including the present chapter, **Chapter 1.**

Chapter 2 gives a brief account of the **Literature Survey** pertaining to physical metallurgy and strengthening mechanisms of *Ni*-base superalloys.

Chapter 3 gives a detailed account of **Experimental** procedures, heat treatment schedules, experimental and analytical techniques used to fulfil objectives of the present study.

Chapters 4-6 present **Results** obtained in this study and analysed in the light of available literature.

Chapter 7 gives a list of **Conclusions** arrived on the basis of this study. This chapter also provides a **Scope for Future Research Work** that can be carried on the present work.

CHAPTER 2

LITERATURE SURVEY

2.1. Introduction:

Superalloys offer excellent combination of strength and corrosion resistance at high temperatures [44]. They are used for a number of applications including aircraft engines, power plant, chemical and petrochemical industries. They are also used in cryogenic applications, metal processing and medical components [15].

There are three classes of superalloys, *NiFe*-base, *Ni*-base and *Co*-base, which are further categorized in two grades on the basis of strengthening mechanisms: (i) solid solution strengthened and (ii) precipitation hardened superalloys. A few examples of superalloys are given in Table 2.1.

Table 2.1. Superalloys belonging to three different classes [45].

Class of Superalloy	Example
NiFe-base	Incoloy 800H, Incoloy 901, Inconel 718
Ni-base	Waspaloy, Astroloy, Inconel 690
Co-base	Haynes 188, *L-605*, Elgiloy

Selection of a specific alloy is ascertained by expected service temperature, life and environment. Among different classes of alloys, *Ni*-base alloys possess best combination of strength and oxidation resistance at high temperatures [46]. *Ni*-base alloys also possess good load bearing capacity under static, dynamic and creep conditions, as well as tolerance to severe operating environments, and can be operated at highest homologous temperature [15]. Their high temperature corrosion resistance can be improved further by coating [47, 48].

Depending upon application and composition involved they can be wrought or cast, selection of which is based upon expected cost effectiveness [44, 45].

2.2. *Ni*-base superalloys:

Ni-base superalloys are complex alloys containing about 10-12 constituent elements [46], which are added in a controlled manner to impart the strength and improve the properties of alloys. *Cr, Fe, Co, Mo, W, Nb, Al, Ti* and *Ta* are major alloying elements while *B*, *C, Zr, Hf, Mg, La* and *Y* are added in very small amounts (a few *ppm* level). Table 2.2 briefly describes the role of different alloying elements in *Ni*-base superalloys [49].

Table 2.2. Role of different alloying elements in *Ni*-base superalloys [49, 50].

<table>
<tr><th>Elements</th><th colspan="2">Responsible For</th></tr>
<tr><td>Co, Cr, Fe, Mo, W, Ta, Re</td><td colspan="2">Solid solution strengthening</td></tr>
<tr><td>Ta, Ti, Nb, Hf, Zr</td><td rowspan="4">Carbide formers
(Reduction of grain boundary sliding)</td><td>MC</td></tr>
<tr><td>Cr</td><td>M_7C_3</td></tr>
<tr><td>Cr, Mo, W, Co, Fe</td><td>$M_{23}C_6$</td></tr>
<tr><td>Mo, W, Nb, Co, Ta, Fe, Cr</td><td>M_6C</td></tr>
<tr><td>Nb, Ta, W, Re, Ru</td><td colspan="2">Increase solvus temperature of γ'-precipitates</td></tr>
<tr><td>Al, Ti, Nb</td><td colspan="2">Forms the hardening precipitates (γ'-, γ''-, η- and δ-)</td></tr>
<tr><td>Al, Cr, Y, La, Ce</td><td colspan="2">Imparts oxidation resistance</td></tr>
<tr><td>Cr, Co, Si</td><td colspan="2">Imparts sulfidation resistance</td></tr>
<tr><td>La, Th</td><td colspan="2">Improves hot corrosion resistance</td></tr>
<tr><td>B, Ta</td><td colspan="2">Improves creep properties</td></tr>
<tr><td>B</td><td colspan="2">Increases rupture strength</td></tr>
<tr><td>B, C, Zr, Hf</td><td colspan="2">Refines grain-boundaries</td></tr>
</table>

Ni-base superalloys comprise austenitic matrix (γ-phase) and may contain several secondary phases [51]. Depending upon the main strengthening mechanism, they are classified in the following ways [44, 51]:

i) Solid solution strengthened alloys, *e.g.*, Hastelloy *X*, *IN-625*, *IN-690*, *etc.* which also gains some strength from carbides.

ii) Precipitation hardened alloys, which are further categorized in following way:

a) γ'-precipitation hardened alloys, *e.g.*, Udimet 700, Waspaloy, Astroloy, Rene 80, *IN-713*, *etc.*

b) γ''-precipitation hardened alloys, *e.g.*, *IN-718*, *IN-625*, *etc*.

c) Both γ'- and γ''-precipitation hardened alloys, *e.g.*, *IN-706*, *IN-909*, *etc*.

iii) Oxide dispersion strengthened (*ODS*) alloys, *e.g., MA-754* and *MA-6000*, *etc.* which are mainly strengthened by oxide dispersed fine particles, like inert yttria.

These secondary phases are briefly discussed in Table 2.3 and described in brief in Section 2.3. Precipitation of secondary phases is a function of alloy chemistry, ageing temperature and time. Microstructure (which includes morphology, size and volume fraction) and chemistry of these phases control the properties of the alloy, and their precipitation in controlled manner impart excellent properties to the alloy.

Table 2.3. Phases observed in *Ni*-base superalloys [51].

Phase	Bravais Lattice	Stoichiometry	Remarks
γ	*fcc* (disordered)	*Ni*-base austenitic matrix	Contains most of the solid solution elements.
γ'	*fcc* (ordered $L1_2$)	$Ni_3(Al,Ti)$	Strengthening phase which is coherent with matrix. Size of the precipitates is sensitive to exposure time and temperature. Precipitates change their shape with variation in γ/γ' lattice mismatch.

γ''	*bct* (ordered $D0_{22}$)	Ni_3Nb	Disk shaped strengthening phase and coherent with matrix.
η	*hcp* ($D0_{24}$)	Ni_3Ti	Forms in alloys with high *Ti/Al* ratios after extended period of exposure. It forms in cellular morphology at intergranular sites while in acicular platelet morphology at intragranular sites.
δ	Orthorhombic (ordered Cu_3Ti-$D0_a$)	Ni_3Nb	It precipitates out in acicular shape in overaged alloys (aged at 815-980°*C*).
MC	Cubic	*MC* *M (Ti, Nb, Hf, Ta, Zr)*	These carbides appear as globular, irregularly shaped particles. '*M*' represents *Ti, Ta, Nb, Hf, Th*, or *Zr*.
$M_{23}C_6$	*fcc*	$M_{23}C_6$, *M (Cr, Ni, Co, Fe, W, Mo)*	These carbides usually forms at grain boundaries. It precipitates out as films, globules, platelets, lamellae and cells. '*M*' usually represents *Cr*, but *Ni, Co, Fe, Mo* and *W* can substitute it.
M_6C	*fcc*	M_6C *M (Mo, W, Nb, Co, Ta, Fe, Cr, Ni)*	Generally '*M*' represents *Mo* and *W*, there is some solubility for *Cr, Ni, Nb, Ta, Co*. These carbides are randomly distributed in matrix.
M_7C_3	Hexagonal	Cr_7C_3	Blocky intergranular precipitates; forms after high temperature (1000°*C*). exposure.
M_3B_2/ M_5B_3	Tetragonal	M_3B_2/M_5B_3 *M (Mo, Ta, Nb, Ni, Fe, V, Ti, Cr)*	These borides are observed in *FeNi*- and *Ni*-base alloys with about 0.03% *B* or greater. '*M* ' elements can be *Mo, Ta, Nb, Ni, Fe,* or *V*. Morphology of these are similar to carbides.
MN	Cubic	*MN* *M (Ti, Nb, Zr)*	These nitrides are observed in alloys containing *Ti, Nb* or *Zr*; and have square to rectangular shapes.
μ	Rhombohedral	Co_2W_6, $(Fe,Co)_7(Mo,W)_6$	These precipitates form at high temperatures in alloys with high *Mo* or *W* contents. They precipitate out as coarse, irregular Widmanstatten platelets.

Laves phase	Hexagonal	Fe_2Nb, Fe_2Ti, Fe_2Mo, Co_2Ta, Co_2Ti	They form at higher temperatures mostly in *Fe*- and *Co*-base alloys. Precipitates out as irregularly shaped globules, elongated or as platelets.
σ	Tetragonal	*FeCr, FeCrMo, CrFeMoNi, CrCo, CrNiMo*	These are more often observed in *FeNi*- and *Co*-base alloys after extended exposure between 540-980°*C* , and rarely seen in *Ni*-base alloys. Precipitates out in irregularly shaped globules, usually elongated.

Microstructures of the heat treated *Ni*-base superalloys are metastable, which approach to equilibrium during extended exposure and creep at elevated temperatures. Salient changes that may occur in *Ni*-base alloys are [52]:

i) Coarsening of hardening precipitates, which increases significantly as exposure temperature approaches towards the solvus temperature.

ii) Change in carbide chemistry (decomposition of a carbide in another carbides).

iii) Precipitation of *tcp*-phases, such as σ, μ and Laves phases, particularly in alloys containing high amounts of refractive elements.

2.3. Morphology and characteristics of different phases:

2.3.1. γ-phase:

γ-phase is a *Ni*-base nonmagnetic disordered *fcc*-matrix phase and contains high percentage of solid solution elements such as *Co, Fe, Cr, Mo, W, Ta* and *Re,* which provides solid solution strengthening to the matrix [53]. γ-phase has wide solubility range for alloying elements, that allows the dissolution of high melting point refractory elements as well as allows the precipitation of intermetallic phases, *e.g.*, γ'- and γ''-phases which imparts strength [46]. Mechanical properties of most of alloys can be changed by changing grain size of the matrix phase. Fine grain microstructure is reported to give excellent hardness, tensile properties and longer *LCF* life [25, 48, 54-56]. For better creep rupture properties coarser grain size of γ-matrix is desired [57].

2.3.2. γ'-phase:

γ'-phase is an ordered cubic phase with Ni_3Al stoichiometry. Crystal structure of its unit cell is shown in Figure 2.1(a). γ'-precipitates remain coherent with disordered matrix phase and obey a cube to cube orientation relationship. This phase remains ordered upto their melting point (~1375°*C*) in binary *NiAl*-alloys, but the ordering temperature varies with addition of alloying elements [15, 58]. Its solvus temperature decreases with elements like *Cr, Co, Ti, Mo* and increases with *Ta, W, Re, Ru* elements [50, 59]. Alloying elements, like *Ti, Nb, Cr* and *Fe* present in alloy may substitute *Ni* and/or *Al* atoms in the γ'-precipitates [60]. Such elemental substitution significantly alters phase stability of γ'-precipitates and therefore affect properties of alloy [61]. Further, elements like *Ti, Nb, Ta, Cr* and *Fe* promotes the formation of γ'-precipitates and increases volume fraction of these precipitates [5, 62-64].

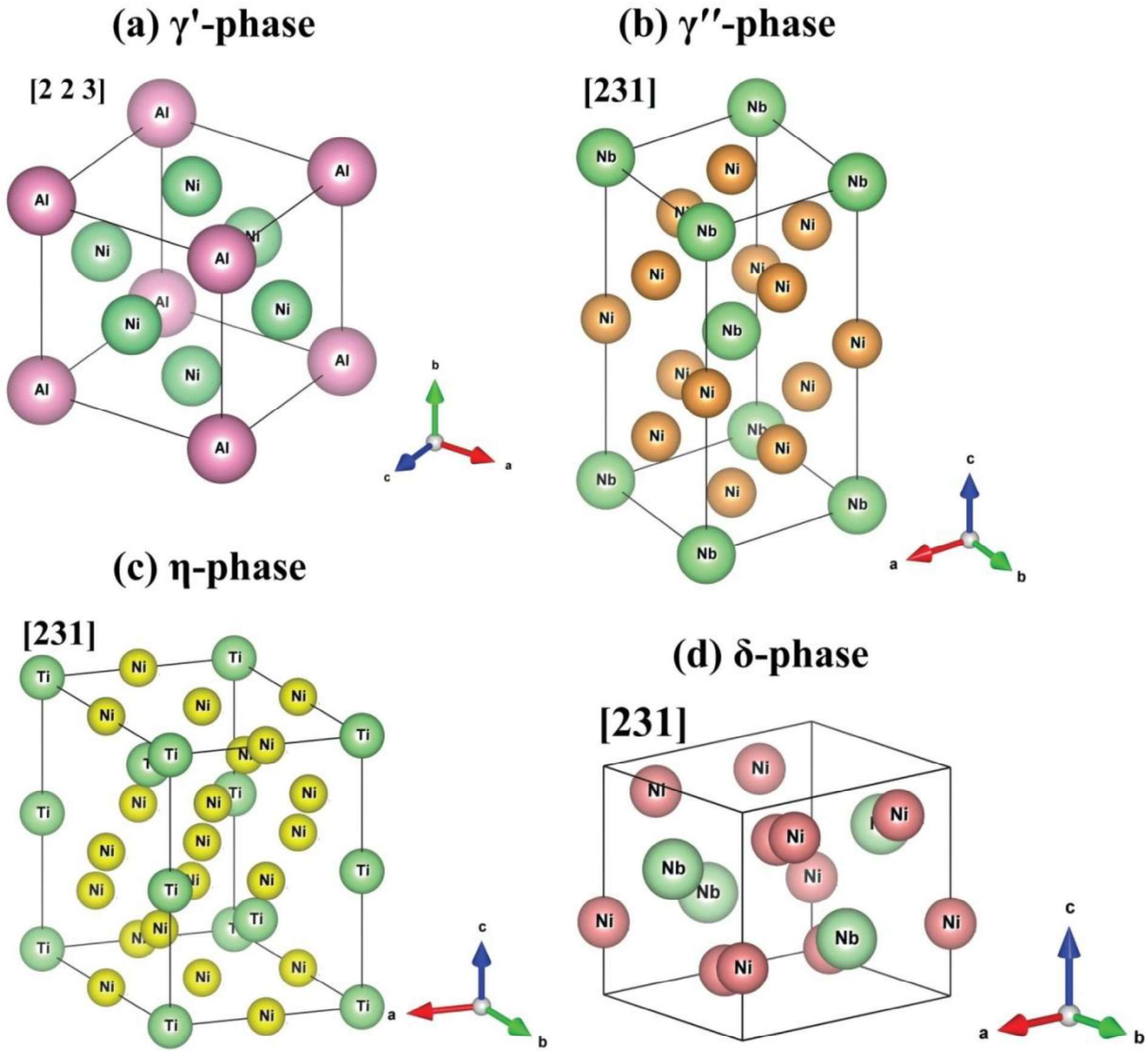

Figure 2.1. Line sketch of ordered crystal structures of (a) γ'-phase; (b) γ''-phase; (c) η-phase; and (d) δ-phase, where *Ni* and *Al/Nb/Ti* atoms are on specified atomic positions and would be replaced by other alloying elements.

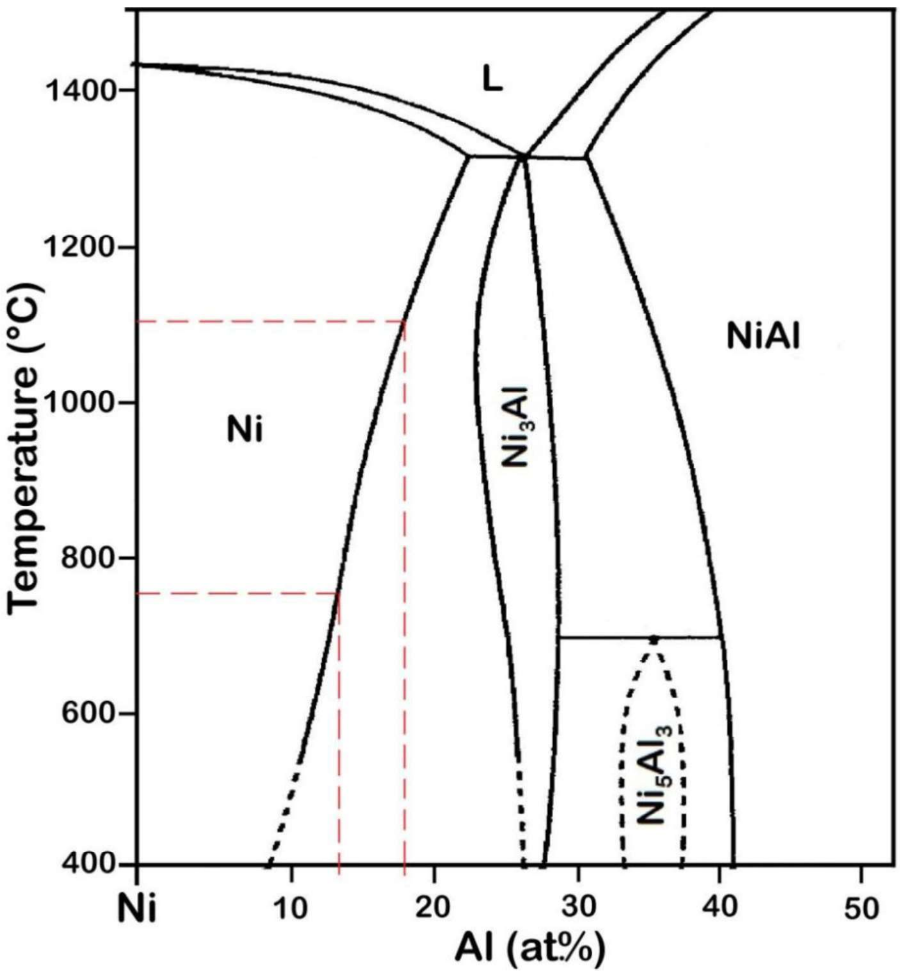

Figure 2.2. Part of *NiAl*-binary phase diagram, showing the γ-γ' phase field as well as solubility limit of *Al* in *Ni* is marked at $750°C$ and $1100°C$ temperatures [65].

Figure 2.2 shows a part of *NiAl*-binary alloy phase diagram [65], which depicts that solubility limit of *Al* decreases with decreasing temperature. Lowering the temperature from $1100°C$ to $750°C$, solubility of *Al* decreases from ~18*at.%* to ~13*at.%* (marked by dashed lines in Figure 2.2). Presence of other alloying elements affects the equilibrium state of the alloy system, by altering the phase stability of the γ'-phase (see Figure 2.3). It is evident from Figure 2.3 that addition of *Ti, Nb, Cr* and *Fe* decreases the solubility of *Al* in *Ni*, which promotes the formation of γ'-phase particles [5, 62, 63]. *Ti* and *Nb* preferentially go to *Al* lattice sites while *Cr* and *Fe* substitute *Ni* atoms. Addition of these elements (see Figure 2.3) is limited to some extent because beyond a certain amount substitution of *Al* by *Ti* and *Nb* elements leads the formation of detrimental phases, *e.g.*, η and δ phases along with γ'-phase. From Figure 2.3(a), it is evident that addition of *Ti* beyond 16*at.%* promotes the η-phase (hexagonal Ni_3Ti-phase) formation. Similarly from Figure 2.3(b), it is clear that more than 8*at.% Nb* would form δ-phase (orthorhombic Ni_3Nb-phase). Mishima et *al.* [61] have shown that *Nb* can be dissolved upto about 8.0*at.%* in *Ti* free γ'-phase, fraction of which would decrease in presence of *Ti*.

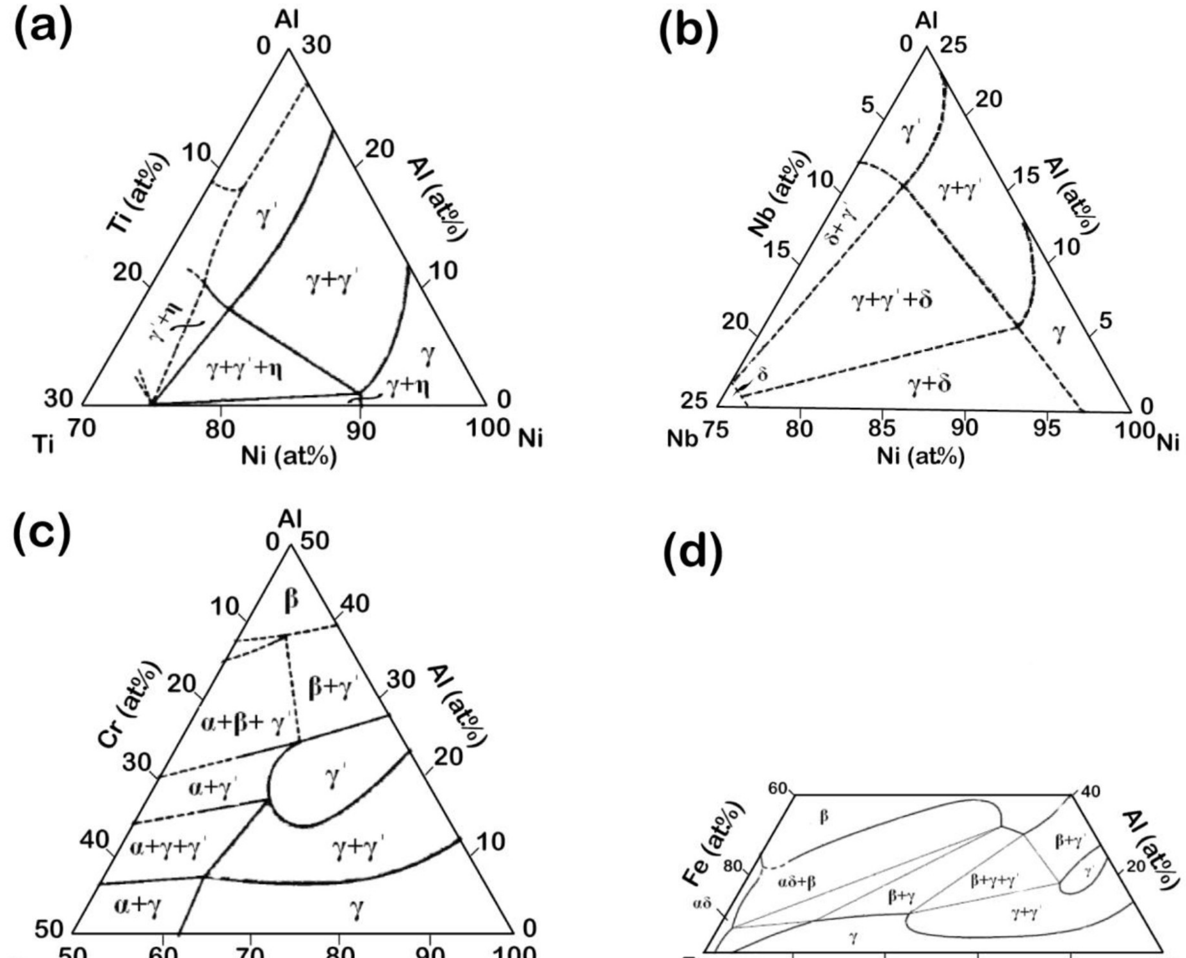

Figure 2.3. Isothermal ternary sections of: (a) *Ni-Al-Ti* at 750°*C* [62]; (b) *Ni-Al-Nb* at 800°*C* [62]; (c) *Ni-Al-Cr* at 750°*C* [5]; (d) *Ni-Al-Fe* at 750°*C* [63] .

Transformation of γ'-phase of Ni_3Al to other phases with N_3X stoichiometry could be explained on the basis of free electrons per atom (*e/a* ratio) of the alloy that governs the stability of competing structures of N_3X stoichiometry in accordance with the hypothesis propounded by Sinha [66]. According to Sinha [66], the *e/a* ratio for the stability of the $L1_2$, $D0_{24}$ and $D0_a$ structures of Ni_3Al, Ni_3Ti and Ni_3Nb compounds are 8.25, 8.5 and 8.75, respectively. Addition of *Ti* and/or *Nb* in Ni_3Al, having free electrons more than those in *Al*, increases the *e/a* ratio and stabilizes the other competing phases [66].

Depending upon heat treatment conditions chemistry of γ'-precipitates varies. Chen et *al.* [67] have investigated the compositional variation for γ'-precipitates in *Ni*-base *RR-1000* superalloy, which was governed by cooling rate employed during heat treatments. In their studies they observed that γ'-precipitates in fast cooled samples showed small size distributions and negligible compositional variations, while remarkable size dependent compositional variations was observed for slow cooled samples [67].

Morphology of γ'-precipitates is governed by three main factors [68]:

i) Surface energy (E_{surf}) of particle.

ii) Strain energy (E_{str}) between precipitate and matrix due to lattice mismatch.

iii) Interaction energy (E_{int}) between particles due to overlap of elastic strain field around individual particles.

Out of three, later two are elastic in nature [68]. Shape of the γ'-precipitates is established by minimizing sum of E_{surf} and E_{str}, and it changes with variation in lattice mismatch. Doi et *al.* [69] have shown that E_{int} has a strong effect on the distribution of γ'-precipitates in such a way that adjacent particles aligned along <100> direction to minimize E_{int} [69].

Elastic strain energy is governed by coherency of γ/γ' interface, which in turn depends upon lattice misfit (ϵ) and is defined in equation (i) [15],

$$\epsilon = 2\,(a_{\gamma'} - a_{\gamma})\,/\,(a_{\gamma'} + a_{\gamma}) \qquad \text{...(i)}$$

where a_γ and $a_{\gamma'}$ are lattice parameter of disordered *Ni*-matrix (γ-phase) and γ'-phase, respectively. Lattice parameter of γ'-phase ($a_{\gamma'}$) increases with addition of *Cr, Ti, Ta, Nb, Mo, Fe, W etc.* elements in γ'-phase [50]. Lattice parameter of γ-matrix (a_γ) increases with addition of *Cr, Ti, Ta, Nb, Mo, Fe, Al, Mn* ; while decreases with precipitation of γ'-particles [70]. Lattice misfit (ϵ) consequently is a function of solutes partitioning between γ- and γ'-phases. It also depend upon thermal history of the alloy, as thermal expansion coefficients (α_T) of γ- and γ'-phases are different: α_T for *Ni* is $13.1K^{-1}$ while that of the γ'-phase (Ni_3Al in binary *NiAl*-alloy) is $12.3K^{-1}$ [71]. Thus value of ϵ would change depending upon the temperature at which measurements were carried out [72]. Lattice misfit (ϵ) can be positive if $a_{\gamma'} > a_\gamma$, *as* in Nimonic 80*A* and Nimonic 90 alloys or negative as in Nimonic 105 and Nimonic 115 alloys depending upon alloying additions [21].

Due to the variations in lattice misfit strain morphological changes of γ'-precipitates take place. Initially γ'-particles precipitate out with spherical morphology which changes to cuboidal after a critical size. Size of precipitates at which morphological transition takes place is the function of magnitude of the lattice mismatch [21], constants of elasticity and volume fraction of the precipitates [73]. Figure 2.4 depicts schematic of morphological transitions sequence observed in a *Ni*-base alloy [21]. This sequence was independent of misfit sign, but the size at which morphological transition took place was observed to be the function of lattice misfit (ϵ) [21].

Microstructural stability is most important factor and desired for the performance of the alloy. In γ'-precipitate hardened *Ni*-base superalloys, these precipitates are prone to coarsening during ageing or servicing, which in turn degrades strength of alloy. γ-γ' microstructure stability at elevated temperatures depends upon the resistance to coarsening of γ'-precipitates. Coarsening kinetics of these precipitates is governed by coherency strain and increasing coherency strain accelerates coarsening rate [74]. Thus precipitates coarsening is enhanced with increasing lattice misfit (ϵ), which in turn deteriorates the microstructural stability and strength of alloy at elevated temperatures [61, 75].

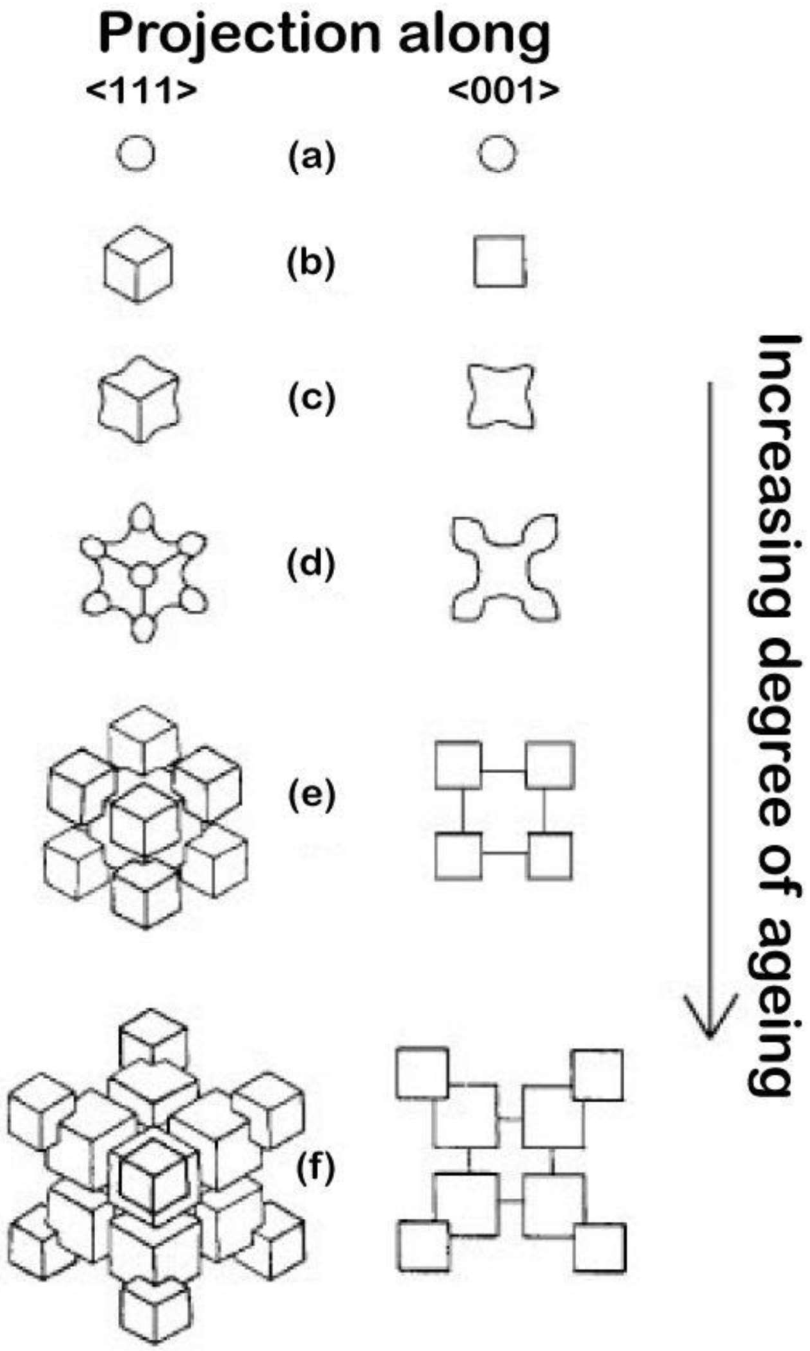

Figure 2.4. Schematic diagram showing strain induced development of γ'-precipitates morphologies during ageing; projection along <111> and <001> are shown in left and right, respectively [21].

Addition of high partitioning and slow diffusing elements (*e.g., Nb* and *Ta*) to γ'-precipitates decreases coarsening kinetics of γ'-phase [50]. Coarsening of γ'-precipitates generally follows Lifshitz and Slyozov [19] and Wagner [20] kinetics, known as the *LSW* model. The *LSW* model is based on dilute solid solution assumption and the coarsening of precipitates is governed by solute diffusion through the matrix. Later on it was modified by Ardell [76] to take into account volume fraction of γ'-precipitates. The modified *LSW* (*MLSW*) theory predicts that along with classical *LSW* theory the coarsening rate increases with increasing volume fraction, even at very small volume fraction of precipitates [76]. After this modification, Chellman and Ardell [77] did a systematic investigation of coarsening behaviour of γ'-precipitates in binary *NiAl*-alloys using the modified *LSW* theory. These alloys contained 0.09-0.60 volume fraction (*f*) of γ'-precipitates and they aimed to study the effect of volume fraction (*f*) on the coarsening behaviour of precipitates. Results of their study showed that coarsening behaviour was not affected by *f*-value and was in good agreement with original *LSW* theory. They concluded that the original *LSW* theory is capable of quantitatively describing coarsening behaviour in systems containing as much as 0.60 volume fraction of γ'-precipitates. More recently, Ardell and Ozolins proposed trans-interface diffusion controlled (*TIDC*) coarsening model [78]. According to *TIDC* coarsening model, in systems involving order/disorder interfaces, the diffusion of solutes across a partially ordered interface would be rate limiting factor for coarsening. In general, precipitate size is correlated with ageing time to establish the coarsening mechanisms, and temporal exponent roughly determines coarsening mechanism: it is expected to be 3 for *LSW* coarsening and 2 for *TIDC* coarsening [23].

Microstructure (morphology, size and volume fraction) of γ'-precipitates governs the mechanical properties of alloy, which can be modified by tailoring chemical composition and processing condition of alloy [79]. For instance addition of *Ti* increases the lattice misfit (ϵ), as size of *Ti* is larger in comparison of *Al* thus lattice parameter of γ'-phase increases after partial substitution of *Al* by *Ti* [80]. Addition of *Ti* also increases the anti-phase boundary (*APB*) energy, which contributes in hardening [51]. Miller and Ansell [81], and Grose and Ansell [82] studied the influence of coherency strain on mechanical properties of series of *Ni*-base alloys and concluded that coherency strains dominantly contribute to the strengthening of alloy.

2.3.3. γ''-phase:

γ''-phase is a *bct* ordered phase with Ni_3Nb stoichiometry, atomic arrangements in unit cell of γ''-phase is shown in Figure 2.1(b). It is found in *Ni*- and *NiFe*-base alloys with high *Nb* contents, such as *IN-625*, *IN-706*, *IN-718*, Rene 62 and Udimet 630 [83]. Presence of *Fe*-promotes the formation of γ''-phase, while *Al*-suppress its formation [84]. It generally precipitates out as coherent disc shaped precipitate with large lattice mismatch strain (of the order of 2.9%), Figure 2.5(b) [85]. It exhibits $\{100\}_{\gamma''}//\{100\}_{\gamma}$ and $[001]_{\gamma''}//<001>_{\gamma}$ orientation relationship with *fcc* γ-matrix. Solvus temperature of this phase is low (*e.g.*, 650°*C* for *IN-718*), thus provides very high strength at low to intermediate temperatures. At temperatures above about 650°*C,* it transforms into δ-phase, which causes loss of alloy strength.

2.3.4. η-phase:

η-phase is an ordered ($D0_{24}$) hexagonal phase of Ni_3Ti stoichiometry, line sketch of its crystal structure is given in Figure 2.1(c). It forms in *NiFe*-base superalloys hardened by γ'-precipitates with high *Ti/Al* ratios such as Nimonic 901and *A-286* alloys. In these alloys after extended period of exposure at higher temperatures *Ti*-rich γ'-phase transforms to η-phase. It forms in cellular morphology at inter-granular sites while in acicular platelet morphology at intra-granular sites, Figure 2.5(c) shows the η-phase in plate shape morphology in a heat treated *Ni*-base superalloy [86]. Small amount of η-phase is useful to control the microstructure but excessive presence degrades mechanical properties of the alloy. Increasing

Ti contents enhance formation of η-phase while increased *Al* contents retard its formation [87].

2.3.5. δ-phase:

δ-phase is an ordered orthorhombic phase with Ni_3Nb stoichiometry, line sketch of its crystal structure is given in Figure 2.1(d). It forms in *Nb*-rich superalloys in temperature range 650-980°*C* when the γ''-phase transform to δ. Precipitates of δ-phase normally have plate shape morphology with $\{111\}_\gamma$ habit plane and also observed in globular shape at grain boundaries [83]. Figure 2.5(d) shows the plate shape δ-phase precipitates in heat treated *IN-625*, in the vicinity of grain boundaries [85]. δ-phase is beneficial if present in small amount, as it controls and refine the grain size of matrix which in turn results in improved tensile properties, fatigue resistance, and creep rupture properties. Large amount of it degrades properties of the alloy [88]. It is observed that presence of high contents of *Nb* and *Si* promotes the formation of δ-phase, while substitution of *Nb* by *Ta* suppresses its formation [87, 89, 90].

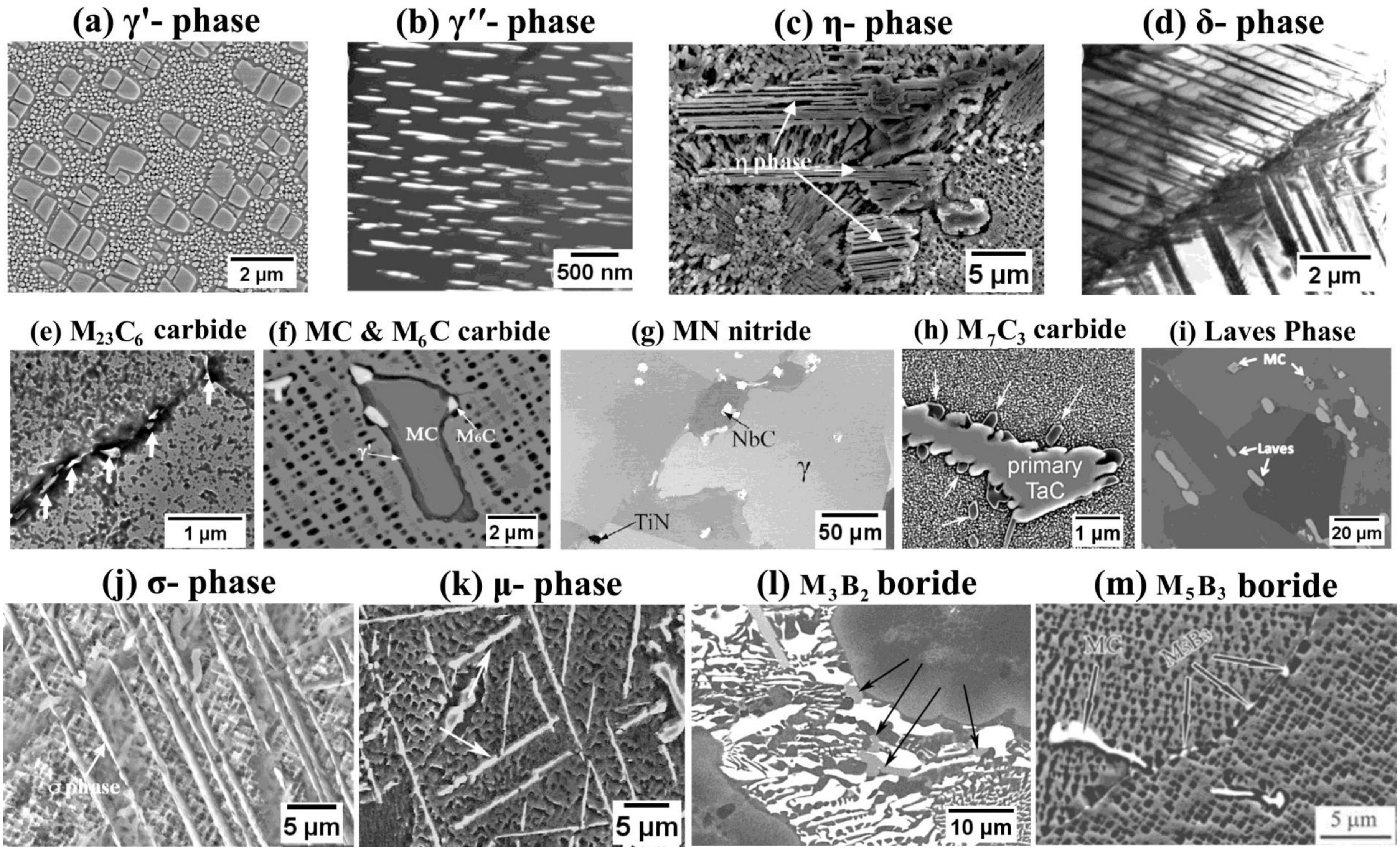
(a) γ'- phase
2 µm
(b) γ''- phase
500 nm
(c) η- phase
η phase
5 µm
(d) δ- phase
2 µm
(e) $M_{23}C_6$ carbide
1 µm
(f) MC & M_6C carbide
MC
M_6C
γ'
2 µm
(g) MN nitride
NbC
γ
TiN
50 µm
(h) M_7C_3 carbide
primary TaC
1 µm
(i) Laves Phase
MC
Laves
20 µm
(j) σ- phase
σ phase
5 µm
(k) µ- phase
5 µm
(l) M_3B_2 boride
10 µm
(m) M_5B_3 boride
MC
M_5B_3
5 µm

Figure 2.5. (a) *SE* micrograph of heat treated *IN-718LC*, showing γ'-precipitates in spherical and cuboidal morphology [91]; (b) *DF TEM*-micrograph of *IN-625* in heat treated condition, showing γ''-precipitates in disc shaped morphology [85]; (c) *SE*-micrograph of a *GTD111* based *Ni*-base superalloy in heat treated condition, showing η-precipitates in plate like morphology [86]; (d) *BF TEM*-micrograph of *IN-625* in heat treated condition, showing needle shape δ-precipitates in the vicinity of grain boundaries [85]; (e) *SE*-micrograph of a *Ni*-base superalloy, *Cr*-rich fine irregular shaped $M_{23}C_6$ carbides along grain boundaries [92]; (f) *SE*-micrograph of heat treated *Ni*-base superalloy, showing *Nb*-rich *MC*-carbide and M_6C-carbides rich in *Mo* and *W* [93]; (g) *BSE*-micrograph of heat treated *IN-718*, showing *TiN* nitride and *NbC* carbide [94]; (h) *SE*-micrograph of a *NiCrTaAlC*-alloy, showing irregular shaped Cr_7C_3 carbides (marked by arrows) [95]; (i) *BSE*-micrograph of a γ'-strengthened alumina forming austenitic alloy, showing Fe_2Nb-type elongated granular shape Laves phase particles [96]; (j) *SE*-micrograph of a *GTD111* based *Ni*-base superalloy in heat treated condition, showing needle shape σ-phase precipitates [86]; (k) *BSE*-micrograph of a heat tread *Ni*-base *K-465* superalloy, showing *Mo*, *W* and *Cr*-rich needle shaped μ-phase precipitates [97]; (l) *BSE*-micrograph of *MAR-M004 Ni*-base superalloy, *Cr* and *Mo*-rich irregular shaped M_3B_2-borides [98]; (m) *SE*-micrograph of heat treated *IN-792*, *Mo*-rich fine grain boundary M_5B_3-borides [99].

2.3.6. Carbides:

Depending upon alloy composition and processing conditions, different kinds of carbides could be formed in *Ni*-base superalloys at intergranular and transgranular positions. These can be MC, M_6C, $M_{23}C_6$, and M_7C_3, where M stands for one or more types of metal atom, whose atomic arrangements are given in Figure 2.6. Some solubility of other alloying elements present in the matrix is also there in all carbides. Trans-granular fine carbides impede material deformation while inter-granular carbides controls grain size, resist grain boundary sliding and permit stress relaxation. Formation of carbides tie up tramp elements which could cause phase instability during service. Thus carbides impart strength and phase stability to material but excess precipitation of carbides depletes the solute elements in the matrix and degrades properties of material.

2.3.6.1. *MC*-carbides:

MC-carbides are high temperature carbides and form during solidification of alloy melt so called primary carbides. In general high *Nb* and *Ta* content favour *MC*-carbides. They have cubic structure and line sketch of it is shown in Figure 2.6(a). They have little or no orientation relation with matrix and occur in different morphologies - coarse, globular or blocky. They are distributed heterogeneously, both in inter-granular and trans-granular positions throughout the matrix. Figures 2.5(f) and 2.5(g) show the blocky and globular shape *Nb*-rich *MC*-carbides in heat treated *Ni*-base superalloy and *IN-718*, respectively [93, 94]. They act as a major source of carbon and decompose into $M_{23}C_6$ and/or M_6C carbides during processing and servicing [51]. Substitution of *Mo* and *W* decreases the stability of *MC*-carbides and promotes the degeneration reaction of these carbides [53].

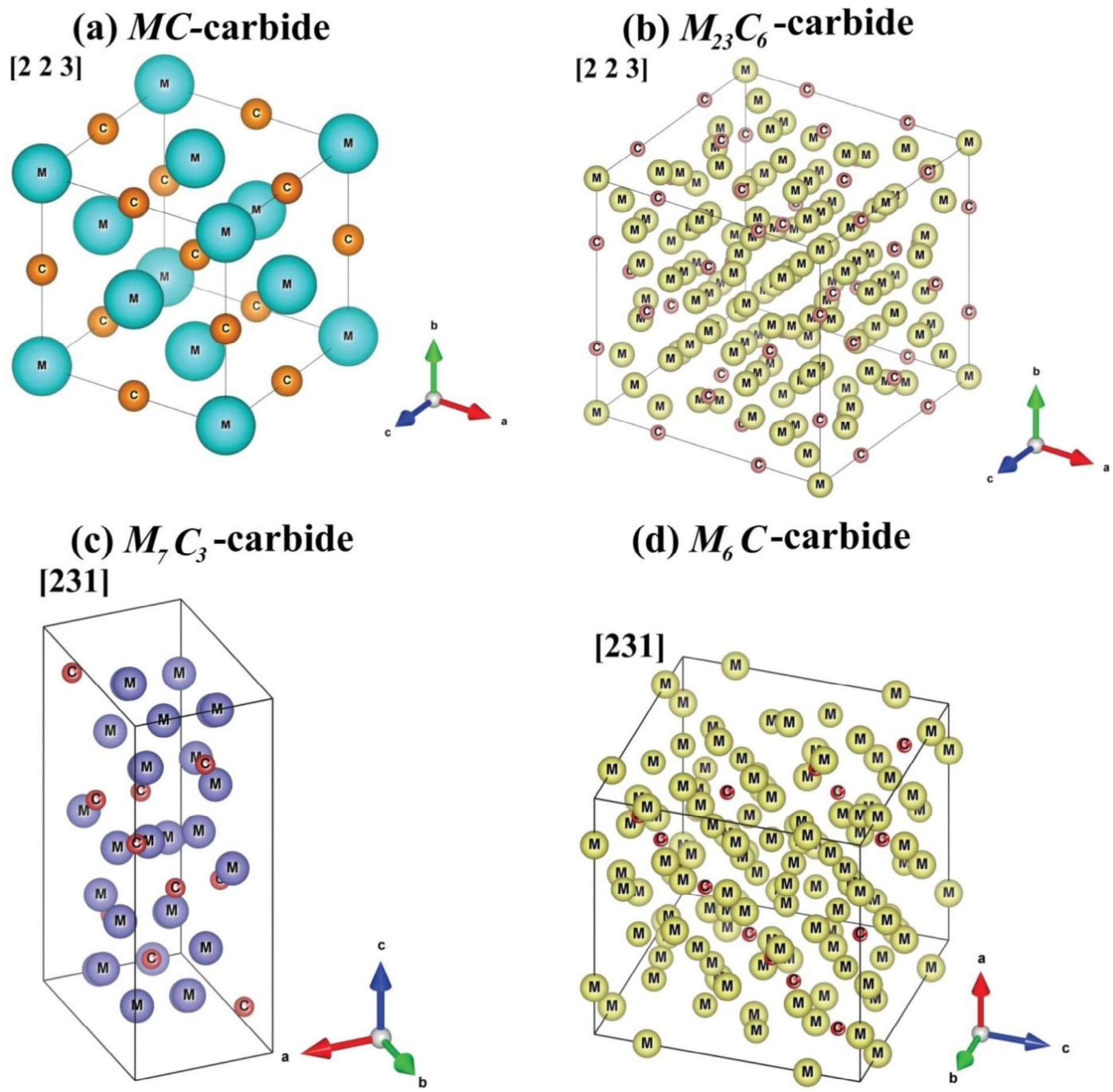

Figure 2.6. Line sketch of crystal structure of (a) *MC*-carbide, where *'M'* represents the *Ti* and *Nb* elements; (b) $M_{23}C_6$-carbide, where *'M'* represents the *Cr, Fe* and *Ni*; (c) M_7C_3-carbide, where *'M'* represents the *Cr;* (d) M_6C-carbide, where *'M'* represents the *Mo* and *W*.

2.3.6.2. $M_{23}C_6$ -carbides:

These carbides form in alloys with moderate-to-high chromium content and may form as primary or secondary carbides. Primary carbides, like *MC* carbides, form during solidification, blocky in nature and do not follow any orientation relationship with matrix. Secondary carbides form during heat treatment or service (in 760-980°*C* temperature regime), either by degeneration of MC-carbides or from residual carbon available in matrix. Decomposition reaction of MC-carbides is given below:

$$MC + \gamma \longrightarrow M_{23}C_6 + \gamma' \qquad \text{...(ii)}$$

They form mainly at grain boundaries in irregular, rounded or blocky shape [51], Figure 2.5(e) shows Cr-rich fine irregular shaped $M_{23}C_6$ -carbides along grain boundaries in a heat treated Ni-base superalloy [92]. Sometimes they precipitate out as continuous or discontinuous (zipper like) grain boundary films which degraded the ductility and rupture life of the alloy. Secondary $M_{23}C_6$-carbide have a complex cubic structure (Figure 2.6(b)) and follow a cube-to-cube orientation relationship with matrix. Their lattice parameter generally three times that of the γ-matrix

2.3.6.3. M_7C_3-carbides:

M_7C_3-carbides have complex orthorhombic structure which is shown in Figure 2.6(c) and are not widely observed in Ni-base superalloys. It is found in a Ni-Cr-Ti-Al (Nimonic 80A) superalloy as Cr_7C_3 precipitates in blocky form at grain boundaries after heating at temperature higher than 1000°C. An addition of elements such as Co, Mo, W, or Nb to Ni-base superalloys prevents formation of M_7C_3. Figure 2.5(h) shows regular shaped Cr_7C_3 carbides (marked by arrows) in a heat treated $NiCrTaAlC$-alloy [95].

2.3.6.4. M_6C-carbides:

M_6C carbides have complex cubic structure (Figure 2.6(d) and form in alloys containing Mo and/or W more than 6-8 *at.*%. These carbides may contain some amounts of Cr, Ni, Nb, Ta, and Co in their solid solutions. They precipitate out in the temperature range 816-982°C having blocky morphology at grain boundaries and Widmanstatten morphology at intragranular sites. Figure 2.5(f) shows the Mo and W-rich blocky M_6C-carbides in a heat treated Ni-base superalloy [93]. They control the grain size during processing if present at grain boundaries. Widmanstatten morphology of these carbides should be avoided for better ductility and rupture life [53].

2.3.7. *MN*-nitrides:

MN-nitrides have a cubic crystal, structure similar to *MC*-carbides shown in Figure 2.7(a), and formed in alloys containing *Ti, Nb* or *Zr*. They form in molten state of the alloy in small sizes with square to rectangular shapes [100], Figure 2.5(g) shows *TiN*-nitrides in a heat treated *IN-718* [94]. They are not affected by heat treatment as they are insoluble to the melting point of the alloy [44]. They are generally present in very small amount so do not have any notable effect on properties of the alloy.

2.3.8. M_3B_2-and M_5B_3-borides:

M_3B_2- and M_5B_3-borides are hard particles and have tetragonal crystal structure shown in Figures 2.7(b) and 2.7(c), where '*M* ' elements can be *Mo, Ta, Nb, Ni, Fe, Cr* or *V*. They are observed in blocky to irregular morphology in *FeNi*- and *Ni*-base alloys when B > about 0.03 *at.*%. Figure 2.5(l) shows the *Cr* and *M*-rich irregular shaped M_3B_2-borides in *MAR-M004 Ni*-base superalloy [98]. *Mo*-rich fine M_5B_3-borides at grain boundary in heat treated *IN-792* are shown in Figure 2.5(m) [99]. Borides form mainly at grain boundaries and impart strength to an alloy in a manner similar to that of carbides, and are favourable for creep rupture properties [88].

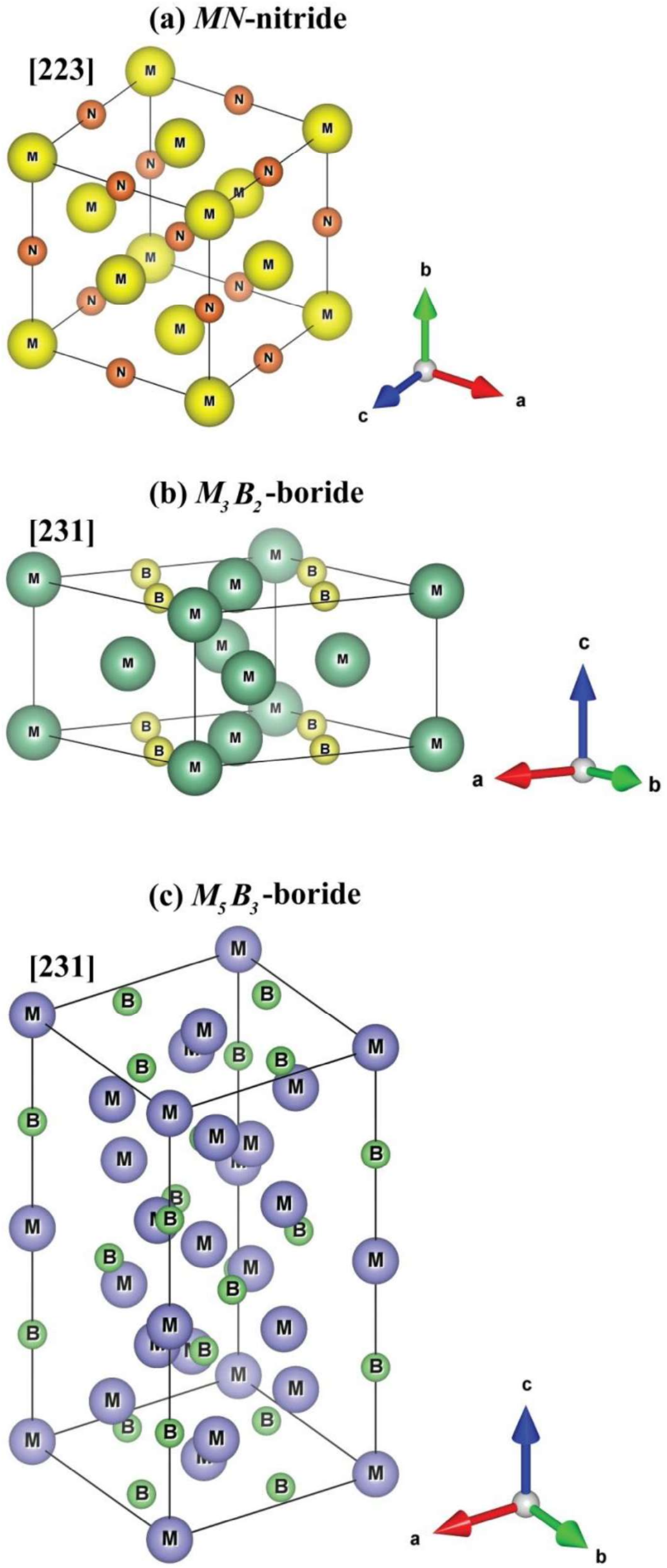

Figure 2.7. Line sketch of crystal structure of (a) *MN*-nitride, where *'M'* represents the *Ti, Nb* and Zr elements; (b) M_3B_2-boride, where *'M'* represents the *Mo, Ta, Nb, Ni, Fe* and *V*; (c) M_5B_3-boride, where *'M'* represents the *Cr*.

2.3.9. *TCP*- phases:

Topologically close packed (*TCP*) σ-, μ-, and Laves-phases (with X_AY_B, $X_{A'}Y_{B'}$ and X_2Y stoichiometry, respectively) are hard and brittle in nature, their crystal structures are shown in Figure 2.8. They are undesirable phases and form in alloys with relatively high amounts of *Cr, Mo* and *W* under certain conditions [101]. *TCP*-phases deteriorate solid solution strengthening of alloys by depleting refractory elements from the matrix [53, 88, 102-105]. They precipitate out in irregularly shaped globules, plate and needle like morphology. They act as crack initiation sites and degrade the mechanical properties of the alloy, like decrease in rupture strength, ductility, fracture life and *LCF* life of the alloy [51]. Their embrittlement effect is more pronounced at low temperatures and high strain rates [106]. μ-phase forms at higher temperatures in alloy with high contents of *Mo* and *W.* Figure 2.5(k) shows the *Mo*, *W* and *Cr*-rich needle shaped μ-phase precipitates in a heat treated *Ni*-base *K-465* superalloy [97]. Laves-phase precipitates out in alloys with high contents of *Nb, Ti* and *Mo* at higher temperatures. Figure 2.5(i) shows typical Fe_2Nb-type elongated Laves phase particles in a γ'-strengthened alumina forming austenitic alloy [96]. Alloys containing high contents of *Mo* and *Co* are prone to form σ-phase after extended exposure between 540-980°*C,* as observed in a heat treated *GTD111* based *Ni*-base superalloy (Figure 2.5(j)) [86].

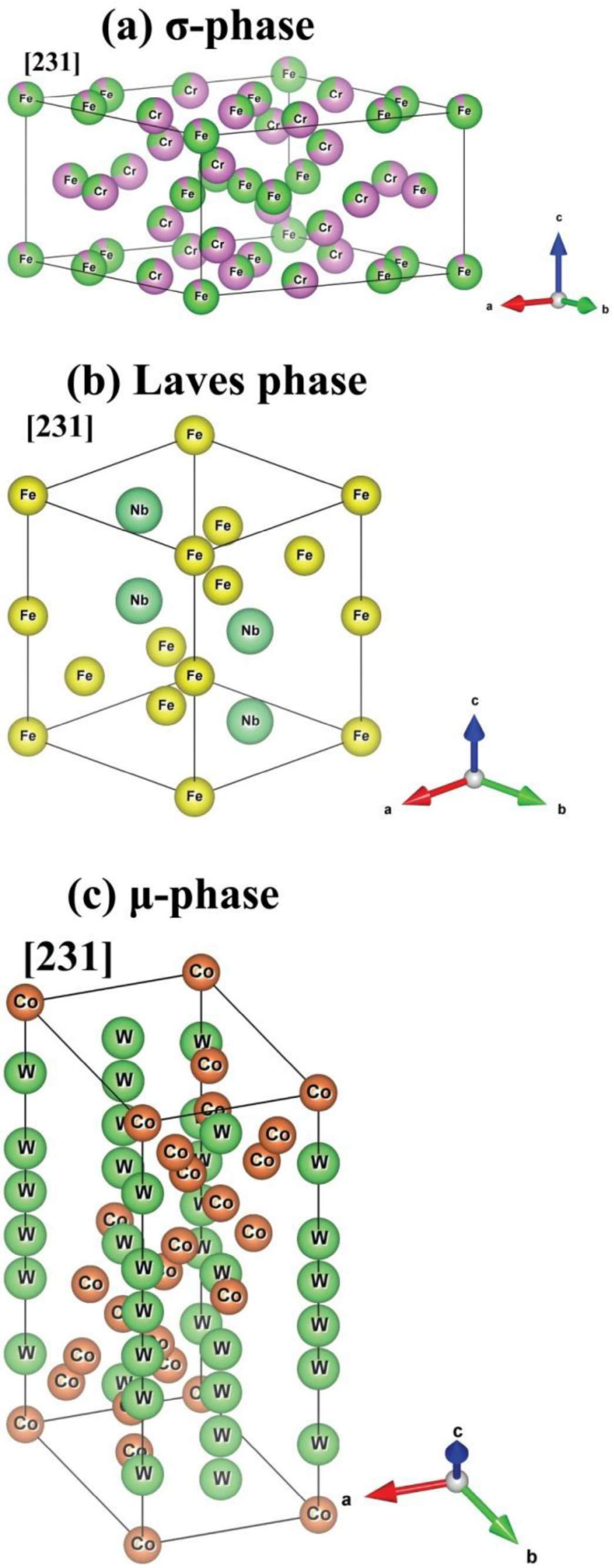

Figure 2.8. Line sketch of crystal structure of (a) σ (X_AY_B)-phase; (b) Laves (X_2Y)-phase; (c) μ ($X_{A'}Y_{B'}$)-phase, where *X* represents *Fe, Ni* and *Co* and *Y* represents the *Mo, Ta, Cr* and *Nb*.

2.4. Precipitation strengthening mechanisms:

In precipitation hardened alloys, precipitates act as barrier to dislocation movement. Strengthening from these particles depends upon their morphology, size and volume fraction. Dislocations need extra stress to either: (i) by pass through them by shearing when they are small and coherent; and, (ii) by bowing around them when they large, strong and impenetrable The two different modes of retardation are depicted in Figure 2.9.

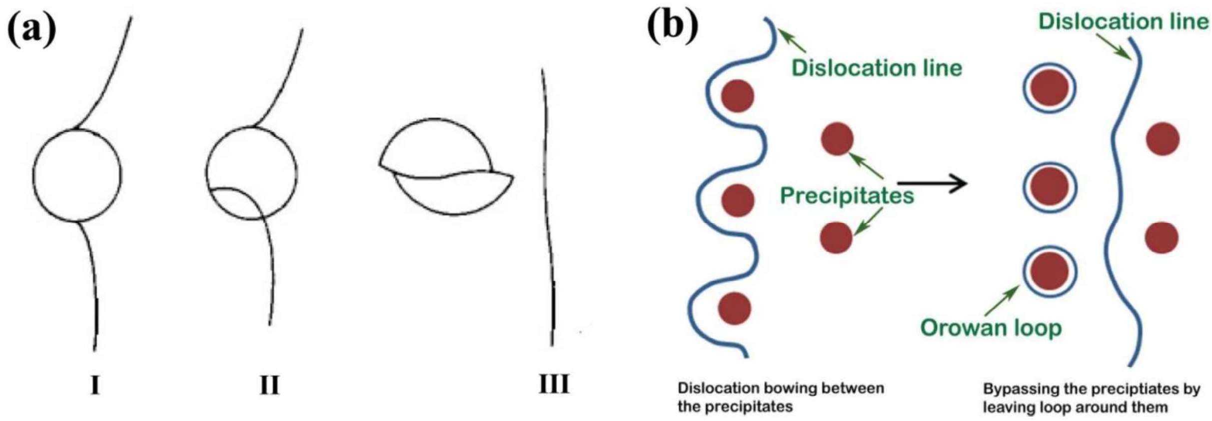

Figure 2.9. (a) Schematic of particle cutting by dislocation [107]; (b) Orowan looping model [108].

It is clear from Figure 2.9 that moving dislocations would cut the particles for smaller sizes, while would create a loop around particles for larger sizes. Out of above two modes, active mechanism of dislocation movement would be controlled by following factors: particle size (*d*), their volume fraction (*f*) and inter-particle spacing (λ). These three factors are interrelated and given by equation (iii) [107],

$$\lambda = \frac{2(1-f)d}{3f} \quad \ldots\text{(iii)}$$

For a given volume fraction, strengthening by rod and plate shape particles has been shown to be twice that of by spherical particles in both the modes [107, 109, 110].

Figure 2.10 shows a schematic variation of strength with particle size [111]. It is clear from Figure 2.10 that initially strength increases with increasing precipitate size, after a critical size of particles strength starts to decrease with increase in size. For cutting mechanism, the intrinsic properties of the particles, like coherency strains, ordered structure, interfacial energy and morphology, stacking fault energy, modulus effect and lattice friction stress, are of importance for alloy strength. All these factors together lead to increase of strength with particle size and volume fraction. For bowing mechanism alloy strength is independent of particle properties and strongly depends on particle size and morphology [107, 110].

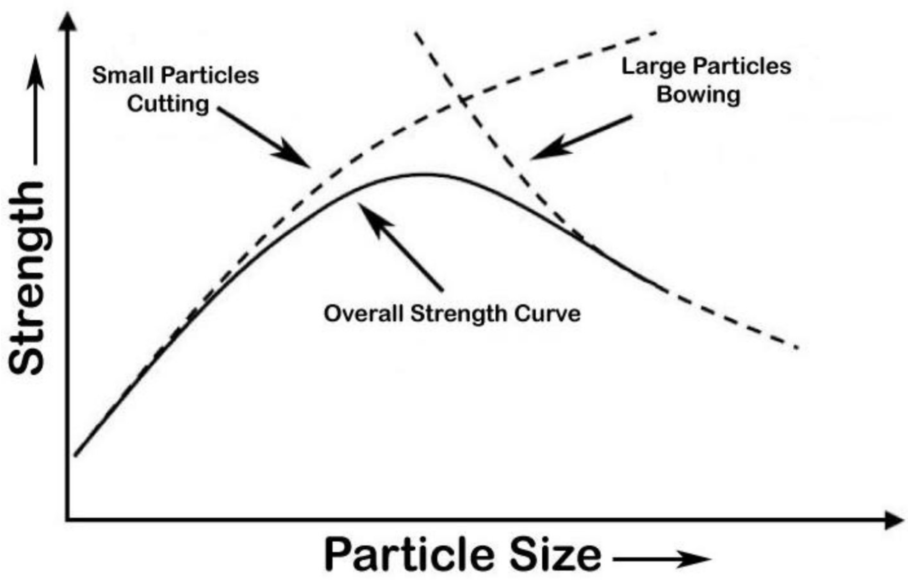

Figure 2.10. Schematic for variation of strength with particle size [111].

In under-aged condition, cutting is dominated while bowing dominates in over-aged condition. In bowing, dislocations create a loop around the particles which raises resistance for forthcoming dislocations thus Orowan bowing mechanism leads to higher work hardening rate in the alloy [107].

2.5. Oxidation and corrosion behaviour:

At elevated temperatures superalloys degrade by oxidation, carburization, nitridation, sulfidation, and/or halogenation. Each type of degradation is caused by specific corrosive media and may be minimized by the addition of appropriate alloying elements (see Table 2.4). In superalloys protection against any environmental media is mainly provided by *Al* and *Cr* in form of Al_2O_3 and Cr_2O_3 oxide layer. Out of these two Cr_2O_3 is most effective at temperatures below 870°*C*, while Al_2O_3 layer is protective at temperatures up to the melting points of the alloys. Resistance to degradation can be avoided by two means: either by making the alloy oxidation resistant by tailoring the composition consistent with mechanical properties requirement or by suitable protective coating on exposed surfaces [44, 48].

Table 2.4. Role of alloying elements in resistance against degradation in different environment [44].

Element	Effects on alloy
Cr	Improves oxidation, sulfidation and carburization resistance
Si	Improves oxidation, nitridation, sulfidation and carburization resistance
Al	Improves oxidation, nitridation, sulfidation and carburization resistance
Mo, W	Beneficial in reducing environment
Yttrium, rare earth elements	Improves oxidation, nitridation, sulfidation and carburization resistance
Nb	Improves carburization resistance
C	Improves carburization resistance

CHAPTER 3

EXPERIMENTAL METHODS

This chapter includes details of the alloy studied, heat treatments involved and various techniques to characterize and analyze microstructure and mechanical properties of the alloy.

3.1. Alloy studied:

Alloy 693 used in present study was prepared by using sequential melting routes of vacuum induction followed by vacuum arc melting at *MIDHANI,* Hyderabad. The alloy was received in the wrought condition in form of sheet of 10*mm* thickness.

Chemical analysis of major alloying elements was carried out using inductive coupled plasma optical emission spectroscopy (*ICP-OES*) technique, while *C*, *S* and *N* were analyzed using combustion analysis. Table 3.1 gives the chemical composition of the alloy studied, which was within the range of nominal composition of an Alloy 693 [2].

Table 3.1. Chemical Composition of Alloy 693 [2]**.**

	Ni	***Cr***	***Fe***	***Al***	***Ti***	***Nb***	***Mn***	***S***	***C***	***N***	***Cu***
wt.%	*Bal.*	27.0-31.0	2.5-6.0	2.5-4.0	1.0 *max.*	0.5-2.5	1.0 *max.*	0.01 *max.*	0.15 *max.*	-	0.5 *max.*
wt.%	58.42	31.26	3.98	3.94	0.34	1.53	0.20	0.01	0.08	0.02	-
at.%	53.81	32.51	3.86	7.90	0.38	0.89	0.20	0.01	0.37	0.06	-

3.2. Heat treatment schedules:

Alloy was solutionized at 1100°*C* for 2.0*h* followed by water quenching to dissolve most of the secondary phases and to retain the alloy in a single *γ*-phase. Solutionized samples were isothermally aged at 800°*C*, 850°*C*, 875°*C*, 900°*C*, 925°*C* and 950°*C* temperatures for series of time intervals of 0.5, 1.0, 2.0, 5.0, 20 and 100*h* followed by water quenching (typical quenching rate ~ 1000°*C* / *min*). Heat treatments were carried out in well calibrated carbolite tubular furnace with a temperature accuracy of ±10*K*. All samples for heat treatments were sealed in quartz ampoules filled with high purity *He* gas at a pressure of about 150*mm* of *Hg*.

3.3. Experimental techniques:

3.3.1 Specimen preparation:

Standard metallographic specimen preparation methods were employed for optical microscopy (*OM*), scanning electron microscopy (*SEM*), *X*-ray diffraction (*XRD*) and hardness measurements. Specimens were first grinded by abrasive silicon carbide (*SiC*) papers of successive grades (80-2400 grit size papers). Final surface polishing was obtained by 0.04μm colloidal silica suspension solution. Polished specimens were used for microhardness measurements. For *OM* and *SEM* studies, polished specimens were electrochemically etched at room temperature for 10*s* using a 5*V DC* voltage and a solution containing 8*g* CrO_3 and 5*ml* H_2SO_4 in 85*ml* H_3PO_4, to reveal microstructural features [112]. Second phase particles, *e.g.,* carbides and α-phase particles were electrolytically extracted out of the bulk samples by selective dissolution of the matrix in an electrolyte solution containing 10% *HCl* and 1.0% tartaric acid in methanol [10]. Extracted particles were collected on Whatman filter paper for analysis. *XRD* studies were carried out on both polished bulk specimens as well as extracted particles. Transmission electron microscopy (*TEM*) specimens were prepared by thinning down specimens upto 100 -120μm thickness and punching out discs of 3*mm* diameter out of thin foils. These discs were made electron transparent by electrolytic polishing using an electrolyte containing 20% perchloric acid in ethanol maintained at about 20*V DC* voltage and temperature around -40°*C,* in a dual jet Tenupol electro-polishing unit.

3.3.2. Phase identification:

3.3.2.1 *X*-ray diffraction:

Room temperature (*RT*) *X*-ray diffraction (*XRD*) studies were carried out for phase identification using BRUKER make *D*8 discover *X*-ray diffractometer in Bragg-Brentano parafocal geometry. Diffractometer was equipped with *Cu* (λ_{WL} = 1.54$\AA$) radiation source operated at 40kV voltage and 40mA current. Diffraction data was recorded using a Lynx-eye position sensitive detector, which offers high detection efficiency of *X*-ray photons at lower acquisition times.

Table 3.2. Details of the *X*-ray optics used for diffraction experiments.

Radiation source	*Cu* (λ_{WL} = 1.54$\AA$)
Goniometer radius	430mm
Filter	*Ni* (0.012mm)
***X*-ray source mode**	Line mode
Soller slit	2.5° axial divergence
2θ range	40 - 100°
Step size	0.02°
Detector slit	9mm
Detector opening angle	1.959°
***X*-ray beam slit mode**	Fixed opening (0.16°)

Diffractometer was calibrated with standard corundum sample. Phase identification in alloy samples were carried out by comparing peaks position in the diffraction pattern with standard *JCPDS* data. Details of the *X*-ray optics used for diffraction experiments are given in Table 3.2.

3.3.2.2. Neutron diffraction:

Room temperature (*RT*) neutron diffraction studies were carried out for phase identification and lattice parameter determination using *PD*-3 neutron diffractometer facility at DHURVA reactor. Bulk samples were cut into small bars (5 x 5 x 50mm^3) and placed in vanadium cans. Neutron diffraction patterns were indexed for phase identification by comparing peaks position with standard *JCPDS* data. Details of the neutron diffractometer optics used for experiments are given in Table 3.3. Lattice parameters of different phases were determined by Rietveld refinement of the diffraction data. FullProf suite software package [113] was used for lattice parameter determination using Rietveld refinement procedure employing Le-Bail fitting method [114].

Table 3.3. Details of the neutron diffractometer optics used for diffraction experiments.

Radiation source	Neutron (λ_{WL} = 1.48$\mathring{A}$)
Monochromator	Bent perfect *Si*
Flux at sample	7 x $10^7 n/cm^2/s$
Detector	Four linear ^3He *PSD*
2θ range	6-120°
Step Size	0.035°

3.3.3. Microstructural characterization:

3.3.3.1. Optical microscopy:

Primarily microstructure characterization was carried out using optical microscope. An Olympus make (*GX* 51 model) optical microscope was used in bright field (*BF*) mode at different magnifications ranging from 100*X* upto 1000*X*.

3.3.3.2. Scanning electron microscopy:

Carl Zeiss make field-emission scanning electron microscope (*FESEM*) SIGMA model operated at 20*kV* was used for microstructural characterization and microchemical analysis of bulk samples and extracted particles. Microstructural characterization was carried out using secondary electron (*SE*) and backscattered electron (*BSE*) imaging modes. Microchemical analysis was carried out with energy dispersive spectroscopy (*EDS*). *AZTEC* microanalysis software (software version 3.1) manufactured by *M/s* Oxford Instruments *Ltd*, *U.K.* with internal library standards were used to quantify the data.

3.3.3.3. Transmission electron microscopy:

Detailed microstructural characterization was carried out using the transmission electron microscopy technique in conjunction with *EDS* using a *JEOL* 2000*FX* transmission electron microscope (*TEM*) equipped with *W* filament and operated at 160*kV,* a *JEOL JEM 3010 TEM* equipped with LaB_6 filament and operated at 300*kV*. Chemical compositions of phases in *TEM* were determined using *EDS* analysis. Bright field (*BF*) and dark-field (*DF*) imaging techniques were used for microstructural characterization. Ordered phases were imaged in *DF* imaging using superlattice reflections. Selected area electron diffraction (*SAED*) patterns were used in conjunction with *TEM* images to identify the presence of different phases and their orientation relationship with matrix. Kodak photographic films were used to record *SAED* pattern and images. *LIBRA* 200 *FE TEM* operated at 200*kV* was used for obtaining high resolution atomic lattice fringes pattern and digital images were recorded using *CCD* camera equipped with microscope.

3.3.4. Mechanical properties measurements:

3.3.4.1. Hardness testing:

Microhardness measurements were carried out to understand the effect of ageing on hardness properties of the alloy. Microhardness testing was carried out using a Vicker's hardness tester

(*ESEWAY* digital hardness tester) at a load of 1*kgf* and dwell time of 10*s*. Microhardness values are reported as an averages of 10 independent readings on different locations for each specimen.

3.3.4.2. Tensile testing:

RT tensile tests of aged alloys were carried out to interpret the effect of ageing on tensile properties. Tests were carried out using M8 x 1.25 round tensile specimens of aged alloys of 4*mm* diameter and about 20*mm* gauge length as per *ASTM E8* standard [11] in an Instron (Model-1185) screw-driven machine, using a constant strain rate of 0.98 x $10^{-4}s^{-1}$. Tensile properties are reported by averaging two independent tensile tests for each aged condition. In-situ tensile experiments were also carried out on 1*mm* thick flat tensile samples of gauge dimensions 5 x 25mm^2 at a strain rate of 4.0 x $10^{-4}s^{-1}$ on a Kammrath and Weiss microtest stage inside the scanning electron microscope.

3.3.4.3. Impact testing:

Sub-sized *V*-notch Charpy specimens of 5 x 10 x 55mm^3 dimension of aged alloy as per *ASTM A*370 standard [12] were tested at room temperature for impact energy measurement in *ROELL AMSLER RKP*450 machine. Value of impact energies are reported by averaging two independent impact tests for each aged condition.

CHAPTER 4

PRECIPITATION BEHAVIOUR OF γ'-PHASE

Alloy 693 is a γ'-precipitation hardened *Ni*-base superalloy. It has been shown that it is difficult to supress the formation of γ'-precipitates in Alloy 693 by solution treatment (*ST*) [13], because dissolved γ'-precipitates re-appear within the matrix during water quenching (*WQ*). Singh et *al.* [13] have shown that reappearance of these precipitates can only be suppressed when the quenching rate is higher than 4500°*C / min* [13]. This chapter gives a detailed account of the precipitation behaviour of γ'-phase particles under isothermal ageing conditions. Samples were aged isothermally at temperatures ranging from 800-950°*C* for varying times (0.5-100*h*) followed by *WQ*. Microstructural investigations were carried out using scanning and transmission electron microscopes.

4.1. Microstructural studies of Alloy 693:

4.1.1. Solution treated alloy:

Figure 1(a) shows a dark field (*DF*) *TEM* micrograph of the *ST*-alloy showing the presence of fine particles (about 10*nm* size) of γ'-phase distributed homogeneously within the matrix, and presence of carbides at the grain boundary. Figure 1(b) shows a [001] zone axis selected area electron diffraction (*SAED*) pattern from corresponding imaged area revealing reflections at characteristic {100} and {110} superlattice positions corresponding to the γ'-phase. Reflections corresponding to $M_{23}C_6$-carbides are also indexed. This was consistent with results reported earlier [13] for a similar alloy. It was, thus, confirmed that γ'-phase particles could not be suppressed during the solutionizing treatment of the alloy.

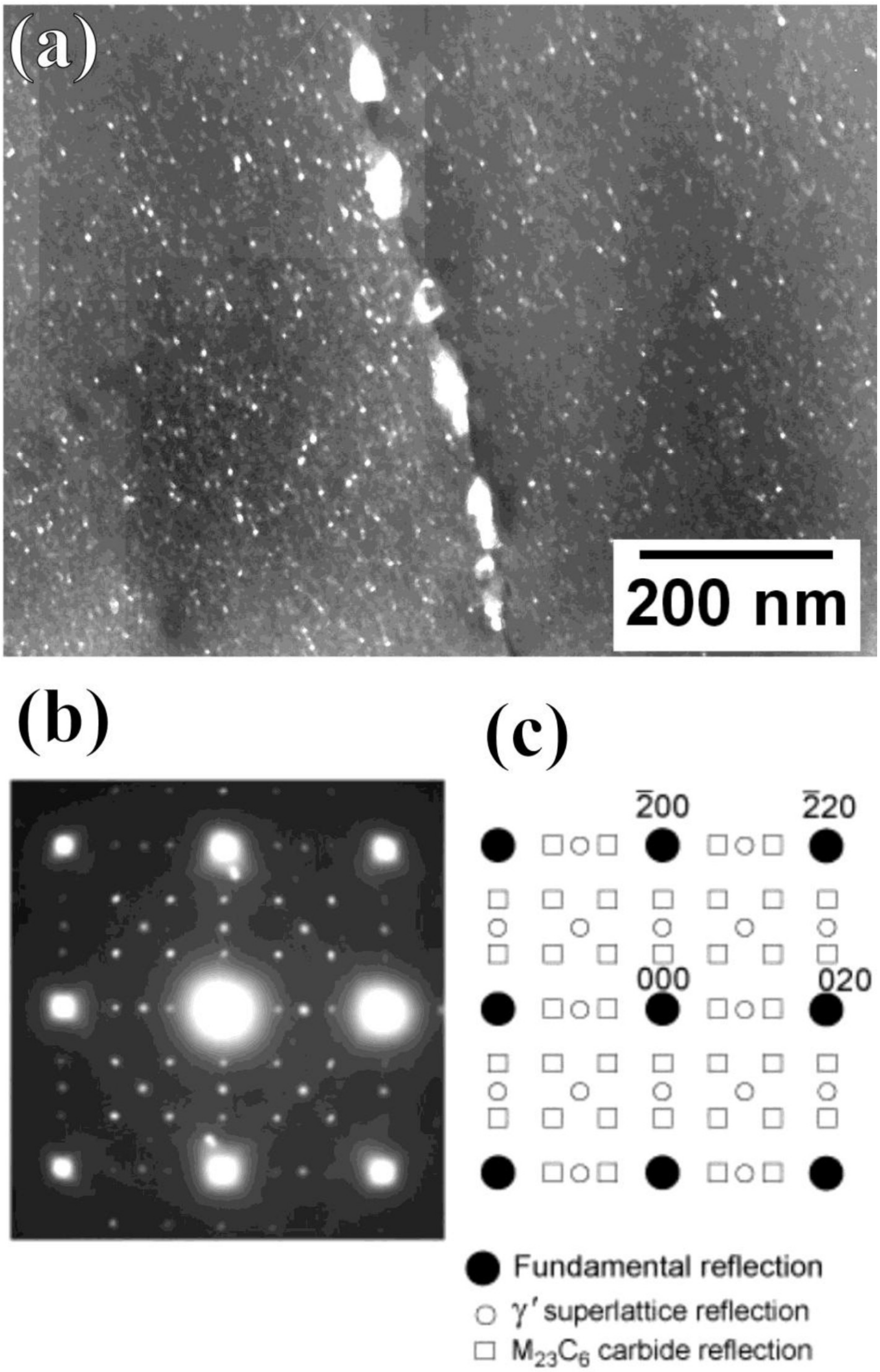

Figure 4.1. (a) *DF TEM* micrograph showing fine particles of the γ'-phase in the *ST*-sample; (b) [001] zone axis *SAED* pattern showing superlattice reflections at {100} and {110} positions characteristic of the γ'-phase, reflection corresponding to $M_{23}C_6$-carbides are also visible; (c) key to Figure (b).

4.1.2. Aged alloys:

Aged samples exhibited a mono-modal distribution of γ'-particles at all temperatures. Figure 4.2 shows a series of micrographs depicting temporal evolution of γ'-phase particles during isothermal ageing at 800-950$°C$ temperature regime for a series of time periods. Tables 4.2 and 4.3 give size (*d*), number density (N_v) and volume fraction (*f*) of γ'-precipitates at different ageing condition. Since the *ST*-sample already contained fine γ'-particles, ageing resulted in their further growth and/or coarsening depending upon ageing temperature. Microstructures of the alloy aged at 800$°C$ exhibited the maximum number density of γ'-particles for all annealing times (Figures 4.2(a-c)). It was clear from Table 4.2 that γ'-particles grew in size continuously with time as their sizes increased monotonically. N_v of particles decreased with the increase of temperature for respective ageing periods (see Table 4.3). At 875$°C$ (Figures 4.2(d– f)), N_v of particles always appeared less than that at 800$°C$ though their sizes were larger in the former due to faster growth kinetics at the higher temperature (see Table 4.2). With further increase in temperature, the N_v of particles decreased while their sizes increased (see Tables 4.2 and 4.3). At higher temperatures, as particles grew, they exhibited a tendency to assume a cuboidal morphology and during later stages of ageing aligned themselves along a specific direction (marked by arrows), which is known to be <100> for these particles [14, 15]. At temperatures between 875-950$°C$, the morphology change over from spherical to cuboidal was seen within 2.0h of ageing. After 100h of ageing at 875$°C$ (Figure 4.2(f)), almost all particles had assumed a cuboidal morphology and aligned themselves. γ'-precipitates remained coherent during growth and even the largest particle observed retained its coherency with the matrix.

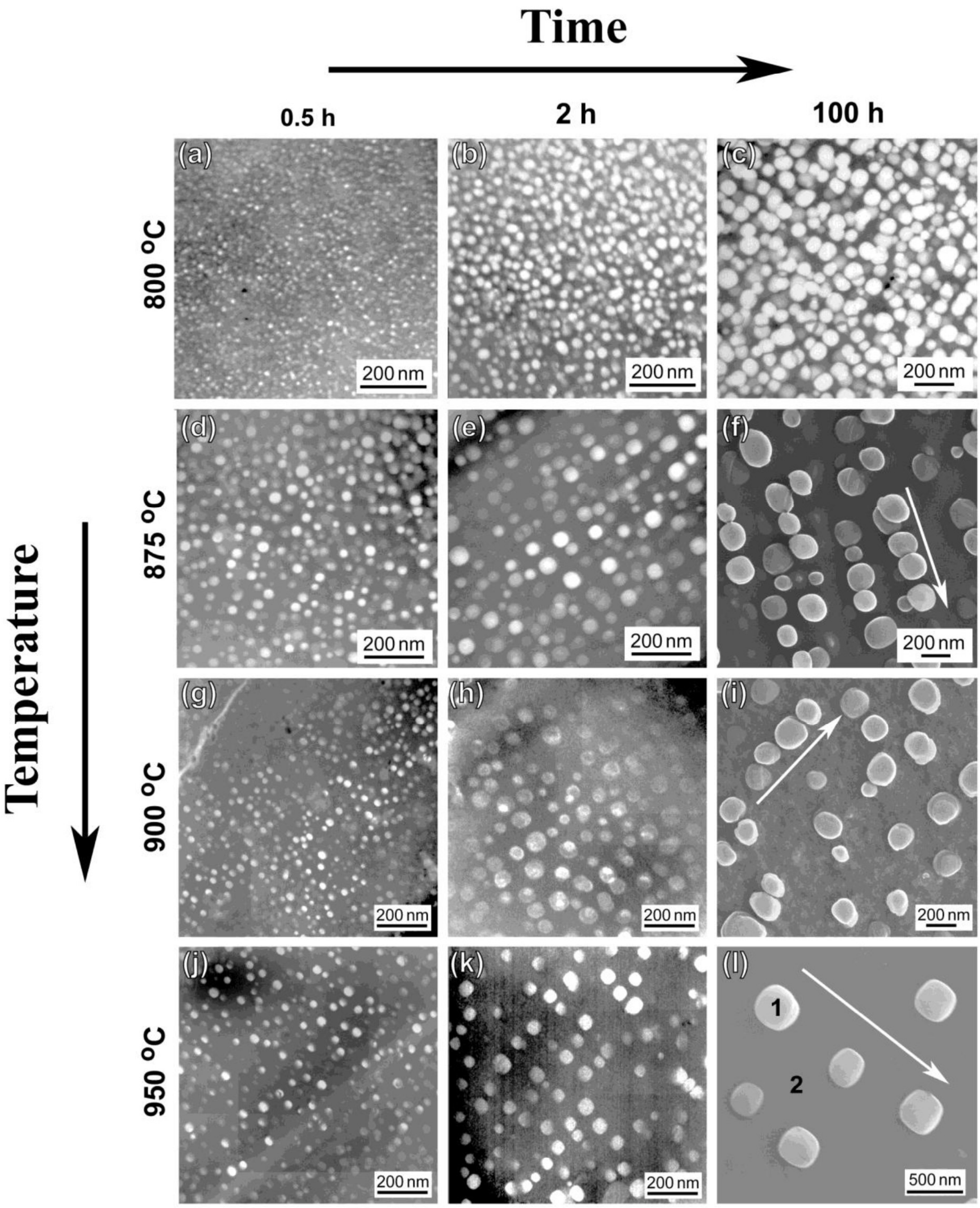

Figure 4.2. Series of electron micrographs depicting temporal evolution of γ'-particles during isothermal ageing at temperatures ranging from 800-950°*C*. (a) 0.5*h* at 800°*C*; (b) 2.0*h* at 800°*C*; (c) 100*h* at 800°*C*; (d) 0.5*h* at 875°*C*; (e) 2.0*h* at 875°*C*; (f) 100*h* at 875°*C*; (g) 0.5*h* at 900°*C*; (h) 2.0*h* at 900°*C*; (i) 100*h* at 900°*C*; (j) 0.5*h* at 950°*C*; (k) 2.0*h* at 950°*C*; (l) 100*h* at 950°*C*. All the micrographs were imaged using *TEM* except for (f), (i) and (l), which were imaged using a *FESEM*.

Table 4.1. Chemical composition of Alloy 693 under study.

	Ni	*Cr*	*Fe*	*Al*	*Ti*	*Nb*	*Mn*	*S*	*C*	*N*
wt.%	58.42	31.26	3.98	3.94	0.34	1.53	0.20	0.01	0.08	0.02
at.%	53.81	32.51	3.86	7.90	0.38	0.89	0.20	0.01	0.373	0.06

Table 4.2. Average sizes (d) of γ'-precipitates in aged samples.

Time (*h*)	**Average size of γ'-precipitates (*nm*)**			
	800°*C*	**875°*C***	**900°*C***	**950°*C***
0.5	8.3 ± 2.3	24.1 ± 8.5	27.9 ± 9.2	43.9 ± 10.0
2.0	18.5 ± 6.8	41.5 ± 10.1	47.0 ± 13.5	78.3 ± 17.1
100.0	81.2 ± 21.4	152.9 ± 43.1	203.2 ± 5.6	341.2 ± 4.2

Table 4.3. Number density (N_v) and volume fraction (f) of γ'-precipitates in aged samples.

Time (*h*)	**No. density of γ'-precipitates (N_v -number.nm^{-2}); volume fraction (f)**							
	800°*C*		**875°*C***		**900°*C***		**950°*C***	
	N_v *10^{-4}	f	N_v *10^{-4}	f	N_v *10^{-4}	f	N_v *10^{-5}	f
0.5	6.79	0.52±0.04	2.38	0.49±0.04	1.54	0.43±0.04	8.47	0.32±0.02
2.0	7.02	0.53±0.07	1.57	0.50±0.04	1.21	0.43±0.05	3.02	0.19±0.03
100.0	7.05	0.78±0.04	0.09	0.62±0.09	0.05	0.37±0.05	0.10	0.19±0.03

It is evident from Tables 4.2 and 4.3 that at higher temperatures, the alloy exhibited an increase in size of γ'-particles and a decrease in their volume fractions with increase of ageing time. At 875°*C*, the alloy exhibited almost constant volume fraction (within experimental errors) of particles though their sizes increased with time, due to faster coarsening kinetics at the higher temperature. Further increase of temperature decreased the number density of γ'-

particles with concomitant increase in their size. This suggested that, at temperatures above 875°C, transformation was dominated by faster coarsening kinetics. Interestingly, at 900°C and 950°C temperatures, the alloy exhibited a larger volume fractions of the γ'-phase during initial ageing times which reduced during prolonged ageing. This behaviour was attributed to under-saturated state of the γ-matrix (with respect to γ'-forming solutes) at 900°C and 950°C temperatures. Due to the under-saturated state of the γ-matrix dissolution of already formed γ'-phase particles would continue till composition of the γ-matrix saturates at these temperatures. This was confirmed on the basis of variation in lattice parameter of γ-matrix during isothermal annealing at 950°C (Table 4.5).

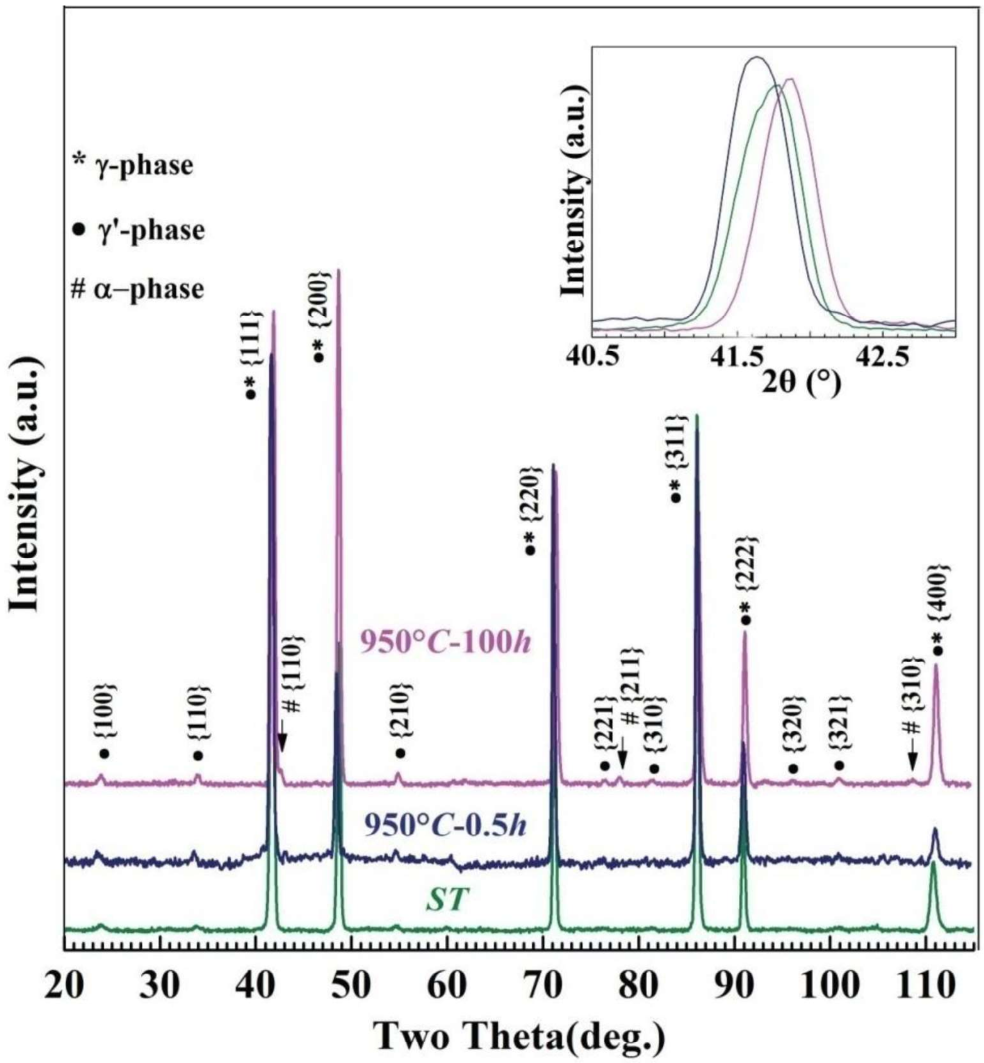

Figure 4.3. Neutron diffraction pattern of ST and aged alloys (950°C-0.5h and 950°C-100h), inset shows a magnified view of the {111} peak.

Lattice parameter values were estimated by Rietveld refinement of neutron diffraction data, using the Le-Bail fitting [114], which fits the whole powder pattern. Figure 4.3 shows the neutron diffraction patterns of *ST* and alloy aged at 950°*C* for 0.5 and 100*h*, which revealed additional peaks along with fundamental reflections of the γ-phase matrix (shown by the * symbol in Figure 4.3). Additional peaks could be indexed corresponding to the γ'-phase (shown by the ● symbol in Figure 4.3) and a α-phase of *Cr* (shown by the # symbol in Figure 4.3), having a *bcc*-structure (which will be discussed in detail in Chapter 5). Table 4.4 gives crystallographic details of different phases used for fitting diffraction patterns. Table 4.5 gives experimentally determined (fitted) cell parameters and errors associated with them for γ- and γ'-phases. From Table 4.5, it is clear that lattice parameter of the γ-matrix in the sample aged for 0.5*h* at 950°*C* was more than that in the *ST*-sample, indicating an increase in solute concentration in the matrix after 0.5*h* of ageing. The observed decrease in the lattice parameter of the γ-matrix after 100*h* was due to the precipitation of a *Cr*-rich α-phase (marked by # in Figure 4.3), which will be discussed in Chapter 5. Compositions of a coarse γ'-precipitate and matrix in sample aged at 950°*C* for 100*h* (regions are marked in Figure 4. 2(l), respectively) are given in Table 4.6.

Table 4.4. Crystallographic details of different phases used in the input file for Rietveld refinement.

Chemical Formula	**γ-phase (*Ni*)**	**γ'-phase (Ni_3Al)**	**α-phase (*Cr*)**
Space group	$Fm\bar{3}m$	$Pm\bar{3}m$	$Im\bar{3}m$
Unit Cell Parameter (Å) **(*JCPDS NO.*)**	3.5238 (00-004-0850)	3.599 (01-071-5899)	2.8839 (00-006-0694)

Table 4.5. Lattice parameter values of γ- and γ'-phases, determined by Rietveld refinement of neutron diffraction data, in different states of the samples.

Specimen State	**Lattice Parameter ($\mathring{A}$)**			
	γ-matrix	**Error (σ)**	**γ'-precipitate**	**Error (σ)**
ST	3.5955	0.4 *E*-4	3.5897	2.7 *E*-4
950°*C*-0.5*h*	3.5988	1.0 *E*-4	3.5897	7.8 *E*-3
950°*C*-100*h*	3.5912	0.3 *E*-4	3.5887	1.4 *E*-4

Table 4.6. Compositions of γ'-precipitate and matrix (restricted to main elements) in sample aged for 100*h* at 950°*C*.

	Elemental composition (in *at.%*)					
	Ni	***Cr***	***Fe***	***Al***	***Ti***	***Nb***
Region 1 **(γ'-precipitates)**	68.77	5.04	1.54	18.49	1.82	4.34
Region 2 **(Matrix)**	57.66	31.04	4.63	5.84	0.23	0.60
Nominal composition in alloy	54.16	32.72	3.89	7.95	0.38	0.90

Figures 4.4 and 4.5 show the frequency-size distribution histograms of γ'-precipitates under different ageing conditions, Figure 4.4 depicts histograms for samples aged at 800°*C* and 875°*C* temperatures, while Figure 4.5 depicts histograms for samples aged 900°*C* and 950°*C* temperatures. Owing to differences in the ranges of particles sizes in samples aged for 0.5, 2.0 and 100*h*, histograms for corresponding sample were obtained using bin sizes of 2.0, 5.0 and 20*nm*, respectively. It was clear from both the figures that particle size distributions were well represented by normal distributions, except for the sample aged for 0.5*h* at 800°*C* (Figure 4.4(a)).

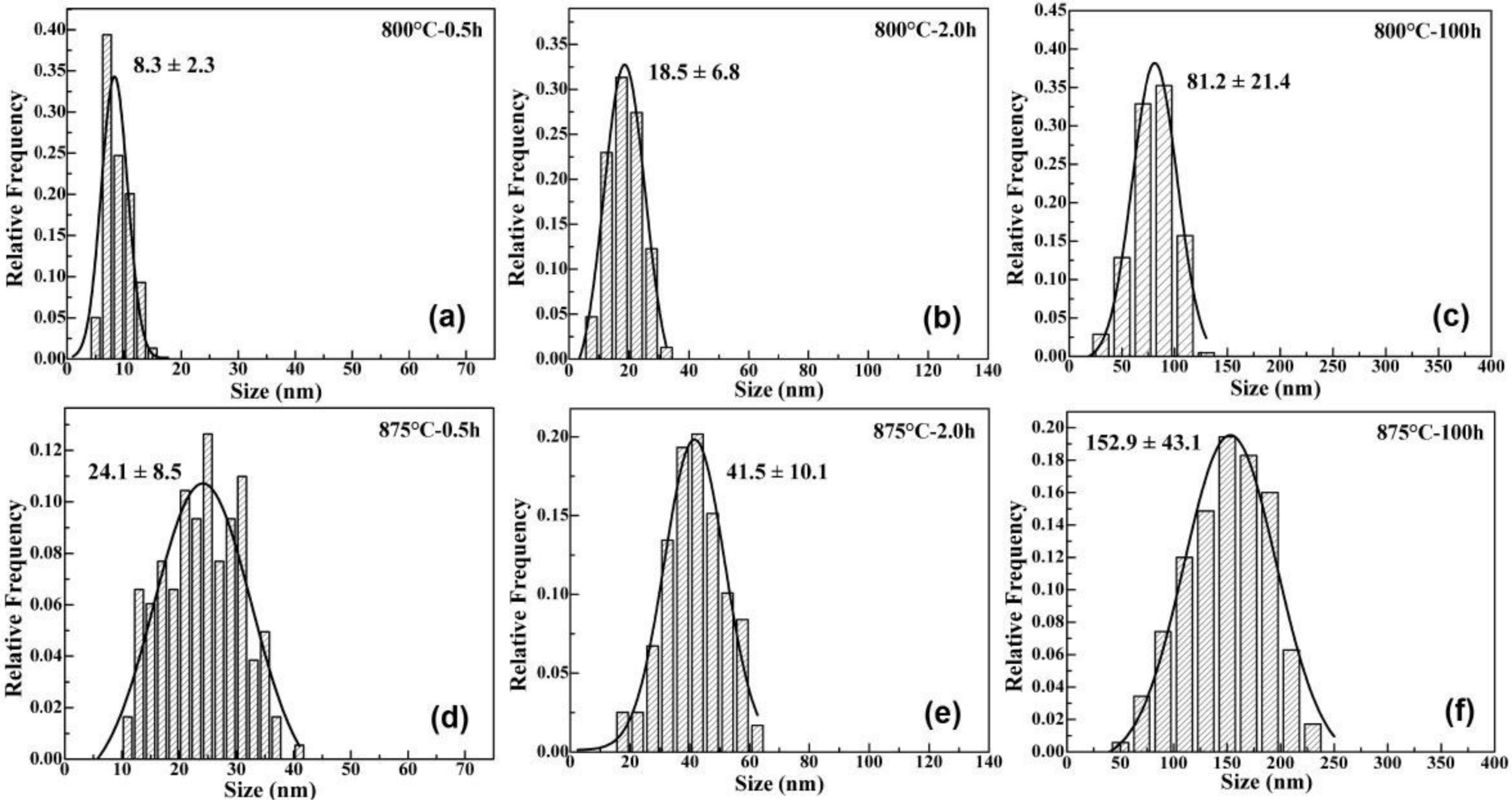

Figure 4.4. Frequency-size distribution histograms of γ'-precipitates in aged samples after ageing for different periods of time at $800°C$ and $875°C$ temperatures: (a) 0.5h at $800°C$; (b) 2.0h at $800°C$; (c) 100h at $800°C$; (d) 0.5h at $875°C$; (e) 2.0h at $875°C$; (f) 100h at $875°C$. Histograms for samples aged for 0.5, 2.0 and 100h were plotted using bin sizes of 2, 5 and 20nm, respectively (see text for details).

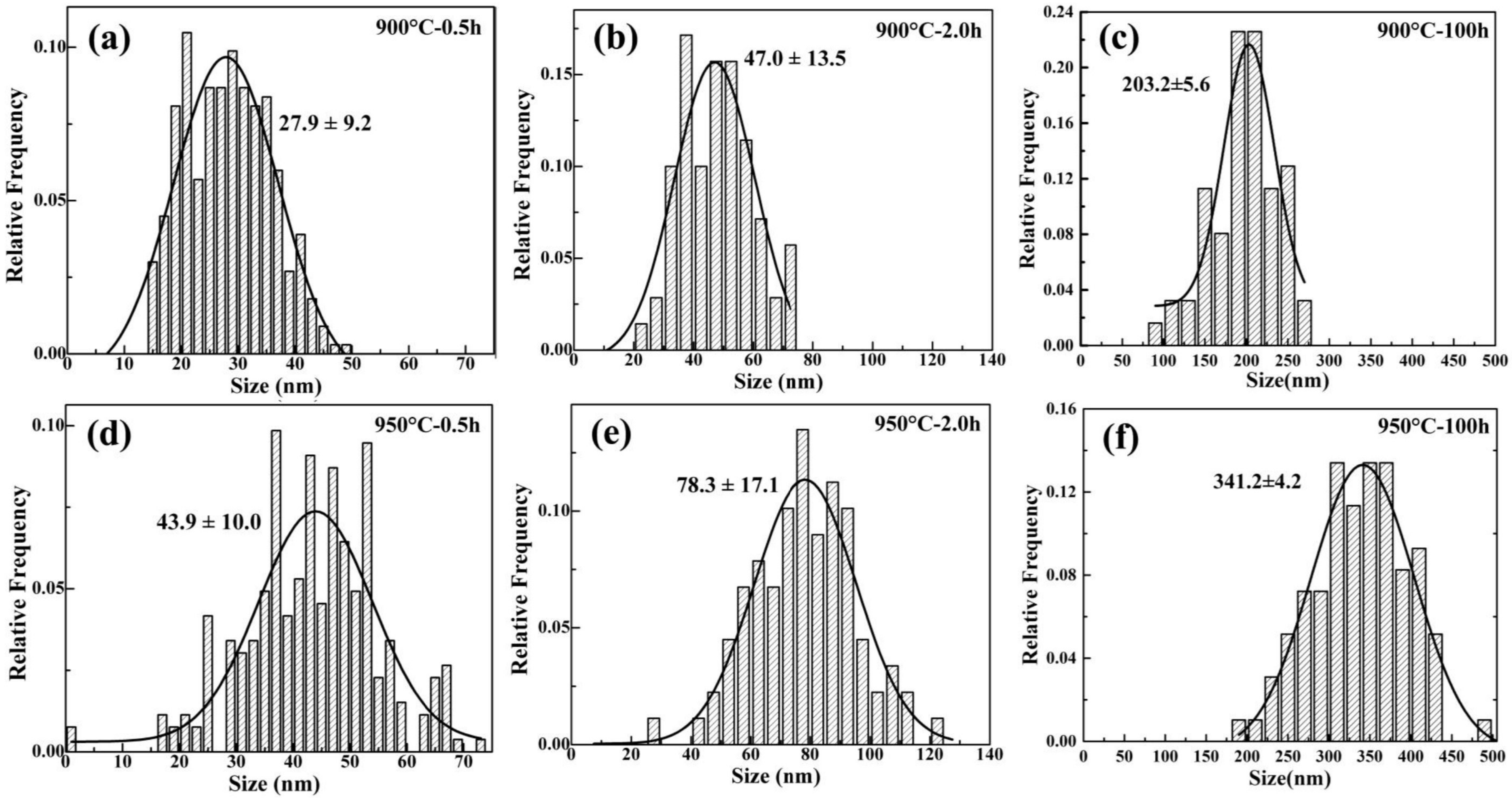

Figure 4.5. Frequency-size distribution histograms of γ'-precipitates in aged samples after ageing for different periods of time at 900°C and 950°C temperatures: (a) 0.5h at 900°C; (b) 2.0h at 900°C; (c) 100h at 900°C; (d) 0.5h at 950°C; (e) 2.0h at 950°C; (f) 100h at 950°C. Histograms for samples aged for 0.5, 2.0 and 100h were plotted using bin sizes of 2, 5 and 20nm, respectively (see text for details).

The skewed nature of the particle size distribution in this sample could be attributed to following factors: (i) high driving force for the nucleation of particle at $800°C$ due to larger under-cooling which could have nucleated new particles during the growth of already existing particles; (ii) experimental limitation of imaging and analysing particles of sizes below $5.0nm$. The fact that the *ST*-sample contained particles of mean size (about $10nm$) larger than those in the sample aged for $0.5h$ at $800°C$ supported that new particles had nucleated during this period. This shifted the mean value towards the lower side and changed distribution from normal to a skewed type. The nature of the distributions for all times remained more or less same for samples aged at 875, 900 and $950°C$ while the average particles sizes increased with time. Further, as mentioned earlier, the number density of particles decreased with time in these samples (see Table 4.3). This confirmed the particles exhibited coarsening behaviour at these temperatures.

4.2. Discussion:

4.2.1 Precipitation behaviour of the γ'-phase particles:

Precipitation is a three step process involving nucleation, growth, and coarsening. According to classical nucleation theory, the rate, J, at which homogeneous nuclei are created per unit volume and time is given by [115],

$$J = n_0 z\, \beta^* exp\, (-\frac{\Delta G^*}{kT})\; exp(-\frac{\tau}{t}) \qquad ...(i)$$

where, n_0 represents the total number of potential nucleation sites, Z, is the Zeldovich factor that takes into account the decomposition of super-critical nucleus due to thermal fluctuation; β^* is the rate at which a single atom joins a critical nucleus to make it supercritical taking into account the long-range diffusive transport of atoms (extremely dependent upon temperature change); k is the Boltzmann constant and T is temperature; τ is the incubation time and t is the time for isothermal reaction. ΔG^* is the main driving force for the formation nucleus and is given by [116],

$$\Delta G^* = \frac{16\pi}{3} \frac{\gamma^3}{(\Delta G_V)^2} \qquad \text{...(ii)}$$

where, ΔG_V is the volume free energy decrease associated with the nucleation event. ΔG_V is proportional to degree of supersaturation (ΔC) and under cooling (ΔT^*) below the equilibrium solvus temperature (T_e). Term $\exp(-\Delta G^*/kT)$ in Equation (i) expresses the probability of forming nuclei and is essentially zero until a critical under-cooling (ΔT_c) is reached after which it rises rapidly.

During nucleation, composition of the matrix remains more or less unchanged. However, continued nucleation occurring with simultaneous growth of the already existing precipitates depletes the matrix from precipitate-forming solutes. As a result, decreases of ΔG_V reduced in magnitude continuously with the nucleation and growth process. Under isothermal conditions, continued growth of the precipitates drives the matrix into a state close to equilibrium when $\Delta C \approx 0$, beyond which coarsening or Ostwald ripening driven by the minimization of the total precipitate surface area occurs.

The overall precipitation behaviour is governed by nucleation rate, growth rate, number density and distribution of nucleation sites, overlap of diffusion fields of transformed volumes and impingement of adjacent transformed volumes [16]. Diffusional transformations are characterized by *C*-shaped time-temperature-transformation (*TTT)* curves governed by the nucleation and growth processes. For a given alloy, ΔC increases with decrease in temperature due to increase in supersaturation at lower temperatures. At temperatures close to T_e, both ΔC and ΔT are small and the transformation is characterized by long incubation periods. At lower temperatures, both ΔC and ΔT are large but slow rates of diffusion limit the transformation rate. A maximum transformation rate is obtained at an intermediate temperature (T_{max}).

Particles number density (N_v) can be related to the nucleation rate (J) as $N_v = J.t$, where t is time. The particle number density therefore increases linearly with time during the nucleation stage for small N_v when particles are uncorrelated. N_v remains roughly constant during the growth stage. In the coarsening stage, the particle number density decreases linearly with time in accordance with Lifshitz and Slyozov [19] and Wagner [20] (*LSW*) theory.

For the present alloy T_e and T_{max} are close to 950°*C* and 875°*C*, respectively [13]. Under isothermal conditions, continuous nucleation and growth of precipitates drive the transformation till matrix composition equilibrates with respect to that of precipitates (*i.e.*, $\Delta C \approx 0$), beyond which coarsening of precipitates driven by the minimization of total precipitate surface area occurs. During ageing at 800°*C*, continuous increase in size as well as volume fraction of γ'-particles indicated their continuous growth till 100*h* suggesting that composition of the γ-matrix remained away from the equilibrium composition till this period. On the other hand, nearly constant volume fraction of precipitates at 875°*C* suggested of their coarsening stage. However, at 900°*C* and 950°*C* temperatures, the alloy exhibited a larger volume fractions of the γ'-phase initially, which reduced during prolonged ageing. This could be attributed to under-saturated state (with respect to γ'-forming solutes) of the γ-matrix at these temperatures. Precipitation of high density of γ'-phase particles during *WQ* (in *ST*-condition) would decrease the concentration of γ'-forming solutes in the γ-matrix to an average composition, defined by $C_{\gamma,T}$, where T represents the temperature up to which diffusion of γ'-forming solutes would be effective. This composition would be lower than the average composition of the alloy. It was not unreasonable to assume that T would be much lower than 900°*C*, which was consistent with an earlier work [13]. This implied that $C_{\gamma,T}$ <

$C_{\gamma,900°C}^{\gamma'}$ and indicated that the γ-matrix in the ST-alloy would be under-saturated with respect to γ'-forming elements at temperatures $900°C$ or higher. This behaviour is schematically illustrated on the $NiAl$-phase diagram [65] in Figure 4.6. This was consistent with higher solubility of solutes at higher temperatures. Further, γ'-particles already present in the γ-matrix of ST-samples would immediately start coarsening when subjected to annealing at $900°C$ or higher temperatures.

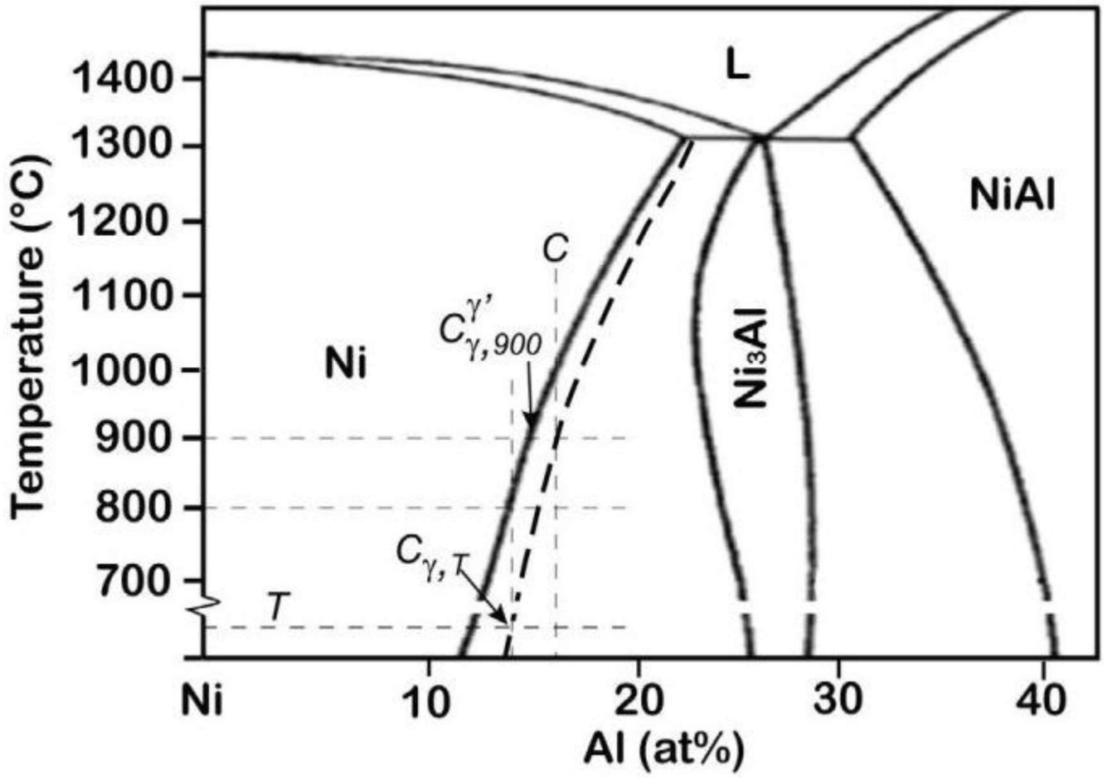

Figure 4.6. A part of $NiAl$-binary phase diagram illustrating a shift of the equilibrium $Ni/(Ni + Ni_3Al)$ phase boundary to metastable state, shown by a broken thick line, after WQ. $C_{\gamma,T}$ denotes average composition of γ'-forming solutes (here represented by only Al) in the matrix after WQ, which is lower than their equilibrium composition at $900°C$, denoted by $C_{\gamma,900}^{\gamma'}$. C represents the average composition of γ'-forming solutes in the alloy and T represents the average temperature upto which diffusion of γ'-forming solutes was effective during WQ (see text for details). Figure is redrawn from reference [7].

Simultaneously, some of them would tend to dissolve to bring the composition of γ'-forming solutes in the matrix to equilibrium values. This tendency was reflected in higher volume fractions of particles observed initially at $900°C$ and $950°C$ temperatures, which decreased during prolonged ageing to equilibrate the matrix compositions at respective temperatures (see Table 4.3). Fixed volume fraction of precipitates, concomitant with decrease in their number density, after $2.0h$ of ageing at $950°C$ (see Table 4.3) indicated of their coarsening stage. Attempts were also made to delineate growth and coarsening stages of γ'-precipitates on the basis of change in lattice parameter of the γ-phase. However, this data could not be utilized due to the precipitation of an α-phase, which also decreased lattice parameter of the matrix [117], during periods that overlapped with coarsening stages of γ'-precipitates.

4.2.2. Morphological evolution of γ'-particles in aged alloys:

Competing factors of γ/γ' interfacial energy and the elastic strain energy arising due to lattice mismatch between matrix (γ) and precipitates (γ') determine the morphological evolution of γ'-precipitates in Ni-base superalloys [23]. In addition, differences in thermal expansion coefficients (α_T) of γ- and γ'-phases at different ageing temperatures may also play a role on morphological changes. Usually lattice parameter increases with temperature at a rate determined by the thermal expansion coefficient of the phase. Owing to stronger bond strengths, ordered phases would have low α_T -values than that of their disordered phases. Differences in the α_T -values of γ- and γ'-phases would therefore increase the strain energy contribution at higher temperatures. In the early stages of precipitation, particles remained spherical due to low interfacial and elastic strain energies, however, latter begin to dominate during growth and coarsening. In general, smaller γ-γ' lattice misfit (ϵ) causes the morphological transition to occur at larger particle sizes because lower elastic strain makes easy growth of γ'-particles [26]. Morphology of particles also depends upon the particles number density (N_v), since the size to which particles can grow is limited by the interaction of strain fields [21], as seen in Figure 4.2(c) (sample aged for 100*h* at 800°*C*). Because of aforementioned factors, morphological transformation from spherical to cuboidal shape occurred at different sizes of particles at different temperatures. During ageing at 800°*C*, γ'-precipitate size increased from an average of 8.3 ± 2.3*nm* (spherical) after 0.5*h* to 81.2 ± 21.4*nm* (spherical) after 100*h* of ageing. Even after ageing for 100*h*, the number density of particles appeared to remain unchanged and particles retained spherical shape after growing to fairly larger sizes. The spherical shapes of particles at this temperature could be attributed to low degree of lattice misfit (ϵ) as a consequence of their limited growth caused by particles impingement. At 875°*C* *TEM* micrographs showed that precipitates size increased from 24.1 ± 8.5*nm* to 152.9 ± 43.1*nm* with increase of ageing time from 0.5-100*h*, respectively. Morphological change over from spherical to cuboidal was seen after 2.0*h* of ageing and the γ'-precipitates developed facets approximately parallel to $\{001\}$. After 100*h* of ageing at 875°*C*, most particles had assumed cuboidal morphology and were aligned in <100> direction. This implied that coarsening of γ'-particles driven by the reduction of interfacial energy already started to operate at this temperature which resulted in their directional distribution and morphological changes, and was consistent with previous works (see, *e.g.*,[118]). Beyond 875°*C,* alloy samples exhibited similar morphological transition from spherical to cuboidal shapes as found at 875°*C* with exception of reduced particle densities and their volume fractions at higher temperatures (see Figure 4.2 and Table 4.3).

4.2.3. Coarsening kinetics of γ'-particles in aged alloys:

A large body of work has demonstrated that coarsening of γ'-particles in a γ-matrix conform volume diffusion controlled behaviour through matrix. Such a volume diffusion controlled coarsening behaviour has been modelled by the *LSW* theory [19, 20]. The theory is strictly applicable only to the growth of an infinitesimally small volume fraction of precipitates in a dilute fluid matrix, though it is able to predict the coarsening behaviour in concentrated alloys like superalloys, as well. According to *LSW* theory, the average size of the particles obeys the law

$$r^3 - r_0^3 = K.(t - t_0) \qquad \text{...(iii)}$$

where, r is average radius of particles at a time t, r_0 is average radius at time t_0 (beginning of coarsening stage), and K is rate constant [119].

In general, coarsening follows $r^{\beta} = K.t$ behaviour, where exponent is β governed by the mode of coarsening. If the coarsening follows a matrix diffusion controlled growth behaviour, $\beta = 3$, and if diffusion across the matrix/precipitate interface controls the growth, $\beta = 2$ [23]. To determine the coarsening mechanism in Alloy 693, logarithm of the average precipitate size (*i.e.*, $\log_e r$) versus logarithm of the ageing time ($\log_e t$) for all the ageing temperatures were plotted as shown in Figure 4.7(a). This analysis was restricted to samples aged at temperatures 875 °*C* and above, as the sample aged at 800 °*C* still exhibited a particles growth behaviour even after 100*h* of ageing. Radii of particles were obtained from average particle sizes for spherical shapes and as a half of the average length of cube diagonal for cuboidal shapes. Inverse of the slope of the linear-fit of $\log_e r$ *vs.* $\log_e t$ were taken to estimate exponents β at respective temperatures (Table 4.7). All the values were nearly same and were close to 3. Thus, the experimentally determined exponents of coarsening suggest it to be volume controlled diffusion as suggested by *LSW* theory. Average particle size raised to the third power (*i.e., r^3*) versus annealing times (t) were plotted for all the temperatures ranging from 875-950°*C* (Figure 4.7(b)). Coarsening rate constant (K) was estimated from the slope of linear fits of respective plots of the cube of particle size versus time (Figure 4.7(b)) while corresponding intercepts gave mean initial particle sizes (r_0). On the basis of r^3 versus t plots (Figure 4.7(b)), coarsening rate constants (K) at temperatures 875, 900 and 950°*C* were calculated and given in Table 4.7. The values of K suggested that γ'-particles coarsened more rapidly at high temperatures mainly due to easier diffusion of elements.

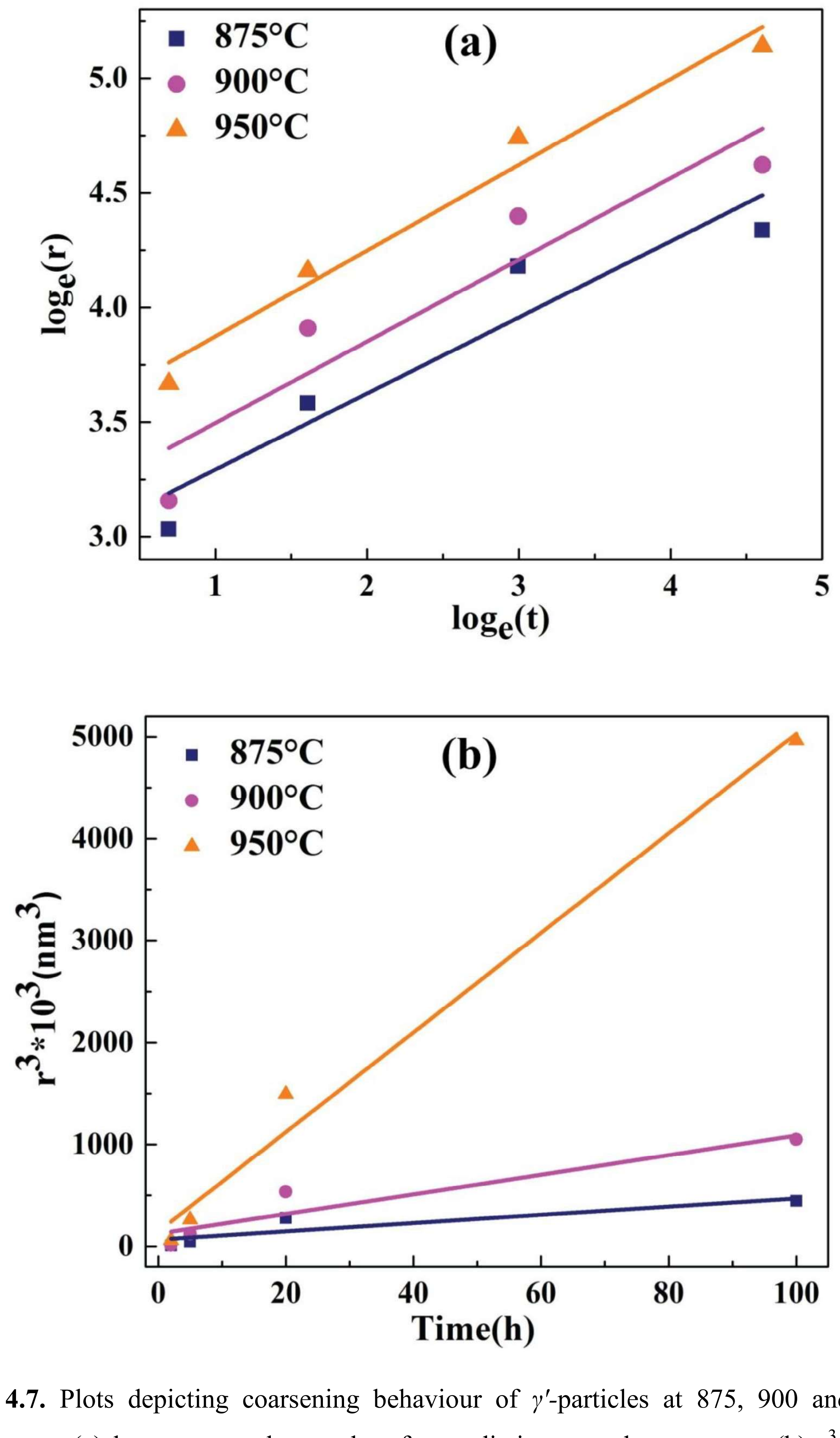

Figure 4.7. Plots depicting coarsening behaviour of γ'-particles at 875, 900 and 950°*C* temperatures: (a) $\log_e r$ versus $\log_e t$ plots for predicting growth exponent; (b) r^3 versus t plots for estimating the coarsening rate constant (K).

Table 4.7. Calculated temporal exponent and rate constants for coarsening behaviour of γ'-precipitates in Alloy 693.

	Ageing temperature (°*C*)		
	875	**900**	**950**
Temporal exponent (β)	3.0	2.9	2.7
Rate constant, K (m^3/s)	1.12×10^{-27}	2.67×10^{-27}	13.57×10^{-27}

4.2.4. Stability of the γ'-phase:

It has been shown earlier in Table 4.6 that alloying elements (*Ti, Nb, Cr* and *Fe*) present in the alloy substitute for *Ni* and *Al* atoms in the γ'-phase. Such elemental substitution have been reported to affect phase stability of γ'-precipitates that results in microstructural instability which ultimately affect properties of the alloy [61]. In the γ'-phase, *Ti* and *Nb* preferentially substitute *Al* lattice sites while *Cr* and *Fe* substitute *Ni* atoms. Presence of these elements in the alloy alters the volume fraction of these precipitates [5, 62, 63]. Addition of these elements (see Figure 2.3 in Chapter 2), however, is limited to certain extent beyond which they promote formation of detrimental phases along with γ'-phase [5, 62, 63]. For instance, addition of *Ti* beyond 16*at.%* in binary *NiAl* alloy promotes the η-phase (hexagonal Ni_3Ti-phase) as mentioned already in Chapter 2 (see Figure 2.3(a) in Chapter 2). Similarly, addition of more than 8*at.% Nb* in binary *NiAl* alloy would form δ-phase (orthorhombic Ni_3Nb-phase) as shown in Figure 2.3(b) of Chapter 2. According to Pearson and Hume-Rothery [120], stability of the γ'-phase of Ni_3X compounds is related to atomic size of *X* elements - *Al, Ti* and *Nb.* An increase of atomic size decreases stability of the γ'-phase and makes it metastable beyond a certain concentration of *X* element. Mishima et *al.* [61] have shown that *Nb* can be dissolved up to about 8*at.%* in the γ'-phase of *Ti*-free alloys, and would further decrease in presence of *Ti*. This could be explained on the basis of free electrons per atom (*e/a* ratio) of alloy that governs the stability of competing structures of Ni_3X stoichiometry in accordance with the scheme proposed by Sinha [66]. According to this scheme, the *e/a* ratio for the stability of the $L1_2$, $D0_{24}$ and $D0_a$ structures of Ni_3Al, Ni_3Ti and Ni_3Nb compounds, respectively, correspond to 8.25, 8.5 and 8.75 (Table 4.8).

Addition of *Ti* and/or *Nb*, having free electrons more than those in *Al*, increases the *e/a* ratio and destabilizes $L1_2$ structure. In the absence of *Ti*, the maximum reported solubility of *Nb* in the Ni_3Al is about 8*at.*% giving an *e/a* ratio ≈ 8.41 for the $Ni_3(Al_{0.68}Nb_{0.32})$ compound. In the present study, *e/a* value for γ'-phase is ~8.20 (calculated from composition given in Table 4.6) which is close to the value of Ni_3Al-phase and thus is a stable phase.

Table 4.8. Numbers of free electrons per atom (*e/a* ratio) for different metals and compounds relevant to γ'-precipitation in Alloy 693.

Composition	*e/a* ratio	Ground state of the equilibrium ordered structure
Ni	10	-
Al	3	-
Ti	4	-
Nb	5	-
Ni_3Al	8.25	$L1_2$
Ni_3Ti	8.5	$D0_{24}$
Ni_3Nb	8.75	$D0_a$

4.3. Summary:

Precipitation and coarsening behaviour of γ'-precipitates in Alloy 693 followed similar behaviour as reported in many other γ'-precipitate bearing alloys. These precipitates evolved homogeneously throughout the matrix with spherical morphology which tended to change to cuboidal during prolonged ageing and they aligned themselves along <100> directions. γ'-precipitates always maintained coherency with the matrix (upto the largest sizes observed in present study). Formation of these precipitates could be explained by classical nucleation and growth theory. They followed a volume controlled diffusion coarsening kinetics as suggested by *LSW* theory.

CHAPTER 5

MICROSTRUCTURAL STABILITY AT ELEVATED TEMPERATURES

The alloy exhibited a microstructural instability in the form of *Cr* rejection from the matrix, as γ'-phase precipitates grew/coarsened, during prolonged ageing at elevated temperatures. This chapter gives a detailed description of this instability observed during the prsent study.

5.1. Microstructure of the alloy after prolonged ageing:

Optical microscopy of samples aged at 800-900$°C$ for prolonged periods of time exhibited the formation of needle shaped particles (a few of them are marked by arrows in Figures 5.1(c, f, i)). Figure 5.1 also shows a few globular shaped MC and $M_{23}C_6$ type carbides, distributed throughout the matrix as well as at grain boundaries, known to form in *Ni*-base superalloys during solidification [15] . At 950$°C$ temeprature, these new phase particles were even observed after short duration of ageing (Figure 5.2(a)). Temporal evolution of these particels at 950$°C$ is shown in Figure 5.2 (few of them are marked by arrows). These needle shaped particles tend to dissolve at temperatures above 950$°C$ - volume fraction and size of these particles reduced in sample aged at 1000$°C$ for 0.5h and were absent in samples aged at 1050$°C$ for 0.5h (see Figure 5.3). Microstructural observations clearly showed that, for a given time, volume fraction of these particles increased with temperature and reached a maximum value at temperature about 900$°C$ (see Figures 5.1(c, f, i)) above which it decreased (see Figure 5.2(f)).

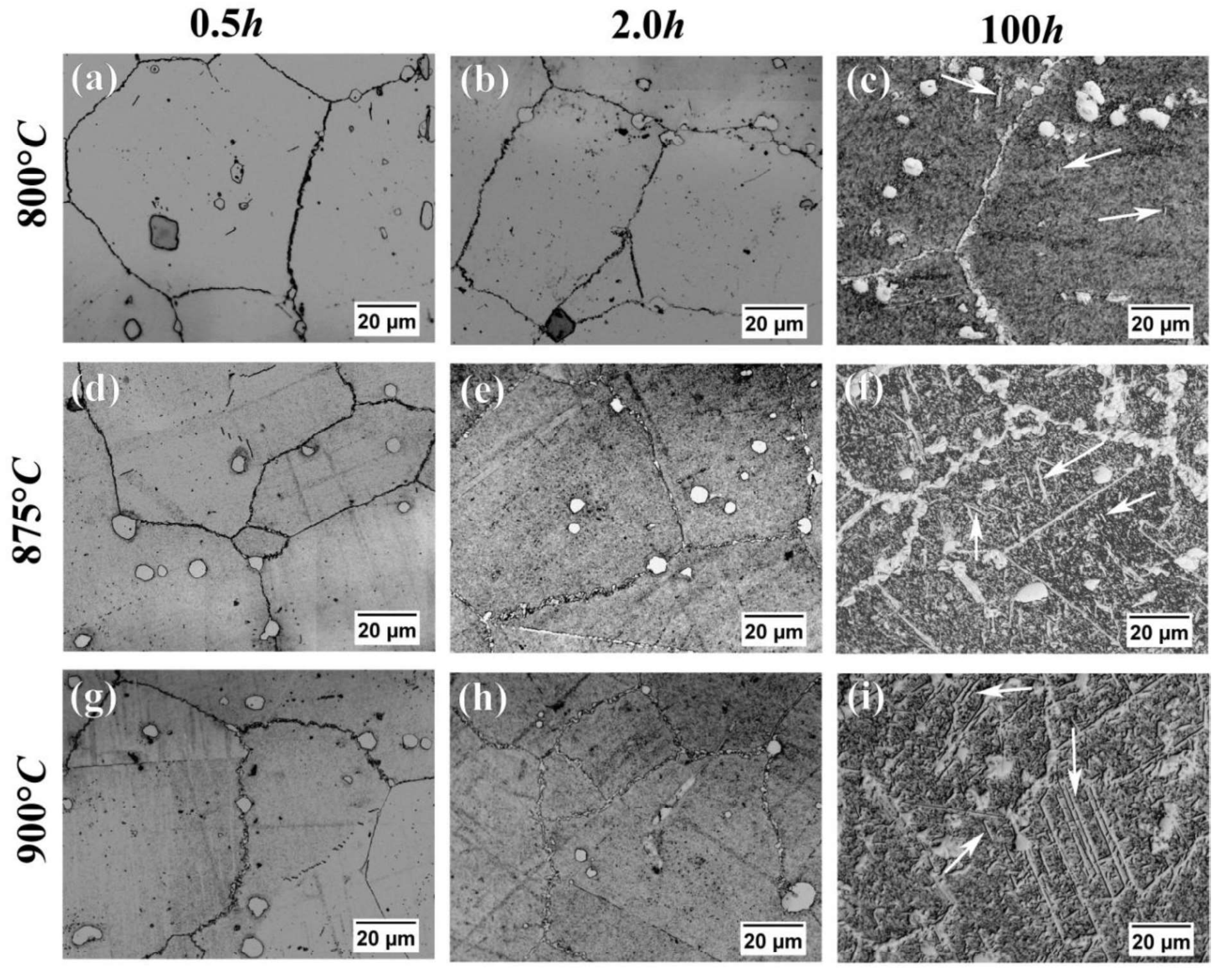

Figure 5.1. Optical micrographs showing the evolution of needle shape particles (a few of them are marked by arrows) in samples aged at 800-950°*C* for 0.5-100*h*: (a) 0.5*h* at 800°*C*; (b) 2.0*h* at 800°*C*; (c) 100*h* at 800°*C*; (d) 0.5*h* at 875°*C*; (e) 2.0*h* at 875°*C*; (f) 100*h* at 875°*C*; (g) 0.5*h* at 900°*C*; (h) 2.0*h* at 900°*C*; (i) 100*h* at 900°*C*.

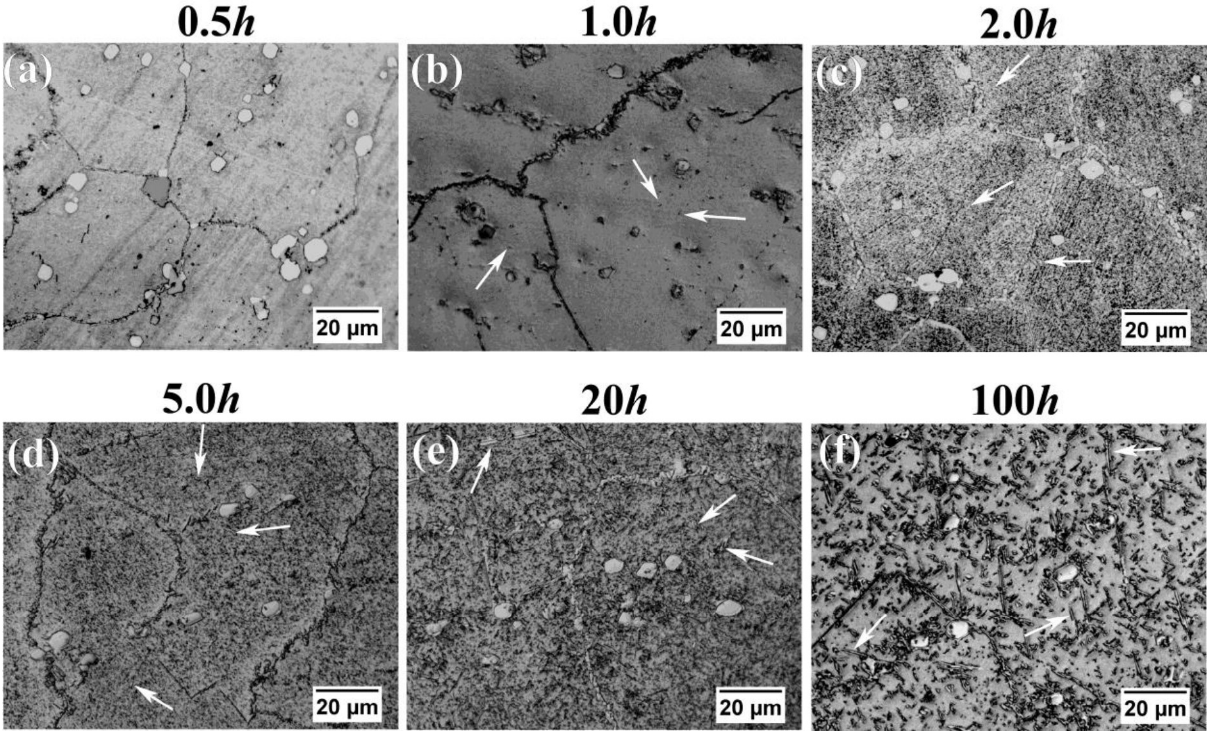

Figure 5.2. Optical micrographs showing isothermal evolution of needle shape particles (a few of them are marked by arrows) in samples aged at 950°*C*.

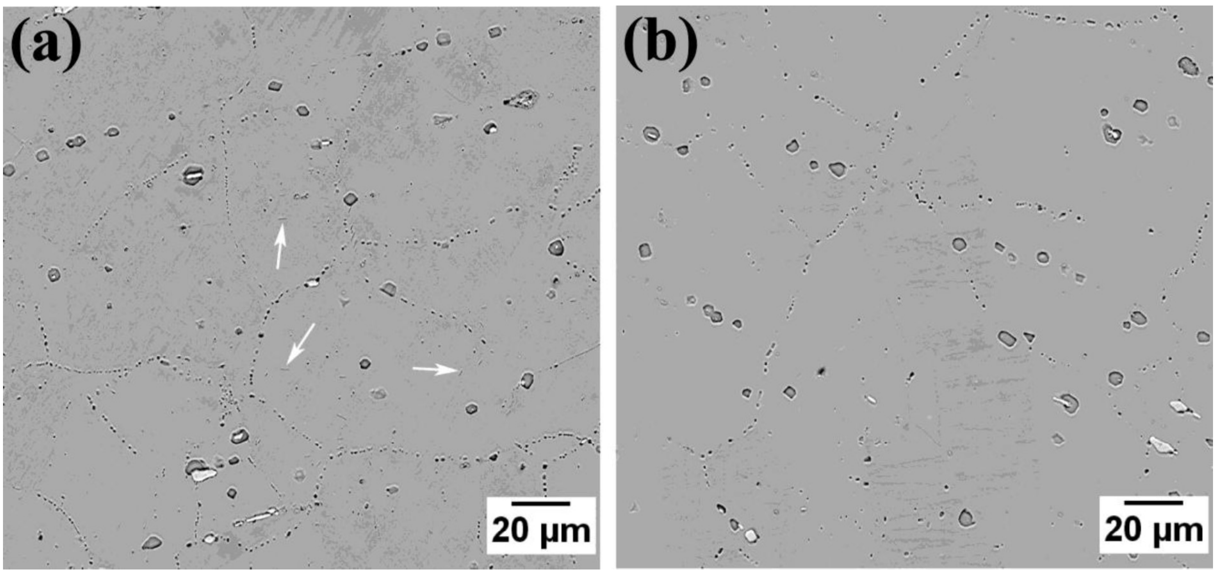

Figure 5.3. *BSE* micrographs of samples aged at: (a) 1000°*C* for 0.5*h*; (b) 1050°*C* for 0.5*h*, Needle shaped particles are visible at 1000°*C* (a few of them are marked by arrows) but are absent at 1050°*C* temperature.

Figure 5.4(a), shows *XRD* patterns of samples aged at 800-950°*C* for 100*h*, in which new peaks appeared (whose zoomed view is also shown in Figures 5.4(b-d)). Detailed investigation of these precipitated particles were also carreid out using *SEM, TEM* and *EDS* methods. Figure 5.5 shows secondary electron (*SE*) micrographs of samples aged for 0.5*h* at 800-950°*C* temperatures. These micrographs clearly revealed the presence of two different kinds of precipitates having different morphology. Particles which appeared in spherical morphology (that changed to cuboidal during later stages of annealing) were γ'-phase particles discussed in Chapter 4 [14]. Second kind of precipitates, always had a lath type morphology during early stages of evolution at all temperatures 800-950°*C* (see Figure 5.5), but later assumed a needle shape morphology. Figure 5.6 shows *SEM* micrographs depicting evolution of morphology of these particles during isothermal annealing at 950°*C*.

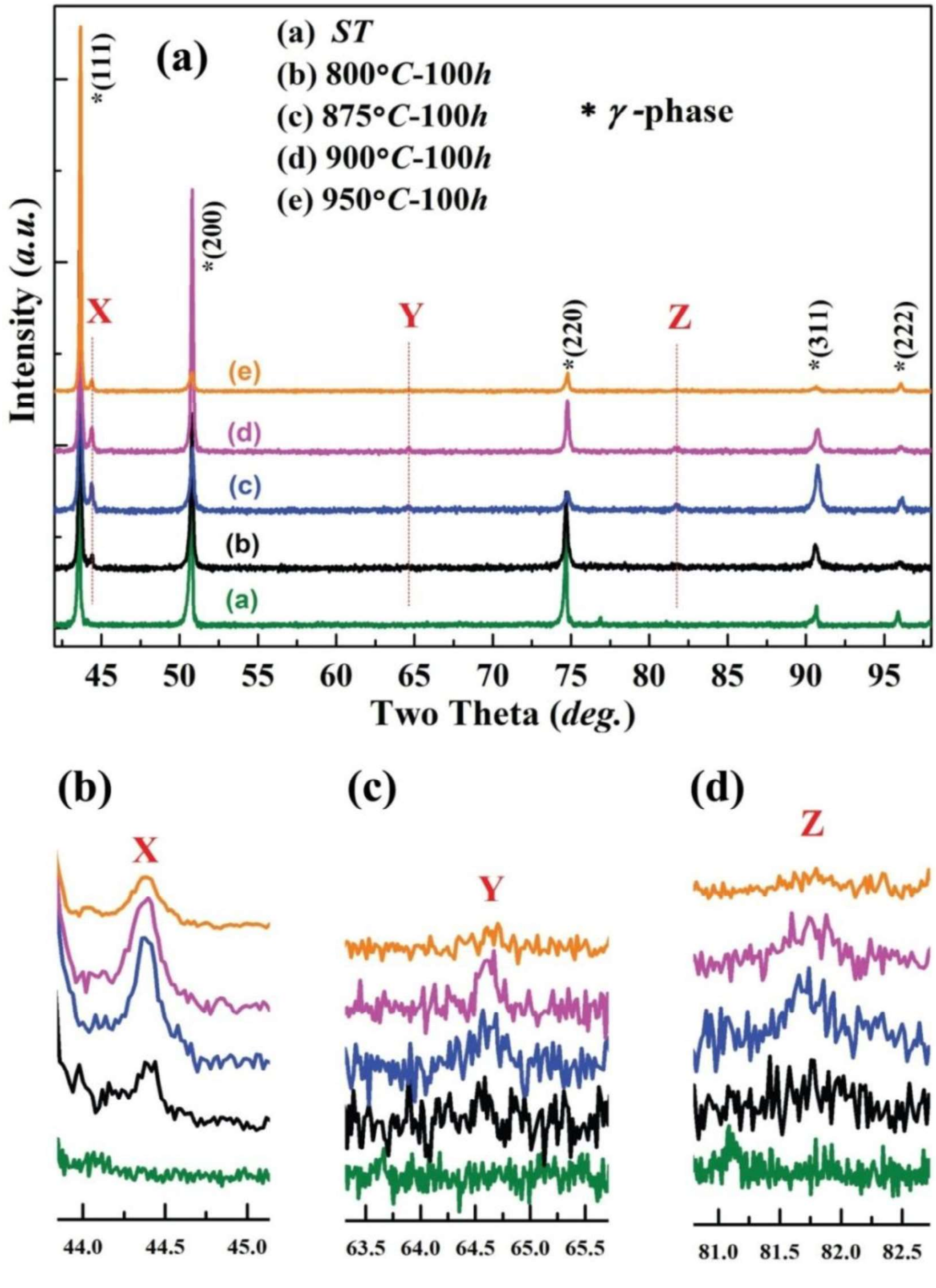

Figure 5.4. (a) *XRD* pattern of solution treated (*ST*) sample and samples aged for 100*h* at 800-950°*C,* depicting peaks corresponding to *γ*-phase as well as a few extra peaks (X, Y and Z) in aged samples (zoomed-in view shown in (b), (c) and (d), respectively), which were later identified to be of a *Cr*-rich *α*-phase.

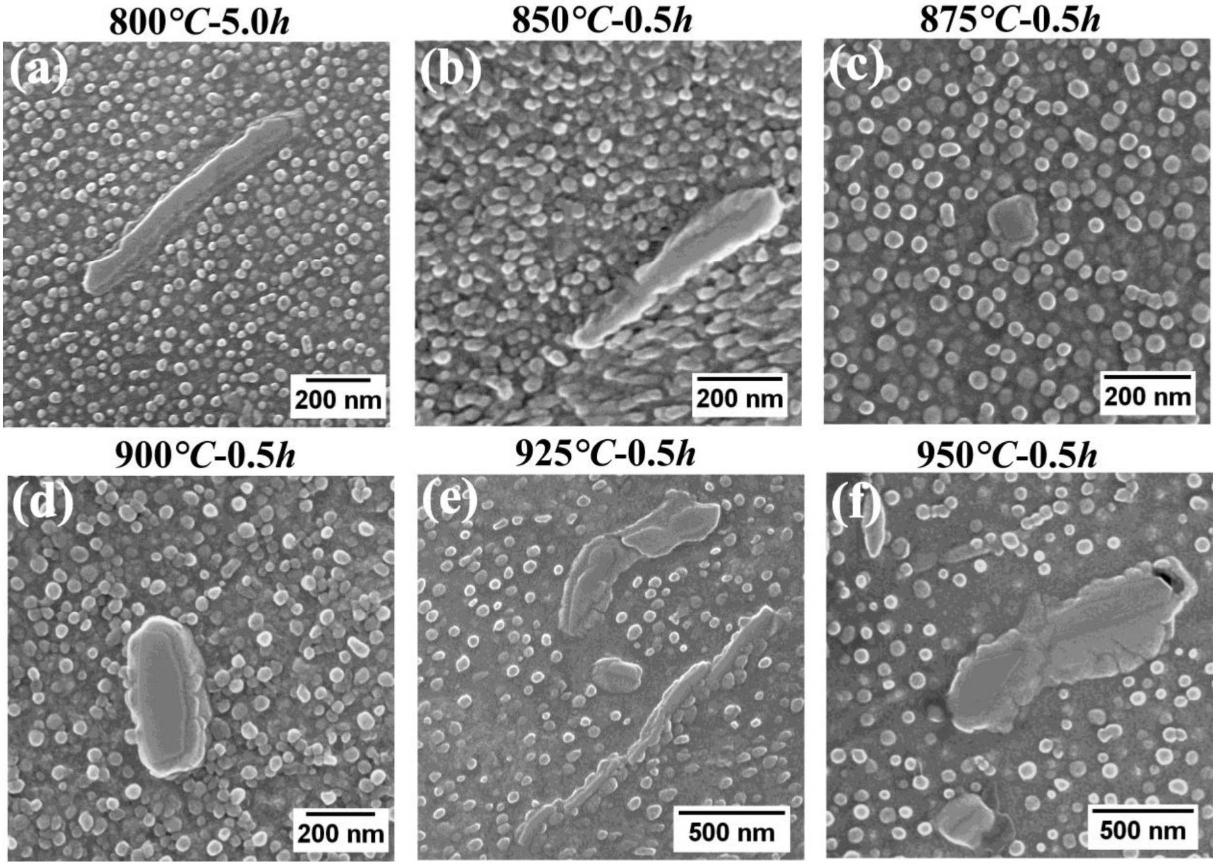

Figure 5.5. *SE* micrographs depicting the start of precipitation of needle shape particles at different ageing temperatures (800-950°*C*). It is also depicting the γ'-phase precipitates which have already discussed in Chapter 4.

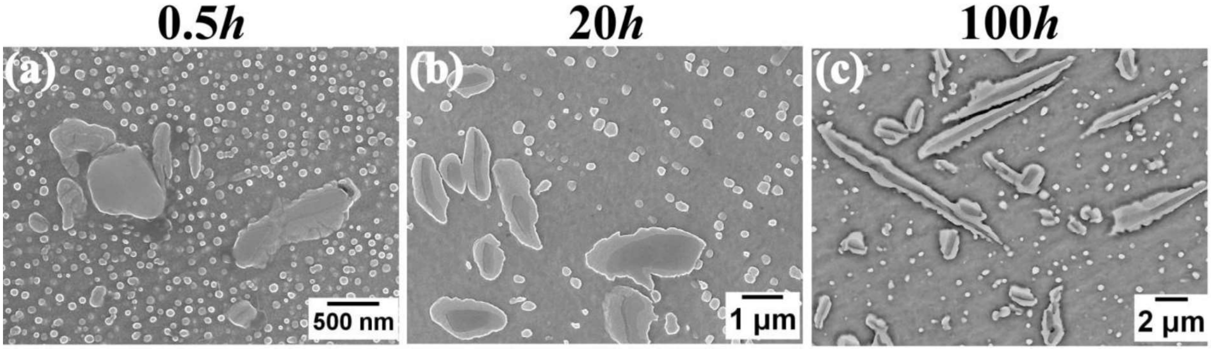

Figure 5.6. *SE* micrographs depicting the isothermal evolution of needle shape precipitates in samples aged at 950°*C*.

5.2. Phase identification and orientation relationship:

A careful analysis revealed that these particles were always comprised of two phases (Figure 5.7(a)) – an inner phase (in dark contrast) enveloped by an envelope phase (in bright contrast) – suggesting of their simultaneous appearance. Components of these particles were determined using point scan *EDS* analysis in *SEM*, which revealed that inner phase was rich in *Cr* while outer phase was enriched in *Al* *w.r.t.* the matrix composition (see *EDS*-spectra given in Figures 5.7(b-c)). Composition of these two phases along with matrix phase is given in Table 5.1. It is important to mention here that composition given in Table 5.1 could be associated with large errors because of the relatively small size of particles compared with large interaction volume of *EDS* in *SEM* and is of only qualitative importance. A line scan analysis (Figure 5.7(d)) across a needle also qualitatively supported the enrichment of *Cr* and *Al* in inner and outer regions, respectively.

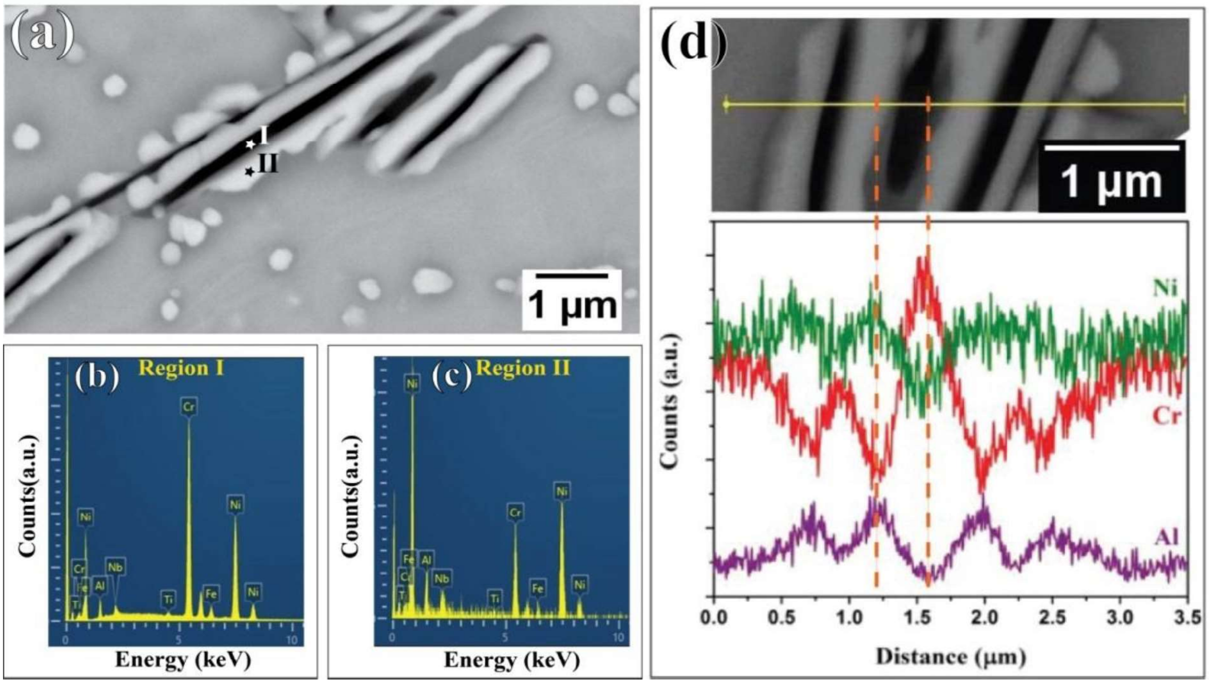

Figure 5.7. (a) *SE* micrographs depicting needle shape particles composed of two phases in bright and dark contrast; (b) and (c) are the *EDS* spectra from region I and II marked in Figure (a), respectively; (d) line scan across both the phases.

Table 5.1. Composition (*at.%*) of matrix and needle shaped particles (dark and bright regions) shown in Figure 5.7(a).

Elements	Matrix (*at.%*)	Dark region (*at.%*)	Bright region (*at.%*)
Ni	57.76	45.38	58.96
Cr	30.32	44.58	20.92
Fe	4.74	3.32	3.72
Al	6.16	5.02	13.08
Nb	0.76	1.20	2.82
Ti	0.26	0.50	0.50

Composition of these particles was identified on the basis of chemical analysis of electrolytically extracted particles from the matrix. Figures 5.8(b-c) show *SE* image of extracted needles along with an *EDS* spectrum from one such needle. *EDS* analysis of extracted needles showed them to be *Cr*-rich (*Cr*-95.0, *Ni*-3.10 and *Fe*-1.90; in *at.*%). Further, *XRD* analysis of extracted particles revealed them to be a *Cr*-rich α-phase with a body centred cubic (*bcc*) structure having a lattice parameter a~2.8802 $\AA$ [117] (Figure 5.8(a)). In addition, peaks corresponding to $(Ti,Nb)C$- and $Cr_{23}C_6$-carbides were also observed in *XRD* pattern, whose presence is normal as they form during solidification and subsequent heat treatments of *Ni*-base superalloys, see for example [121]. Thus *Cr*-rich inner phase particles shown in Figures 5.7(d) and 5.8(b) are *bcc* *Cr*-rich particles and henceforth will be designated as α-phase particles.

Detailed analysis of the *Al*-rich enveloped phase, designated as e_p-phase (region II in Figure 5.7(a)) was carried out using *TEM* analysis. Figure 5.9 shows a bright field (*BF*) *TEM* micrograph of a sample aged at 950°*C* for 100*h*. The figure showed a region of a grain containing (γ+γ')-phases within which α-particles surrounded by the e_p-phase had formed. As shown earlier [14], maximum volume fraction of the γ'-phase had precipitated out within $0.5h$ at this temperature.

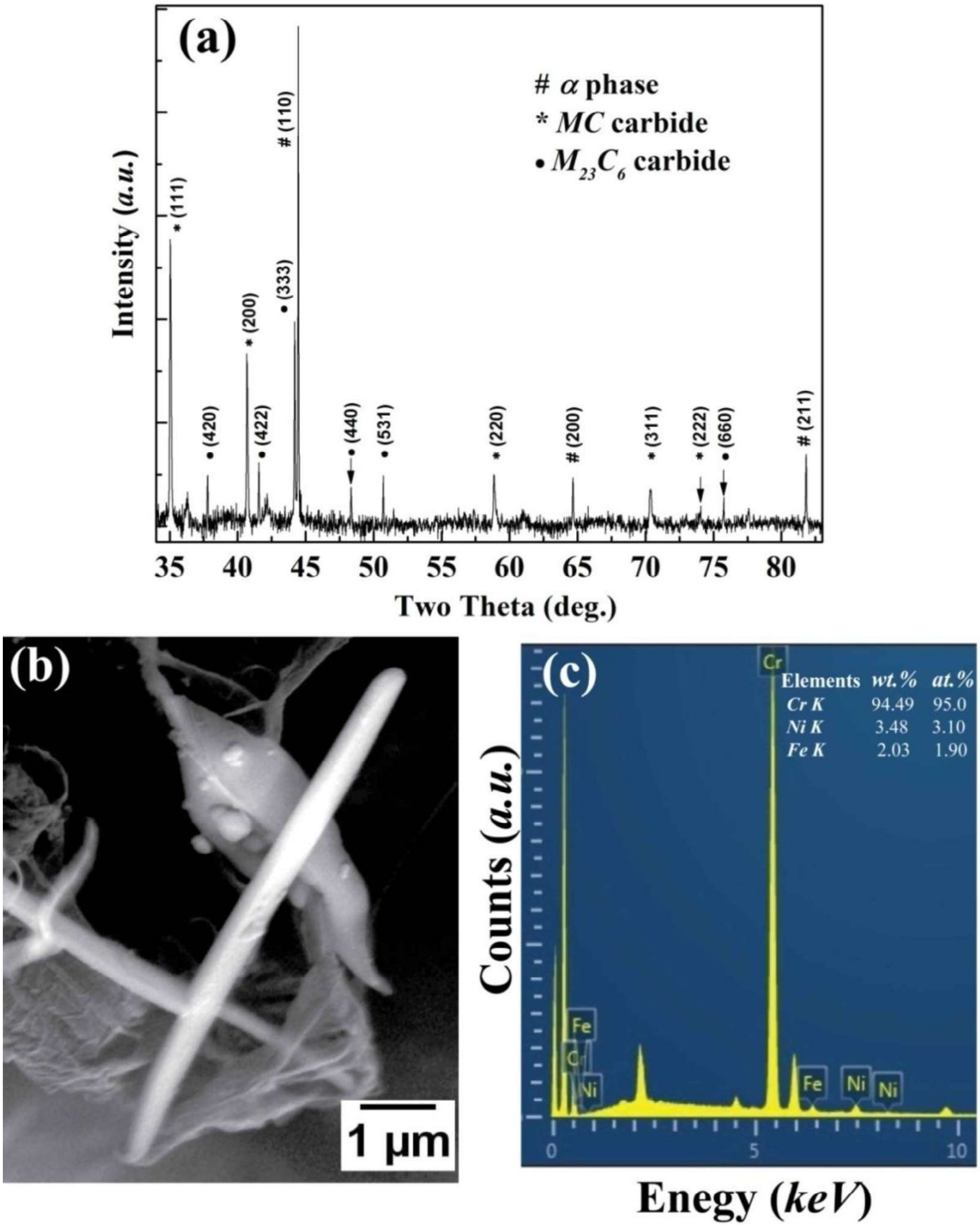

Figure 5.8. (a) *XRD* scan of extracted particles; (b) *SE* micrographs showing the needle shape particles; (c) *EDS* spectra from particle shown in Figure (b).

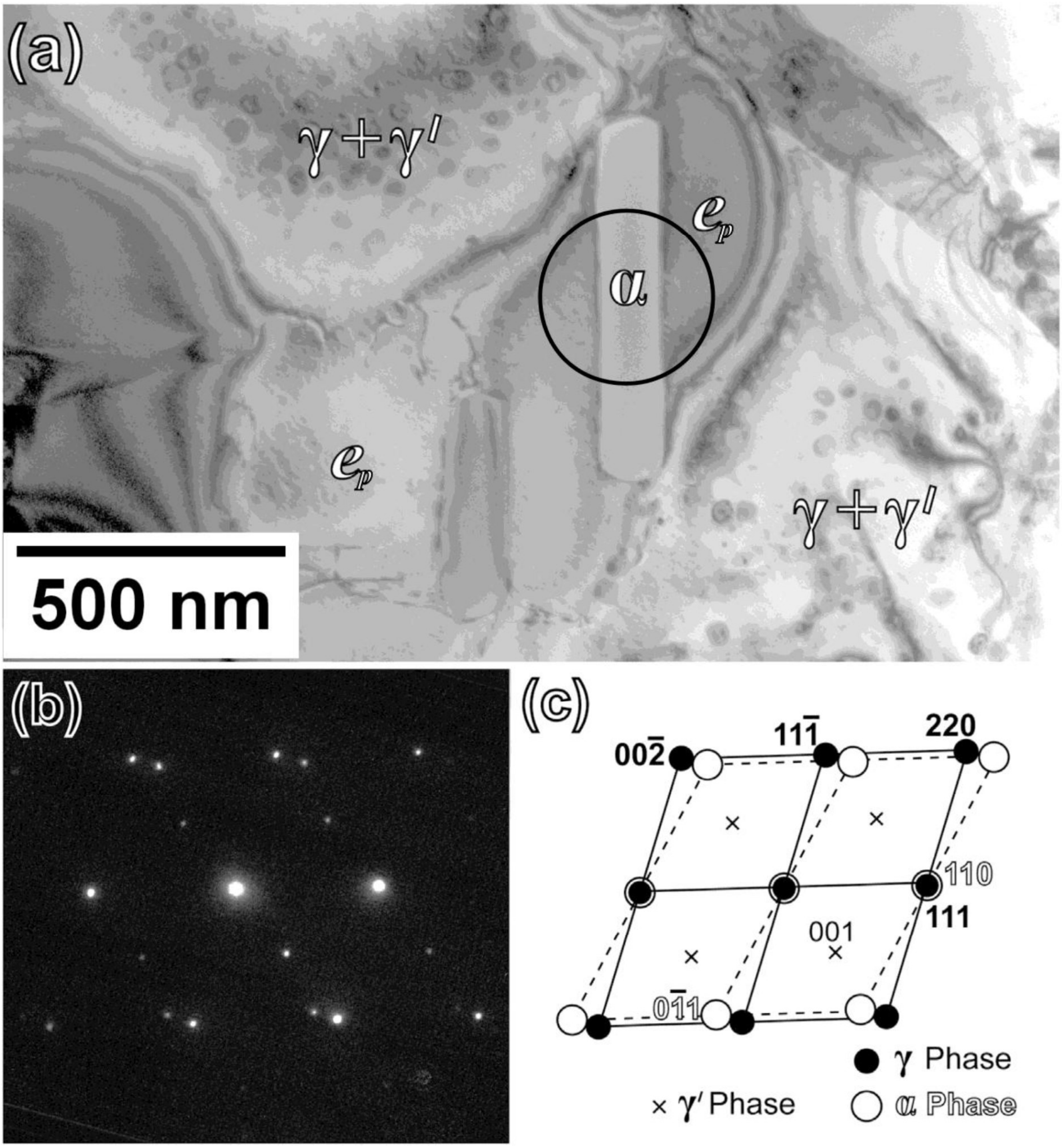

Figure 5.9. (a) *BF TEM* micrograph of sample aged at 950°*C* for 100*h*. Different phases, namely α-, e_p-, γ- and γ'- are marked in Figure; (b) selected area electron diffraction (*SAED*) pattern from the region marked in Figure (a), containing α- and e_p-phases. This diffraction pattern could indexed as superimposed diffraction pattern corresponding to $[\bar{1}10]_{\gamma}//[\bar{1}11]_{\alpha}$ zone axes of γ- and α-phases; (c) key to *SAED* pattern in (b). Superlattice reflections of the γ'-phase at {100} and equivalent positions of the γ-phase, could also be noticed.

Table 5.2. Compositions of α- and e_p-phases corresponding to regions shown in Figure 5.9(a). Composition of the γ_s-phase was determined from the matrix region in between γ'-particles in the $(\gamma + \gamma')$-region. Composition of the γ'-phase corresponds to that of particles coarsened at 950°*C* reported earlier in Chapter 4 [14].

Phases	**Elemental composition (in *at.%*)**					
	Ni	***Cr***	***Fe***	***Al***	***Ti***	***Nb***
$\boldsymbol{\alpha}$	3.28	95.18	1.54	-	-	-
$e_p\ (\gamma_d + \gamma'_d)$	71.85	5.32	1.26	15.54	1.78	4.26
γ_s	57.76	30.32	4.74	6.16	0.26	0.76
γ'	68.77	5.04	1.54	18.49	1.82	4.34

It was, therefore, reasonable to assume that the γ-phase regions in between γ'-particles had saturated with respect to γ'-forming solutes at this temperature. Composition of the saturated γ-phase (designated as γ_s) measured by *EDS* analysis is given in Table 5.2. Figure 5.9(b) shows a composite *SAED* pattern taken from α- and e_p-phases from the marked region in Figure 5.9(a) when their interface was parallel to the electron beam. The observed diffraction patterns could be indexed to $[\bar{1}10]_\gamma$ and $[\bar{1}11]_\alpha$ zone axes of the two phases, which appeared to be nearly parallel (a key to Figure 5.9(b) is shown in Figure 5.9(c)). In addition, superlattice reflections of γ'-phase, at {100} and equivalent positions of γ-phase, could be noticed. However, γ'-phase particles could not be imaged by dark field (*DF*) microscopy suggesting that their size was smaller than the diffraction contrast resolution limit of the *JEOL* 2000*FX* microscope used for their imaging. Nonetheless, the mottled contrast observed within the enveloped region in the *BF* image (Figure 5.9(a)) was consistent with the presence of fine particles in it. Thus e_p-phase contained a mixture of γ_d- and γ'_d -phases (subscript '*d*' is used to represent that chemical compositions of the γ_d- and γ'_d-phases were different from those of otherwise mentioned γ- and γ'-phases due to the formation of former in Cr depleted regions). Composition of α-particles analysed by *TEM* was in agreement with that measured in extracted particles (Figure 5.8(c)), while composition of the e_p-phase (which was an average of compositions of γ_d- and γ'_d-phases) was found to be close to that of the γ'-phase (Table 5.2). Crystal structure and chemical composition together, therefore, established that the e_p-phase was nothing but γ_d- and γ'_d-phases formed in a locally altered (γ + γ')-phase field due to Cr rejection during the formation of α-particles. High resolution transmission electron microscope (*HRTEM*) image of regions across α/e interface exhibited fringes corresponding to $(111)_\gamma$ planes parallel to those of $(110)_\alpha$ planes when imaged along $[\bar{1}10]_\gamma//[\bar{1}11]_\alpha$ direction (Figure 5.10(a)). This was also confirmed by diffraction patterns generated by Fast Fourier Transformation (*FFT*) which exhibited overlapped reflections due to $(111)_\gamma$ and $(110)_\alpha$ planes of the two phases (Figures 5.10(b) and 5.10(c)).

5.3. Discussion:

On the basis of results presented here, it could be concluded that the Alloy 693 studied here, starting from the supersaturated (*SS*) solid solution state, followed a phase transformation sequence given below:

$$\gamma_{ss1} \xrightarrow{ST} \gamma_{ss2} + \gamma' \xrightarrow[950°C]{\text{Ageing}} (\gamma_s + \gamma') + (\gamma_d + \gamma'_d) + \alpha \quad \text{...(i)}$$

γ_{ss1} -represents the super saturated solid solution state of the disordered alloy. During water quenching (*WQ*), after a solid solution treatment at 1100°C, it instantly precipitated out fine particles of γ'-phase at temperatures below 950°C [13]. γ_{ss2} -represents super saturated solid solution state of the alloy after partial precipitation of the γ'-phase during *WQ*. Obviously, the γ_{ss2}-state would be less supersaturated mainly with Al with respect to the γ_{ss1}-state. As mentioned earlier, growth and coarsening of γ'-phase particles during ageing at 950°C saturated the γ-phase matrix in between them with respect to γ'-forming solutes, referred as γ_s-phase. The γ_s-phase, however, was unstable with respect to chromium concentration, which was rejected to form α-phase. Depletion of chromium in the vicinity of α-phase particles altered composition of the enveloped region significantly.

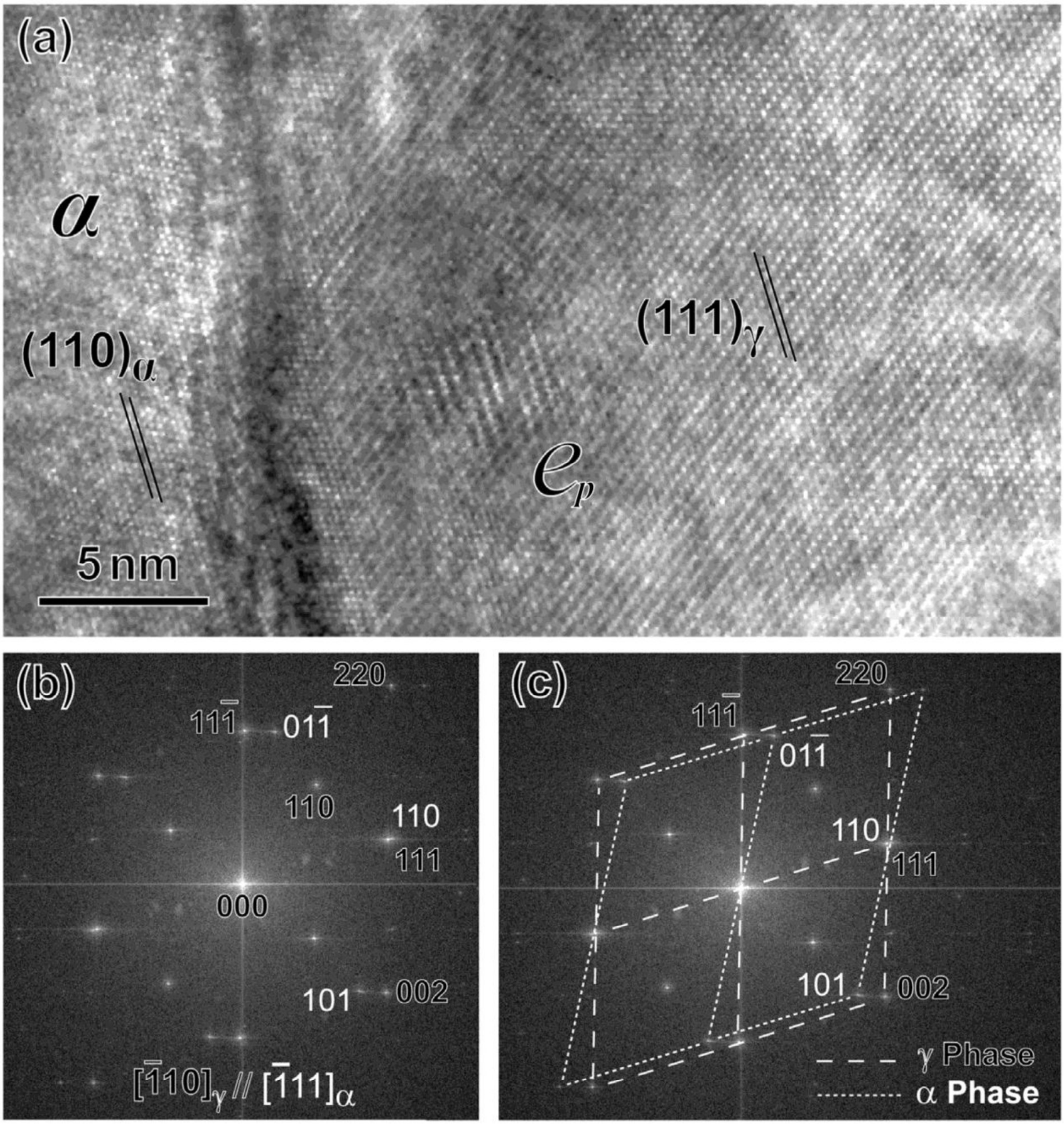

Figure 5.10. (a) *HRTEM* micrograph of α/e_p interface region in sample aged at 950°*C* for 100*h;* (b) *FFT* pattern from corresponding region, showing superimposed reflections from $\{110\}_\alpha$ and $\{111\}_\gamma$ planes. For the sake of clarity, orientation of reflections is marked by lines in (c).

Following sections discuss thermodynamic stability of various phases involved in this transformation sequence, orientation relationship of the α-phase with the matrix and mechanism of the formation of α-phase particles.

5.3.1. Stability of phases at elevated temperatures:

Three major elements, *Ni*, *Cr* and *Al*, together make about 94.3*at.%* of the alloy composition. *Ni-Al-Cr* ternary phase diagram, therefore, makes a useful basis for understanding thermodynamic stability of γ-, γ'- and α-phases observed in this work.

Figure 5.11 shows isothermal sections of *Ni-Cr-Al* ternary phase diagrams at 850°*C,* 1000°*C* and 1100°*C* temperatures*,* showing the effect of temperature and *Al*- addition on phase fields of binary *Ni-Cr* alloy system [5, 7, 24]. From Figure 5.11, it could be observed that *Cr* solubility in the γ-phase decreases from about 48a*t.%* (at 1100°*C*) to about 39*at.%* (at 850°*C*). Addition of *Al* in binary *Ni-Cr* alloys further decreases the solubility of *Cr* at these temperatures, like at 1000°*C* addition of 5.0*at.% Al* reduces the *Cr* solubility from 44.5*at.%* to 37.5*at.%.*

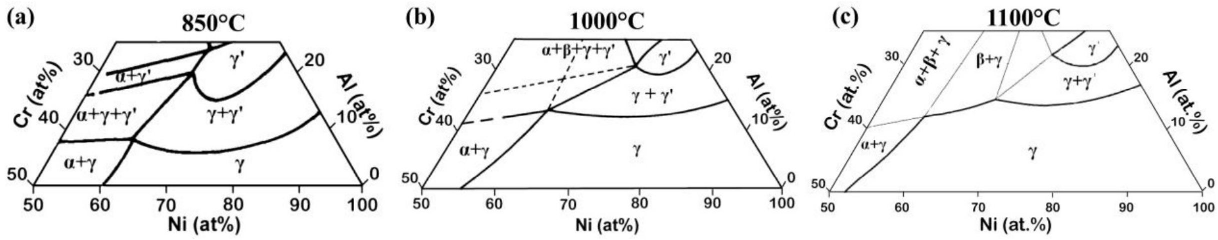

Figure 5.11. Isothermal sections of *Ni-Cr-Al* ternary phase diagrams taken at: (a) 850°*C*; (b) 1000°*C* and (c) 1100°*C,* showing the effect of temperature on phase fields [5-7].

Figure 5.12 shows superimposed parts of isothermal sections of the ternary *Ni-Cr-Al* phase diagram taken at 1000°*C* and 850°*C* [5, 24]. An isothermal section at 950°*C* (shown by broken lines in Figure 5.12) was drawn on the basis of linear interpolation of phase boundaries at two temperatures. Composition of the γ_s-phase determined after 100*h* of ageing at 950°C (after the precipitation of γ'-phase) was found to be Ni-57.76, Cr-30.32, Fe-4.74, Al-6.16, Ti-0.26, Nb-0.76 (in $at.\%$) (Table 5.2). Restricting compositions to Ni, Cr, and Al elements, equivalent compositions of γ-phases in fully disordered state (*i.e.,* γ_{ss1}) and after precipitation of γ'-phase (*i.e.,* of γ_s-phase), as per relation (i), would lay at points marked as orange and green dots, respectively, in Figure 5.12.

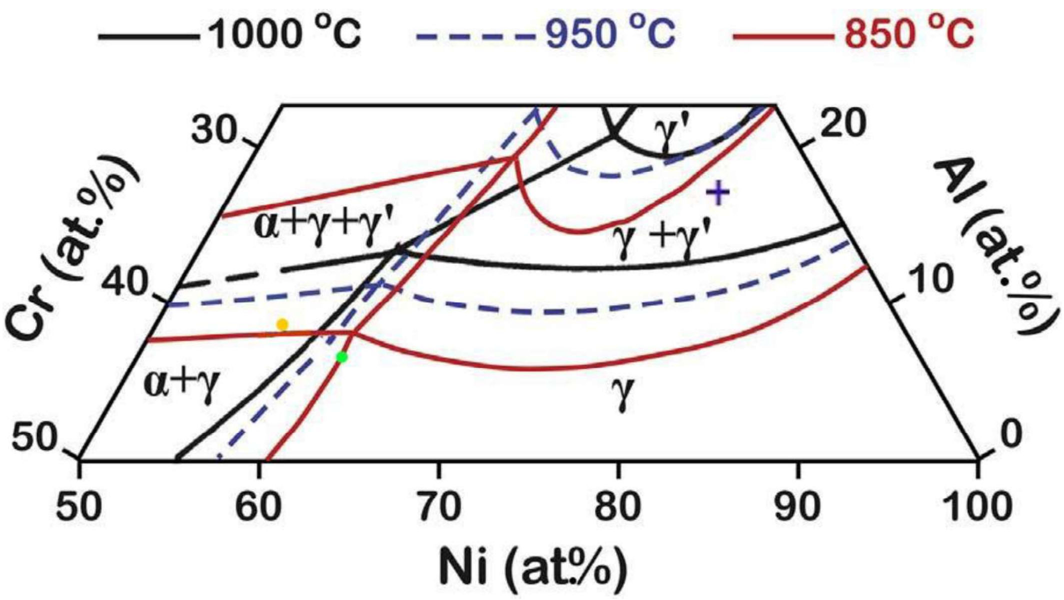

Figure 5.12. Superimposed parts of isothermal sections of Ni-Cr-Al ternary phase diagrams taken at 1000°C and 850°C (solid lines) [5, 6]. Phase fields at 950°C (in broken lines) were drawn on the basis of their linear interpolation. Equivalent compositions of the γ-phases in fully disordered state (*i.e.*, γ_{ss1}), and after the precipitation of γ'-phase (*i.e.*, of γ_s-phase), as per nomenclature given in relation (i), are marked as orange (●) and green (●) dots, respectively. Equivalent composition in the enveloped region is marked by a '+' mark (see text for details).

Composition of the γ_s-phase lay close to the $\gamma/(\alpha+\gamma)$ phase boundary at 950°C. Further, according to ternary phase diagrams of Ni-Cr-Nb, Ni-Cr-Fe and Ni-Cr-Ti alloys [8, 122, 123], addition of Nb, Fe and Ti in binary Ni-Cr alloys reduces the solubility of Cr in the γ-phase (see Figure 5.13). Likewise, their additions in Ni-Al alloy reduce solubility of Al in the γ-phase and promotes the formation of γ'-phase [62, 63] (see Figure 5.14). From this, it could be concluded that presence of 4.74, 0.76 and 0.26 *at.%* of *Fe, Nb* and *Ti* elements (γ_s-phase), respectively, in the *Ni-Cr-Al* phase diagram would shift its phase boundaries to stabilize composition of the γ_s-phase in the ($\alpha+\gamma+\gamma'$)-phase field at 950°*C* (Figure 5.12) by shifting the ($\alpha+\gamma$)/($\alpha+\gamma+\gamma'$) boundary towards lower *Al* side and the ($\alpha+\gamma+\gamma'$)/($\gamma+\gamma'$) phase boundary towards higher *Ni* (lower *Cr*) side.

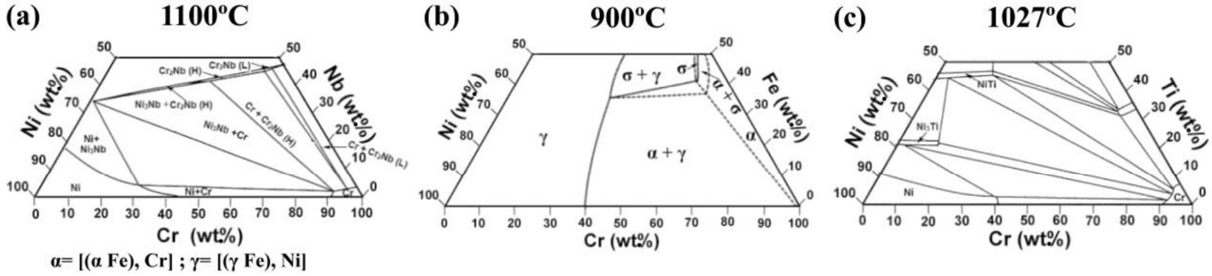

Figure 5.13. Isothermal sections of ternary phase diagrams : (a) *Ni-Cr-Nb* at 1100°*C* [122]; (b) *Ni-Cr-Fe* at 900°*C* [123]; and (c) *Ni-Cr-Ti* at 1027°*C* [8], showing the effect of ternary addition on *Ni-Cr* phase fields.

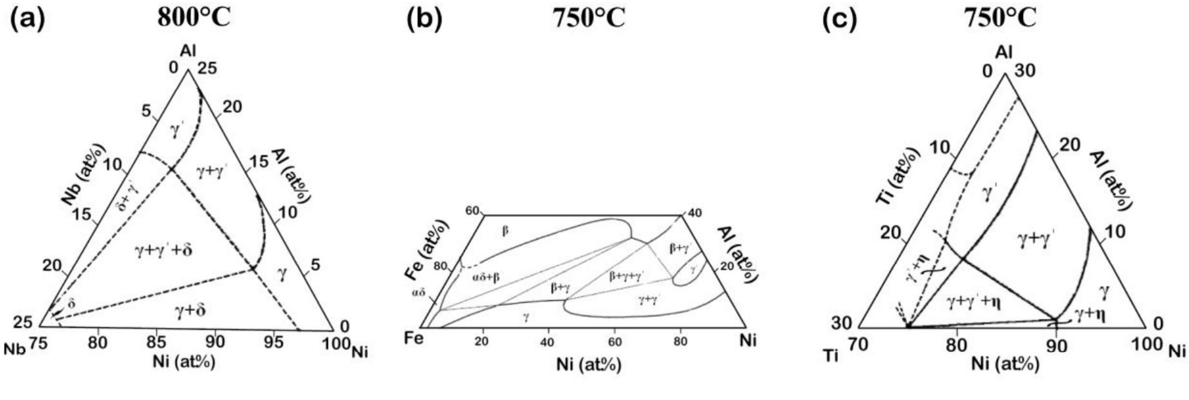

Figure 5.14. Isothermal section of ternary phase diagrams: (a) *Ni-Al-Nb* at 800°*C* [62]; (b) *Ni-Al-Fe* at 750°*C* [63]; and (c) *Ni-Al-Ti* at 750°*C* [62], showing the effect of ternary addition on *Ni-Al* phase fields.

Composition of the γ_s-phase after the precipitation of γ'-phase at 950°*C* would, therefore, be supersaturated with *Cr*, which would precipitate out as α-phase particles. Rejection of *Cr* during the formation of α-phase would alter composition of the enveloped region (Table 5.2).

Altered composition of e_p-phase field, restricted to *Ni, Cr, Al* elements, would be about 17*at.% Al* and 6*at.%* of *Cr* (marked as "+" in the *Ni-Cr-Al* phase diagram, Figure 5.12), which lay within the ($\gamma + \gamma'$)-phase field. The fact that γ'_d-phase particles in the envelope region could not be resolved indicated of their fine sizes. Fine sizes of γ'_d-phase particles suggested of limited driving force available for their formation, which is a function of supersaturation (ΔC) and under cooling (ΔT^*) below the solvus temperature (T_e) [16]. Due to the wide range of ($\gamma + \gamma'$)-phase field, precipitation of the γ'-phase having a composition, for instance, near to $\gamma'/(\gamma + \gamma')$ phase boundary towards less *Al* and *Cr* side (Figure 5.12) would be associated with limited driving force.

As seen in Figures 5.2 and 5.3 that volume fraction of α-particles reaches to a maximum value then started to dissolve into the matrix with increasing temperature and at 1050°*C* they completely dissolved into the matrix. The tendency of the alloy to dissolve α-phase at temperatures higher than 950°*C* could be rationalised on the basis of phase fields in which alloy composition would move to single phase field at higher temperatures. It was clear from Figure 5.11 that with increasing temperature solubility of *Cr* increased and γ-phase field expended significantly thereby makes the composition of the matrix (γ_{ss2}) to appear in single phase field region.

5.3.2. Orientation relationship of α-phase with matrix:

Crystallographic orientation relationship (*OR*) between two phases having different crystal structures depends upon their relative lattice parameters and plays an important role in determining microstructure as well as mechanical properties. It is typically expressed by a set of planes that are parallel in the two lattices and a set of directions which lies within them and are parallel. A number of alloys undergo $\gamma \rightarrow \alpha$ transformations in steels, *Cu–Zn* brasses, *Cu–Cr* alloys, *etc.* [124-139]. *OR* between two phases in these alloys vary within a well defined range but close-packed $\{111\}_\gamma$ planes are usually found to be approximately parallel to $\{011\}_{\alpha}$ planes. Variations in the *ORs* are a consequence of difference in directions that comes in order to meet the condition of undistorted and unrotated habit plane. Table 5.3 list different *ORs* reported for $\gamma \rightarrow \alpha$ transformations [124, 140-144].

Table 5.3. Summary of commonly observed *fcc-bcc ORs* [124, 140-144].

Name	**Orientation Relationship**		**References**
	Planes	**Directions**	
Bain	$(010)_{fcc} \parallel (010)_{bcc}$	$[001]_{fcc} \parallel [101]_{bcc}$, $[100]_{fcc} \parallel [10\bar{1}]_{bcc}$, $[101]_{fcc} \parallel [100]_{bcc}$, $[\bar{1}01]_{fcc} \parallel [001]_{bcc}$	[140]
K-S	$(111)_{fcc} \parallel (110)_{bcc}$	$[\bar{1}10]_{fcc} \parallel [\bar{1}11]_{bcc}$, $[11\bar{2}]_{fcc} \parallel [\bar{1}1\bar{2}]_{bcc}$	[124]
N-W	$(111)_{fcc} \parallel (110)_{bcc}$	$[\bar{1}01]_{fcc} \parallel [001]_{bcc}$, $[\bar{1}2\bar{1}]_{fcc} \parallel [\bar{1}10]_{bcc}$	[141, 142]
G-T	$(111)_{fcc}$ ~ 1° from $(110)_{bcc}$	$<112>_{fcc}$ ~ 2° from $[1\bar{1}0]_{bcc}$	[143]
Pitsch	$(001)_{fcc} \parallel (101)_{bcc}$	$[\bar{1}10]_{fcc} \parallel [\bar{1}11]_{bcc}$, $[110]_{fcc} \parallel [12\bar{1}]_{bcc}$	[144]

Among the *ORs* listed in Table 5.3, Kurdjumov-Sachs (*KS*) and Nishiyama-Wasserman (*NW*) *ORs* are the most frequently reported relationships. The two relationships bear a close resemblance. In both the *ORs*, a $\{111\}_{\gamma}$ plane of the γ-phase is parallel to a $\{110\}_{\alpha}$ plane of the α-phase, and the only difference between the two is a rotation of one by 5.26° around its normal with respect to that of the other.

Figure 5.15 shows stereographic projections of two lattices depicting relationship between α- and γ-phases in *NW*- and *KS*-orientations. Open and solid circles represent *bcc* and *fcc* poles while rectangle and hexagon depict relative orientations of atomic arrangements on respective close packed planes. In the *NW*-orientation, close packed directions of the two phases (*i.e.*, $<110>_{\gamma}$ and $<111>_{\alpha}$) are misaligned by an angle of 5.26°. However, a rotation of 5.26° around the plane normal of $\{111\}_{\gamma}$ plane changes *NW-OR* to a *KS*-relationship where a

$\langle 110\rangle_\gamma$ direction comes into coincidence with a $\langle 111\rangle_\alpha$ direction while the other set of similar directions gets misaligned by 10.52°. In Figure 5.15, an anti-clock rotation of the $(111)_\gamma$ plane normal in *NW*-orientation coincided $[\bar{1}10]_\gamma$ and $[\bar{1}11]_\alpha$ directions of the two phases, and created the *KS-OR* . Likewise, a clockwise rotation would create another variant of the *KS-OR*. This makes *NW*-relation exactly midway between two variants of *KS*-relation for a given set of parallel close-packed planes. This close proximity sometimes makes it difficult to determine *OR* on the basis of diffraction patterns because Bragg's relaxation allows their appearance even when crystal orientation is a few degrees away from an exact zone axis.

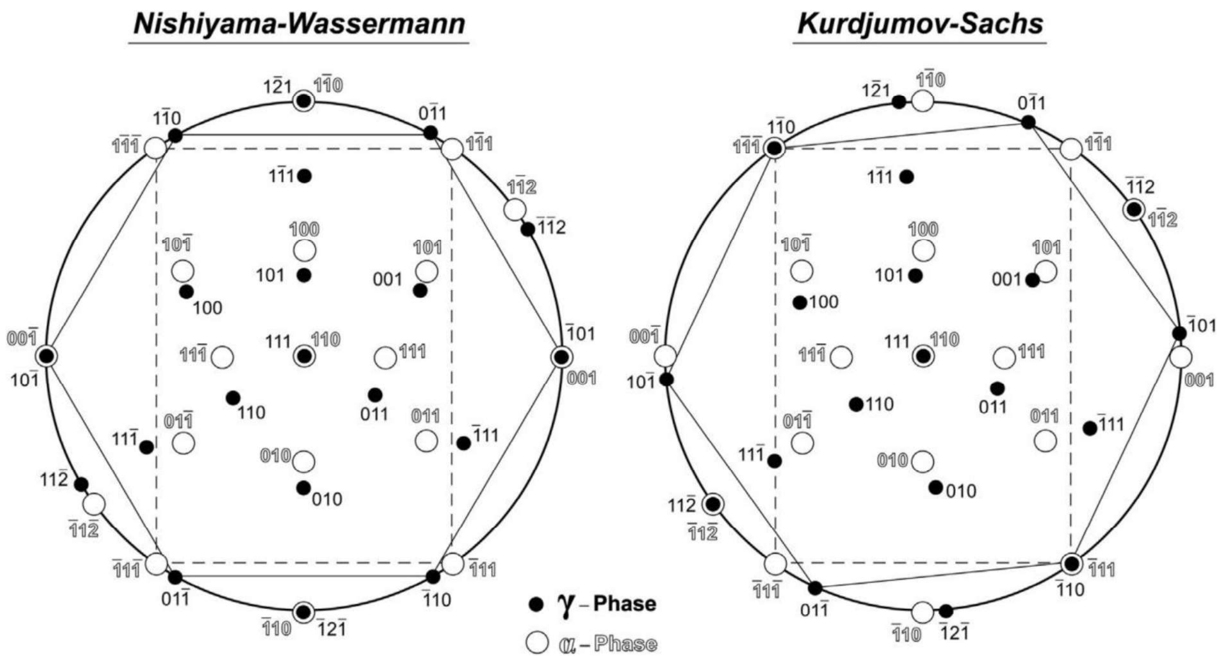

Figure 5.15. Composite stereograms of γ- and α-phases showing relative orientation of crystals when the two phases are oriented according to: (a) Nishiyama-Wassermann (*NW*) orientation; (b) Kurdjumov-Sachs (*KS*) orientation, for $(110)_\alpha$ and $(111)_\gamma$ close packed planes. Open and solid circles represent the *bcc* and *fcc* poles, respectively, while rectangle and hexagon depict relative orientation of atomic arrangements on respective close packed planes. Note that an anti-clock direction rotation of $(111)_\gamma$ plane normal by 5.26º in *NW*-orientation has brought to $[\bar{1}10]_\gamma$ in coincidence with $[\bar{1}11]_\alpha$ [139].

In the present case, Figure 5.9(b) unambiguously established a *KS*-type relationship between two phases as one set of close packed directions of two phases overlapped while the other set made an angle of about 10° between the two. The presence of this *OR* further was confirmed on the basis of *HRTEM* analysis of interface region whose *FFT* (Figure 5.10(b)) was consistent with diffraction pattern shown in Figure 5.9(b). This analysis concluded that the two phases followed the *KS-OR*.

5.3.3. Mechanism of the formation of α-phase:

The simplest way to view phase transformation in the present case is by the operation of two consecutive shears (see Figure 5.16), a mechanism originally proposed by Kurdjumov and Sachs (*KS*) [124]. The first shear of $a/_{12}$ magnitude along $[\bar{1}2\bar{1}]_{\gamma}$ direction on successive $(\bar{1}\,\bar{1}\,\bar{1})_{\gamma}$ planes, followed by a second shear of magnitude $a/_{10}$ along $[\bar{1}10]_{\gamma}$ direction on planes of the γ-phase having $3/_{2}$ $(\bar{1}\ \bar{1}\ 2)_{\gamma}$ spacing. The second shear changes the 60° angle to 70°32′ at the base of the transformed structure. This mechanism only orients the $[01\bar{1}]_{\gamma}$ direction parallel to the $[\bar{1}1\bar{1}]_{\alpha}$. A small contraction along $[\bar{1}11]_{\alpha}$ and a small expansion along $[\bar{1}1\bar{1}]_{\alpha}$ would however be required to create correct cell dimension for an undistorted habit plane. Relationship between transformation strain to that associated with the *KS*-mechanism was demonstrated by Weatherly et *al.* [135] in their analysis of coherent precipitates in *Cu-Cr*. They have shown that strain field associated with the formation of needles can be approximated to that of a dipole having effective Burgers vector equal to the addition of equal numbers of two types of partial dislocations involved in the *KS*-mechanism. Though Weatherly et *al.* [135] did not associate a mechanistic significance to this transformation, Dahmen et *al.* [138] have shown the accommodation of homogeneous shears by dislocations in semi coherent needles.

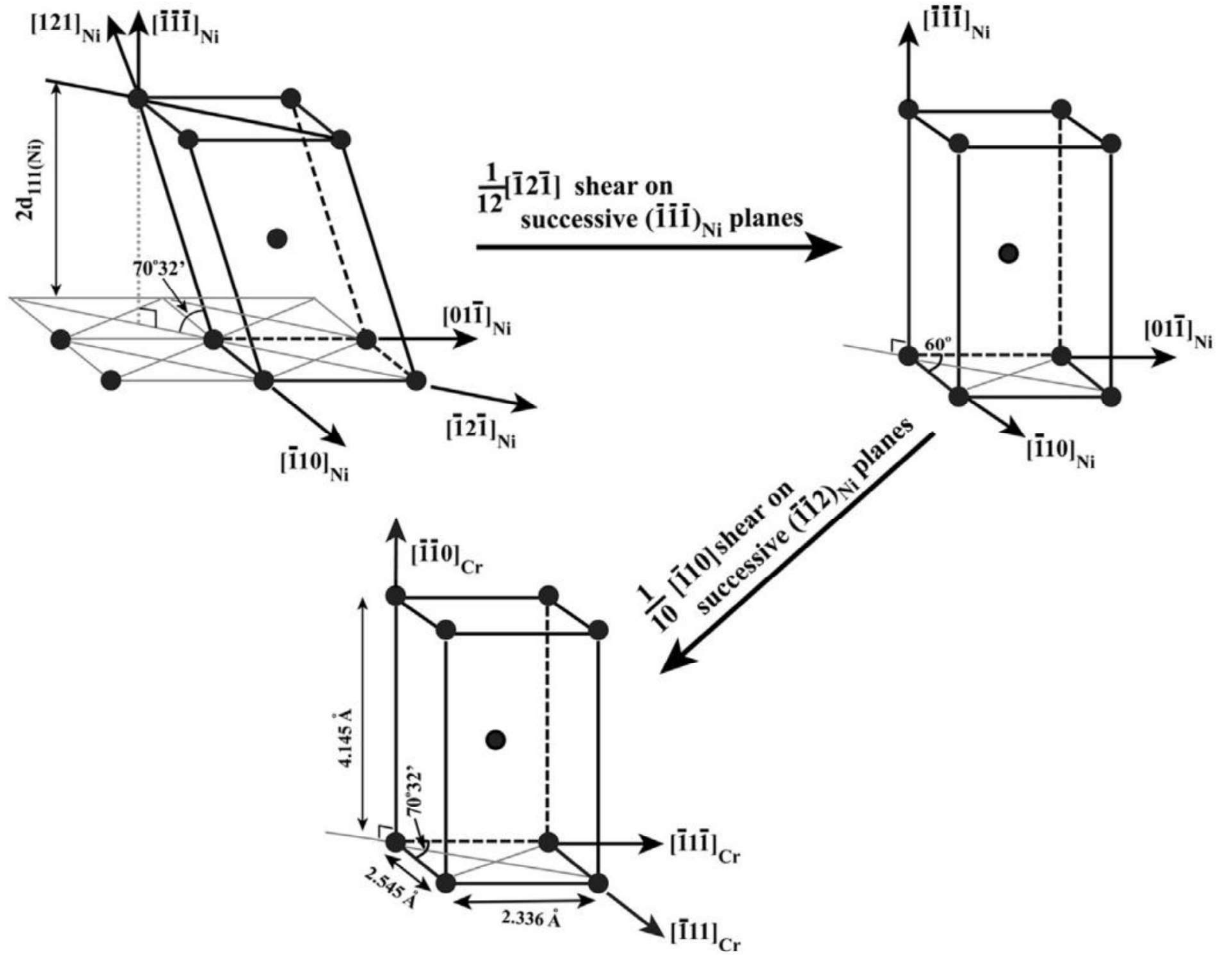

Figure 5.16. A schematic drawing depicting transformation of *fcc*-structure to *bcc* by the operation of two simple shears proposed by Kurdjumov and Sachs [124].

According to Christian [145], the role of such shear mechanisms in diffusional transformations is restricted only to the accommodation of transformation strain by plastic deformation of the transformed inclusion, though it can help in the nucleation stage also in a martensitic transformation. Faults and dislocations have been shown to reduce energy barrier for the formation of critical size nucleus in isothermal martensites [146]. Nucleation in the present case could be attributed to thermal/chemical fluctuations, and low stacking-fault energy of the γ-phase (typically ~50 mJm^{-2} [147]) would have aided it. Transformation in the present case would be associated with a small misfit of 1.8% on $\{111\}_{\gamma}$ // $\{110\}_{\alpha}$ and a misfit of about 2.7% along the overlapping direction, *i.e.*, $<\bar{1}10>_{\gamma}$ // $<1\bar{1}1>_{\alpha}$ (calculated on the basis of lattice parameters mentioned earlier [117]). Formation of the initial lath morphology of α-particles appeared to be a consequence of higher misfit strain along $[\bar{1}10]_\gamma$ // $[\bar{1}11]_\alpha$ directions. Influx of *Cr* solutes through curved α/γ interfaces due to the Gibbs-Thomson effect helped their transformation into needles.

5.4. Summary:

On the basis of above study, it could be concluded that supersaturation of chromium in the γ-phase after the precipitation of γ'-phase caused the formation of α-phase in Alloy 693. α-phase particles maintained a Kurdjumov-Sachs (*KS*) type *OR* with the γ-matrix. α-phase particles were always enveloped by the γ-phase enriched in *Al* and *Nb* solutes due to their rejection from α-phase forming regions. These particles initially had a lath morphology which assumed a needle shape during coarsening.

CHAPTER 6

MECHANICAL BEHAVIOUR OF AGED ALLOY

In Chapter 4, precipitation of γ'-phase particles has been shown to occur during ageing of Alloy 693. Depending upon ageing temperature, these particles grew and/or coarsened with time (see Figure 4.3 of Chapter 4). Further, during prolonged ageing, alloy also exhibited a tendency to precipitate out needle shape α-phase particles (see Figure 5.6 of Chapeter 5). This Chapter describes the effect of γ'- and α-phase particles on room temperature (*RT*) mechanical properties of the alloy. These properties include hardness, tensile strength and charpy impact energies of solution treated (*ST*) as well as aged alloys.

6.1. Microhardness:

Microhardness measurements of aged specimens were carried out to understand the effect of precipitation on hardness values of the alloy. Figure 6.1 shows variation in the RT hardness values of aged specimens with ageing time at different ageing temperatures. At all temperatures hardness of the aged alloys increased with time up to $0.5h$. Further change of hardness could be categorized into two broad categories with respect to (*w.r.t.*) ageing temperatures, namely, (i) samples aged at $800°C$ and $850°C$ temperatures exhibited a monotonous increase in hardness till it reached a plateau; (ii) samples aged at temperatures above $850°C$ exhibited a monotonous decrease in hardness until a plateau is reached during prolonged ageing. Table 6.1 gives the hardness values of samples aged at different temperature for different time periods.

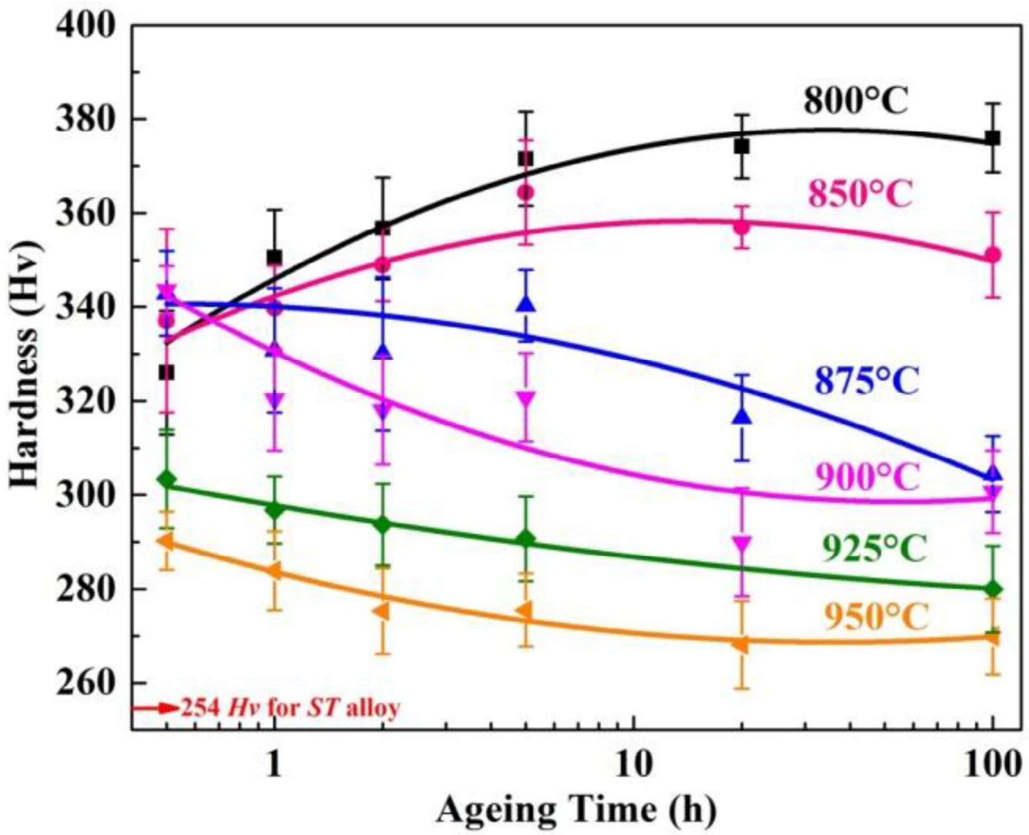

Figure 6.1. Variation in the room temperature hardness values of aged samples with ageing time (samples are aged at different temperatures).

Table 6.1. Vicker's hardness of samples aged for different ageing conditions.

Time (*h*)	**Temperature (°*C*)**					
	800	**850**	**875**	**900**	**925**	**950**
0.5	326.0±13.2	337.0±19.5	342.9±9.1	343.6±5.2	303.4±10.5	290.2±6.2
1.0	350.5±10.2	339.7±9.1	330.8±13.2	320.3±10.8	296.8±7.1	283.9±8.3
2.0	356.7±10.8	349.0±7.8	330.1±16.3	318.0±11.6	293.7±8.7	275.3±9.1
5.0	371.6±10.0	364.4±11.1	340.3±7.6	320.8±9.4	290.7±9.0	275.5±7.8
20.0	374.1±6.7	357.0±4.5	316.4±9.1	290.0±11.5	263.2±8.1	268.1±9.4
100.0	376.0±7.3	351.1±9.1	304.4±8.1	300.7±8.8	280.0±9.2	269.9±8.0

6.2. Tensile behaviour:

Mechanical properties of *ST* and aged alloys at *RT* were investigated using uniaxial tensile and Charpy impact testing. *ST* sample at *RT* exhibited yield strength (*YS*) of about 378*MPa*, ductility of about 44% and impact energy of about 56.86*J*. Aged alloys exhibited higher strength, low ductility and low impact energy in comparison to *ST*-alloy, given in Tables 6.2-6.3.

Figure 6.2 shows *RT* engineering stress (*s*) – engineering plastic strain (*e*) plots of the *ST*- sample as well as of samples aged for 0.5, 2.0 and 100*h* at different temperatures. From Figure 6.2, it is evident that there was a significant increase in the *YS* as well as *UTS* with concomitant decrease in ductility with ageing, though the latter appeared to have decrease significantly for samples aged for 100*h*. At 800°*C* strength increased with ageing time, while for samples aged in 875-950°*C* temperature regime it decreased with time. Except for 0.5*h* ageing time strength decreased with ageing temperature for a given ageing time, while for 0.5*h* ageing time strength initially increased upto 875°*C* temperature then started to decrease on further increase of temperature. On the other hand, for given ageing time ductility and impact energy initially decreased with temperature and found to increase for elevated temperatures. Tables 6.2 and 6.3 list *YS, UTS*, ductility and impact energy of *ST* and aged samples, respectively.

Table 6.2. *RT YS* (calculated as 0.2% proof strength), ultimate tensile strength(*UTS*), ductility and impact energy of *ST* alloy.

***YS* (*MPa*)**	***UTS* (*MPa*)**	**Total elongation(%)**	**Impact energy (*J*)**
378	818	44.12	56.86

Table 6.3. *RT YS* (calculated as 0.2% proof strength), *UTS*, ductility and impact energy of aged samples.

Ageing temperature (°*C*)	Time (*h*)	Property			
		***YS* (*MPa*)**	***UTS* (*MPa*)**	**Total elongation(%)**	**Impact energy (*J*)**
800	0.5	729.48	1123.94	27.39	36.44
	2.0	765.30	1182.41	27.23	20.47
	100.0	867.68	1105.43	7.00	2.55
875	0.5	752.30	1144.61	26.30	22.42
	2.0	699.50	1139.39	23.96	13.03
	100.0	642.48	930.63	8.38	4.93
900	0.5	681.99	1114.38	30.44	19.84
	2.0	658.20	1087.55	24.32	13.93
	100.0	547.34	1035.45	19.25	6.15
950	0.5	558.20	1002.29	32.06	26.47
	2.0	513.33	968.70	36.22	16.37
	100.0	433.57	963.34	32.52	14.04

6.3. Fractographic Investigations:

There are two types of fracture: ductile and brittle fracture. Ductile fracture progresses through micro-void nucleation, growth and coalescence under the influence of favourable hydrostatic tensile stress and plastic strain with the help of a defect present and/or successively generated in the material matrix during loading [148]. The defect can be inclusions, second phase particles, phase interfaces, grain boundary junctions, shear bands, twin boundaries *etc.* [149, 150]. On the other hand, brittle fracture takes place by crack propagation [151]. Brittle fractures are characterised as having little or no plastic deformation prior to failure and keeping the signature of cleavage on the fracture surfaces [152].

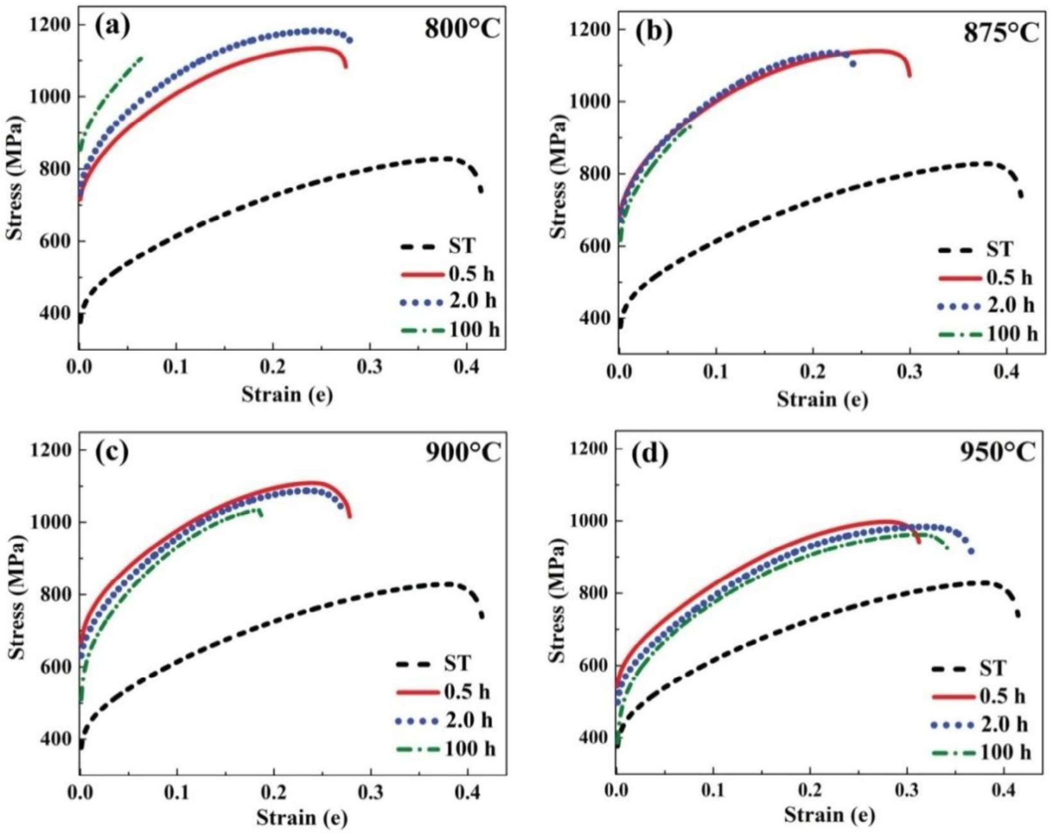

Figure 6.2. Engineering stress (s)-engineering plastic strain (e) plots of the *ST*-sample as well as samples aged for 0.5, 2.0 and 100h at: (a) 800℃; (b) 875℃; (c) 900℃; (d) 950℃.

In the current investigation, detailed fractographic examination was performed for *ST* and aged specimens to understand the deformation and fracture micro-mechanisms of the alloy under study. In order to comprehend that, extensive *SEM* investigation was carried out under secondary mode of electron imaging. Tensile fracture surface of *ST*-sample was characterized by the presence of dimples and wavy appearance of tearing ridges spread in three dimensions throughout the surface (see Figure 6.3). This clearly designates the typical ductile fracture of the alloy under this condition. Micro-void nucleation sites are also marked by the arrows in Figure 6.3(b), they were likely to be carbides and inclusions. Extensive amount of plastic deformation was noted in the *ST*-specimen compared to the rests aged specimens (see Figure 6.2).

Figures 6.4-6.5 elucidate the effect of ageing conditions (temperature and time) on the fracture characteristics of the alloy. Fracture features changed significantly with ageing. Engineering stress-engineering strain plots for aged specimens are ploted in Figure 6.2. It has been realized from the tensile plots of specimens aged at 800°C for 0.5-100*h* time (see Figure 6.2(a)) that the fracture feature characteristics (see Figure 6.4(a-c)) of 0.5 and 2.0*h* specimens were almost similar and they were more ductile than the rest specimen feature (specimen aged for 100*h*). Samples aged at 800°*C* for 0.5 and 2.0*h* exhibited ductile dimpled features accompanied with brittle cleavages (see Figure (6.4(a-b)). However, with ageing time, appearance of cleavage fracture features increased dramatically (see Figure 6.4(c)-specimen aged at 800°*C* for 100*h*). The signature of stress-strain responses for this was also noted (in Figure 6.2(a)). It has been noted from Figure 6.2(b), that the stress-strain responses of 0.5 and 2.0*h* specimens (875°*C*) were almost similar kind, hence it was apprehended that the fracture feature characteristics of these specimens would be similar kind (noted in Figure 6.4(d-f)). On the other hand, specimen aged at 875°*C* for 100*h* showed brittle characteristics of the alloy (see Figures 6.2(b) and 6.4(f)).

The stress-strain response of the alloy at 900°*C* (Figure 6.2 (c)) clearly indicated similar kind of behaviour of specimens aged for 0.5 and 2.0*h*, except 100*h* specimen which breaks earlier than rests. Fracture features of 0.5 and 2.0*h* specimens revealed inhomogeneous mixture of dimples and cleavage facets, whereas 100*h* specimen was comprised of fully cleavage facets. The stress-strain response of 0.5, 2.0 and 100*h* specimens tested at 950°*C* were almost similar kind hence it was expected that fracture characteristics of these three specimens would be similar consisting of ductile dimples and small amount of cleavages.

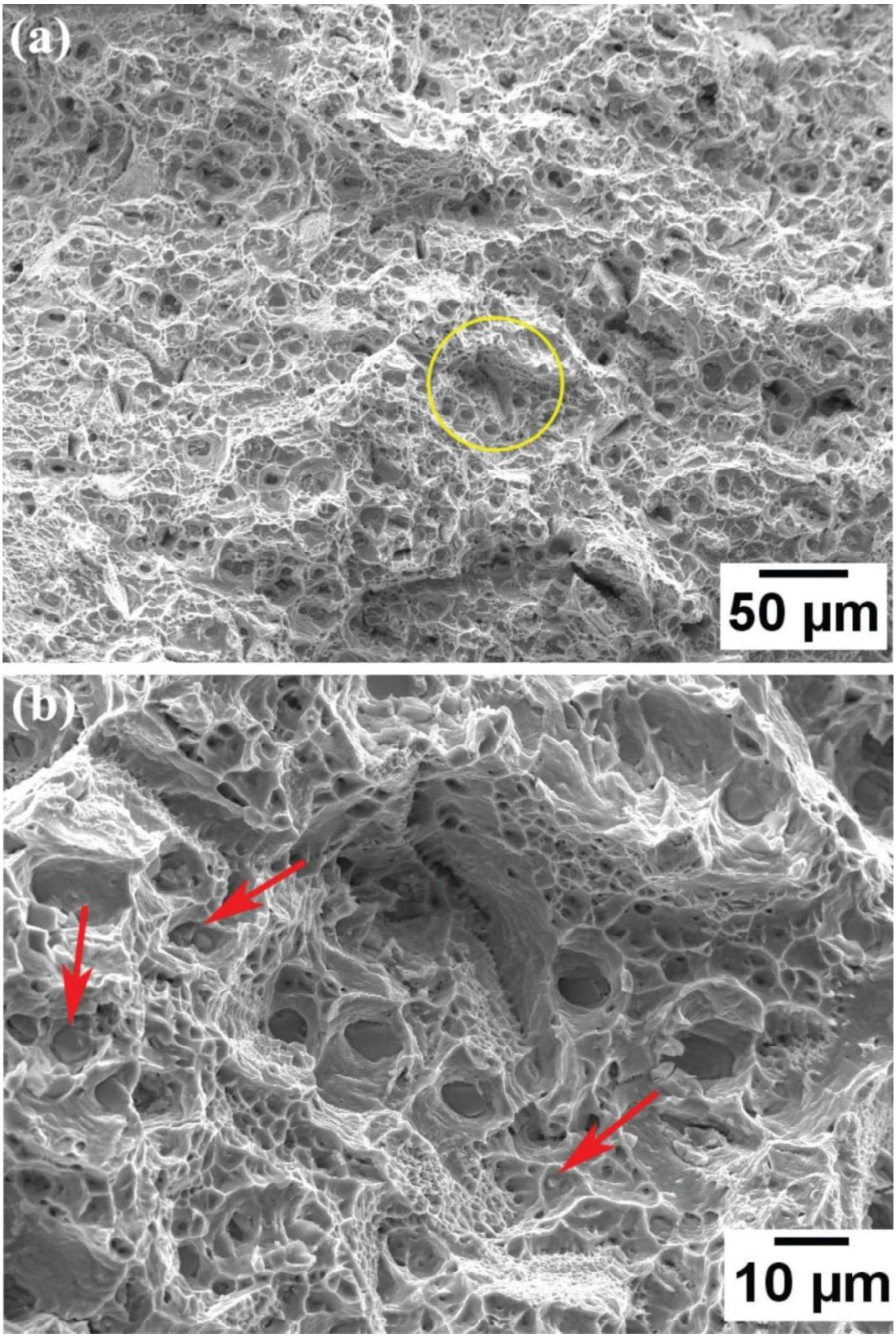

Figure 6.3. (a) Fractograph of fractured surface of *RT* tensile tested *ST*-alloy; (b) zoomed view of encircled region of Figure (a) in which carbides are marked by arrows.

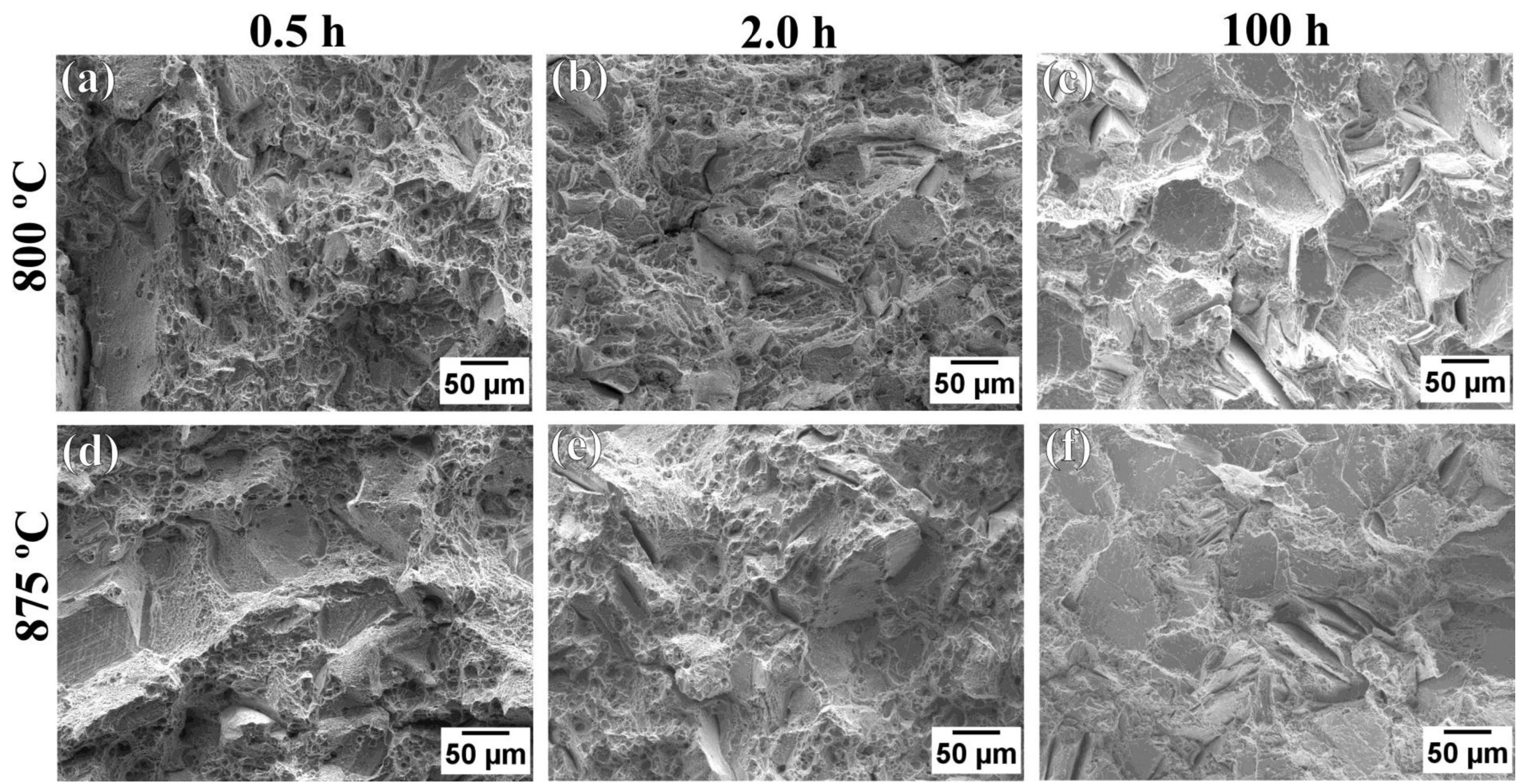

Figure 6.4. Fractographs of *RT* tensile tested aged specimens, at different ageing conditions: (a) 0.5*h* at 800º*C*; (b) 2.0*h* at 800º*C*; (c) 100*h* at 800º*C*; (d) 0.5*h* at 875º*C*; (e) 2.0*h* at 875º*C*; (f) 100*h* at 875º*C*.

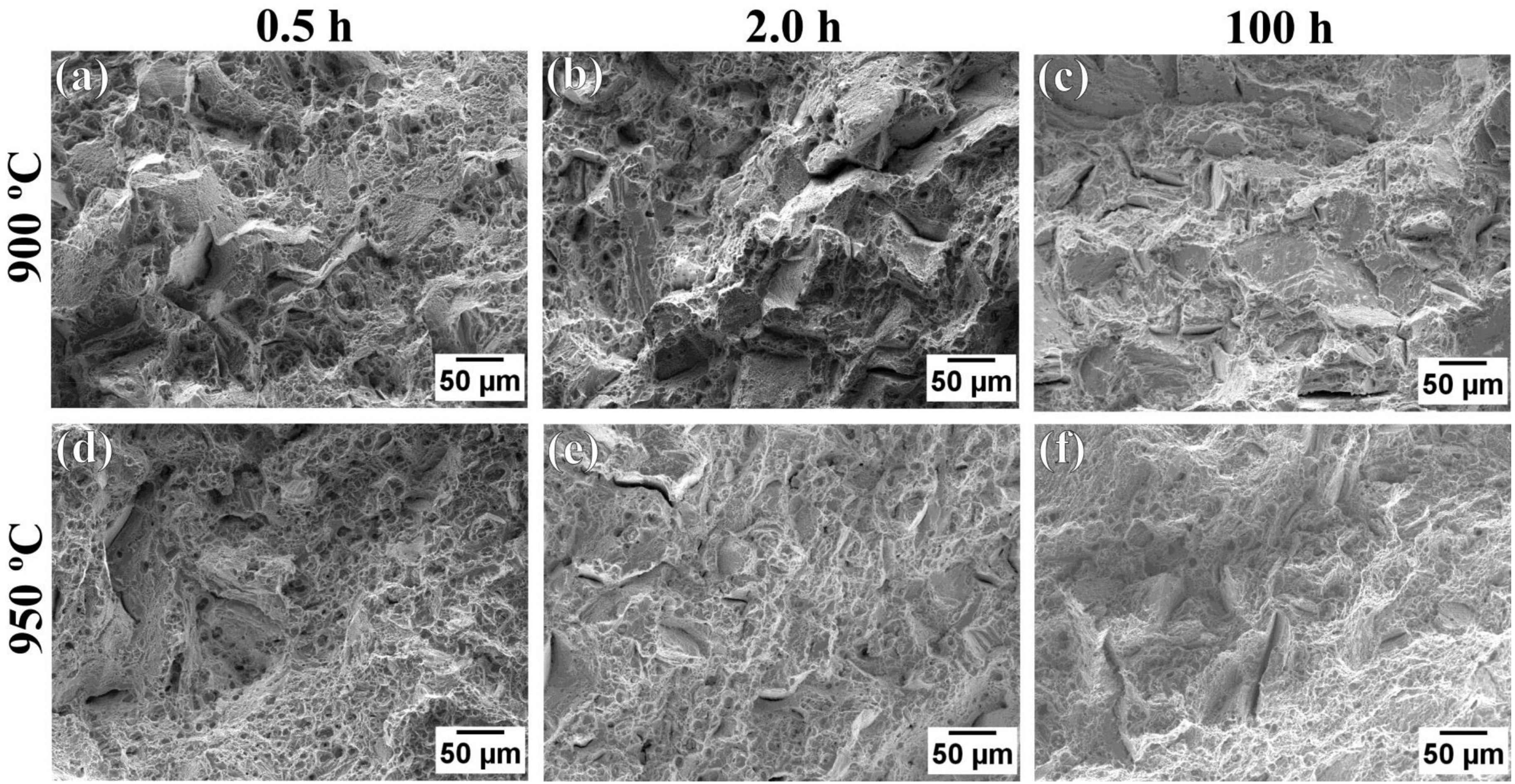

Figure 6.5. Fractographs of *RT* tensile tested aged specimens, at different ageing conditions : (a) 0.5*h* at 900º*C*; (b) 2.0*h* at 900º*C*; (c) 100*h* at 900º*C*; (d) 0.5*h* at 950º*C*; (e) 2.0*h* at 950º*C*; (f) 100*h* at 950º*C*.

6.4. Discussion:

Following sections discuss observed mechanical properties of Alloy 693 based upon contributions identified on the basis of microscopic evidences, different strengthening mechanisms and work hardening behavior of aged alloys.

6.4.1. Effect of precipitation of γ'-particles on strength of the aged alloy:

The degree of strengthening caused by a second phase hardening particles depends upon their distribution in the ductile matrix. Further, distribution of particles is described by their volume fraction, average particle size and mean inter-particle spacing, which are inter-related such that a change in one factor affects the others. For instance, at a given volume fraction of the second phase particles, an increase in particle size increases their inter-particle spacing. Difference in the strengths of alloys aged at different temperatures for different periods of time (Tables 6.2-6.3) could be attributed to combinations of one or more of these factors.

Figure 6.6 shows variations of precipitates size as well as *YS* plotted against ageing time for samples aged at different temperatures. The observed variation in their strength values (Figure 6.6 and Table 6.3) was similar with their hardness behaviour (Figure 6.1). A monotonous increase in hardness as well as strengths (both *YS* and *UTS*) with ageing at $800°C$ was consistent with increase in size and volume fraction of γ'-particles at this temperature (Tables 6.4 and 6.5), a typical feature of nucleation and growth. Precipitation of the γ'-phase particles at $850°C$ appeared to have followed a similar nucleation and growth trend, albeit at a faster rate, as reflected by a peak in hardness value within about $20h$. A small drop in hardness beyond $20h$ could be attributed to the coarsening stage. On the other hand, samples aged in the temperature regime 875–$950°C$ exhibited continuous drop in their *YS* (similar to those observed in their hardness values) and suggested of coarsening stage. In this temperature range, size of particles (Tables 6.4) increased with ageing time (Figure 6.6).

The time beyond which the strength/hardness values started to decrease (Figure 6.1, Figure 6.2 (c-d)) could be associated with the beginning of coarsening at respective temperatures.

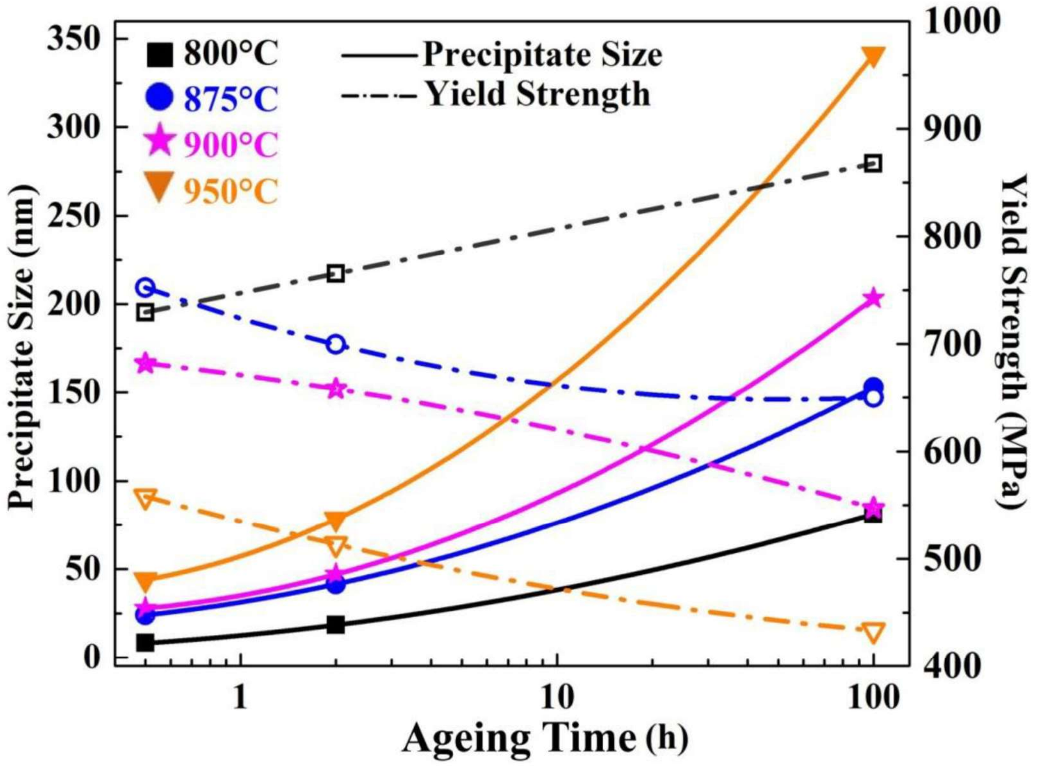

Figure 6.6. Shows variation in the precipitate size as well as *YS* plotted against ageing time for samples aged at different temperatures.

Table 6.4. Average sizes (*d*) of γ'-precipitates in aged samples.

Time (*h*)	**Average size of γ'-precipitates (*nm*)**			
	800°*C*	**875°*C***	**900°*C***	**950°*C***
0.5	8.3 ± 2.3	24.1 ± 8.5	27.9 ± 9.2	43.9 ± 10.0
2.0	18.5 ± 6.8	41.5 ± 10.1	47.0 ± 13.5	78.3 ± 17.1
100.0	81.2 ± 21.4	152.9 ± 43.1	203.2 ± 5.6	341.2 ± 4.2

Table 6.5. Number density (N_v) and volume fraction (f) of γ'-precipitates in aged samples.

Time (h)	**No. density of γ'- precipitates (N_v - number.nm^{-2}) ; volume fraction (f)**							
	800°C		**875°C**		**900°C**		**950°C**	
	N_v *10^{-4}	f	N_v *10^{-4}	f	N_v *10^{-4}	f	N_v *10^{-5}	f
0.5	6.79	0.52±0.04	2.38	0.49±0.04	1.54	0.43±0.04	8.47	0.32±0.02
2.0	7.02	0.53±0.07	1.57	0.50±0.04	1.21	0.43±0.05	3.02	0.19±0.03
100.0	7.05	0.78±0.04	0.09	0.62±0.09	0.05	0.37±0.05	0.10	0.19±0.03

6.4.2. Effect of α-phase precipitation on ductility:

It has been shown earlier in Chapter 5 that during prolonged ageing at elevated temperatures needle shape Cr-rich α-phase particles formed along with γ'-precipitates. These particles appeared to remarkably affect the plasticity of the aged alloy, which was apparent from tensile testing of samples containing α-particles (prolonged aged samples). During the coarsening of γ'-precipitates alloy exhibited a decrease of strength, though the concomitant increase of ductility was not observed (*e.g.*, see Figures 6.2(c-d)). Impact energies of these alloys also displayed trend a similar to ductility (see Table 6.3). Variations of these properties with time at 950°C are plotted in Figure 6.7. It is evident from Figure 6.7 that ductility and impact energy of an alloy decreased with the decrease of strength which is variance with general understanding. Anomalous ductility of 950°C-100h aged sample could be correlated to the precipitation of α-phase. Fractography of fractured surface of *RT* tensile tested samples revealed the presence of many α-phase precipitates particles that had broken (cleaved) during deformation (marked by arrows in Figure 6.8). *EDS* analysis of broken particles confirmed them to be Cr-rich. Appearance of cracks within these particles suggested them to be of brittle in nature.

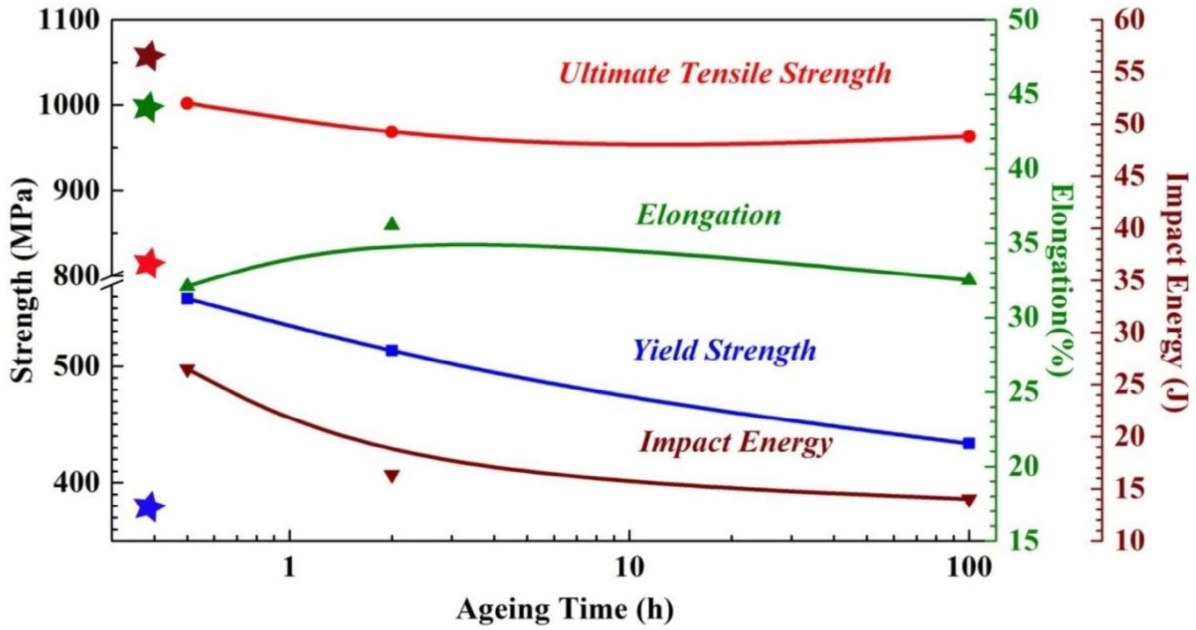

Figure 6.7. Variation in *YS*, *UTS* , percentage elongation and impact energy of samples aged at 950°*C* for 0.5-100*h* *w.r.t.* *ST*-sample (value of which are marked by star symbols in Figure).

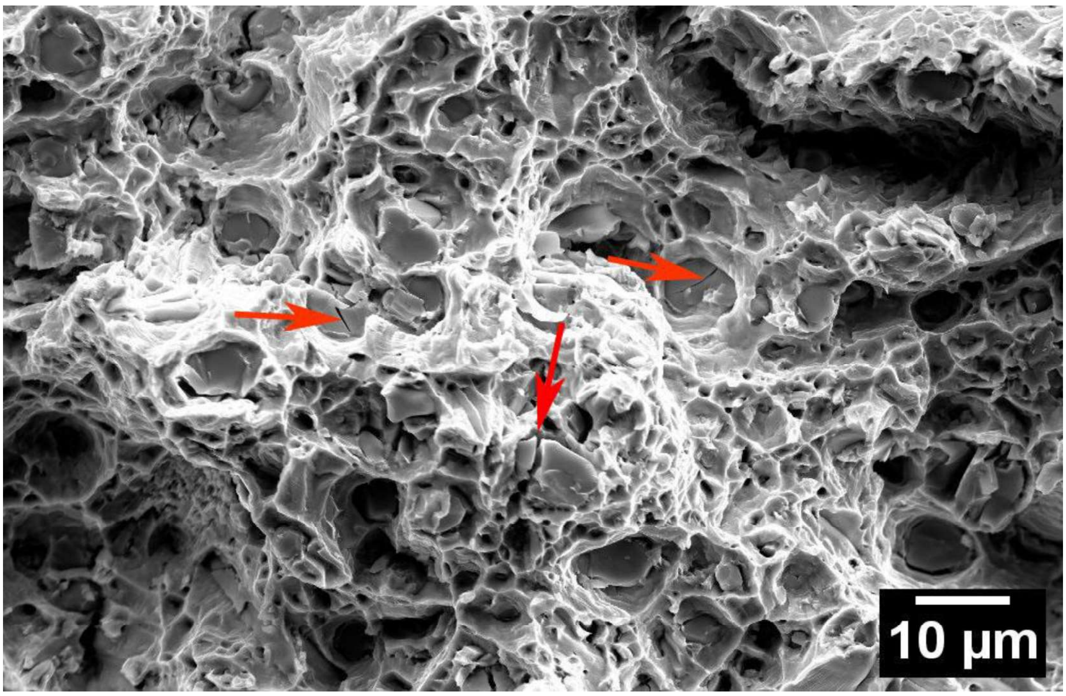

Figure 6.8. *SEM* fractograph of fractured surface of *RT* tensile tested aged sample, aged at 950°*C* for 100*h*.

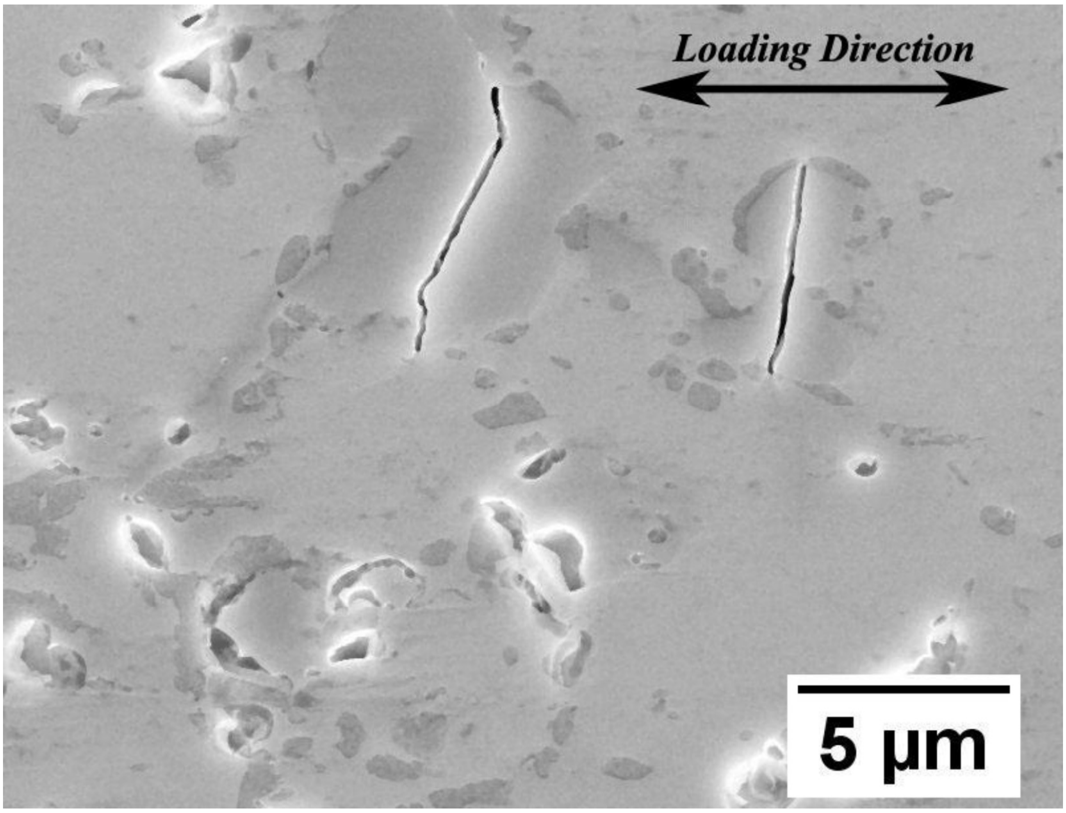

Figure 6.9. An in-situ *SE* micrograph of a sample (aged at 950°*C* for 100*h*) deformed at *RT* under tension inside the *SEM* ,taken after 3% straining. Cracking of *Cr*- rich α-phase particles within 3% strain could be noticed.

Reduced ductility in presence of these α-precipitates was also confirmed by in-situ straining experiments of prolonged aged sample (aged at 950°*C* for 100*h*) inside *SEM*. In-situ straining experiment confirmed development of cracks in α-phase precipitates (shown in Figure 6.9) within about 3% straining. This was found to be consistent with the brittle nature of *Cr*, whose maximum strength at *RT* is reported to be 282*MPa* with nil ductility, which was lower than *YS* of aged alloy and they developed cracks well before an appreciable strain.

6.4.3. Identification of mechanisms responsible for strengthening:

Flow stress of a crystalline material increases when obstacles restrict the movement of dislocations and the latter tend to overcome the former by bending, which needs extra force. The extent to which dislocations can bend is governed by the strength of obstacles (Figure 6.10).

In general, shear stress (τ_{ss}) required to bend dislocations to an angle Φ is given by [153],

$$\tau_{ss} \cong \frac{Gb}{\lambda}\cos\frac{\Phi}{2} \qquad \text{...(i)}$$

where, G is the shear strength of obstacles, b is the Burger's vector of dislocations and λ is spacing between two obstacles within a slip plane.

Strong obstacles restrict the penetration of dislocations. As the strength of obstacles increases, Φ approaches zero (Figure 6.10). On the other hand, for weak obstacles, Φ is very large and tend to approach 180° with decreasing strength of obstacles. λ is another important parameter as decrease in its value, for a given stress, would reduce the value of Φ also.

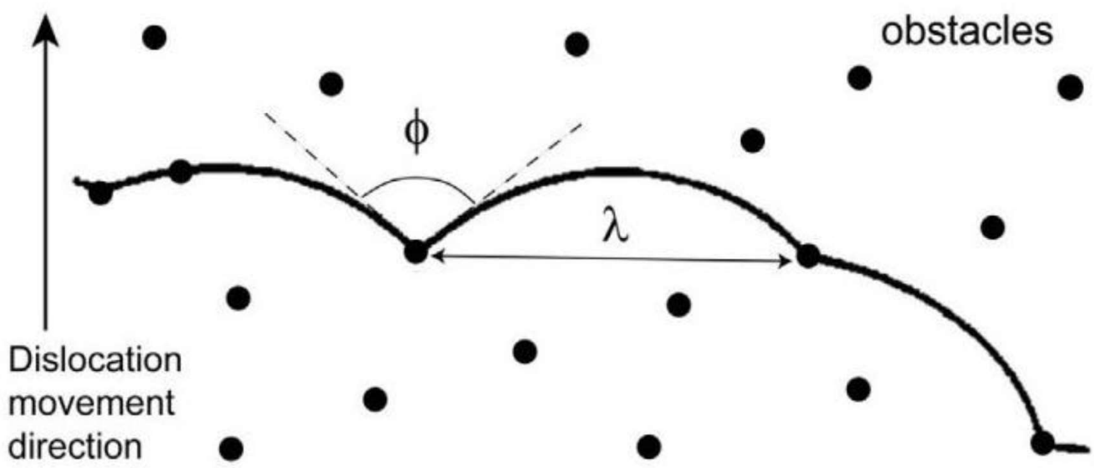

Figure 6.10. Schematic illustrating the interaction of a dislocation with obstacles (depicted by solid circles) [153].

Several factors, such as coherency strain, ordered structure, modulus effect, stacking fault energy, interfacial energy, morphology, and lattice friction stress, *etc.* act as obstacles for dislocation movement. However, in γ'-hardened *Ni*-base alloys ordered structure and coherency strain associated with γ'-phase particles primarily act as strengthening mechanisms [154, 155]. Energy associated with the formation of anti-phase boundaries (*APBs*) within ordered precipitates during their shearing also contributes to the strength. Further, shearing of ordered γ'-particles necessitates the passage of pairs of dislocations to restore their $L1_2$ ordering [156, 157] – passage of the leading dislocation of the pair destroys the $L1_2$ crystalline order and that of the trailing dislocation restores the order. Two mechanisms of shearing of ordered particles are proposed depending upon the spacing maintained between the leading and trailing dislocations relative to the size of particles (d). When precipitates are small and inter-particle spacing (λ) between them is rather large (*i.e.,* for small d and $d<\lambda$), distance between two dislocations would be large compared to the size of particles and, therefore, two dislocations of a pair would not lie within an individual precipitate. The two dislocations would be weakly coupled (*WCD*) and the mechanism is termed as "shearing by weakly coupled dislocations". In this case, critical resolved shear stress (*CRSS*) required to shear particles by weakly coupled dislocations is given by [158].

$$\tau_{ss} = \frac{1}{2} \cdot \left(\frac{\Gamma}{b}\right)^{\frac{3}{2}} \cdot \left(\frac{bdf}{T_l}\right)^{\frac{1}{2}} \cdot A - \frac{1}{2} \cdot \left(\frac{\Gamma}{b}\right) \cdot f \qquad \text{...(ii)}$$

where, Γ is the *APB* energy on {111} plane of the γ'-precipitates, T_l is line tension of dislocations in the γ-matrix, f is the volume fraction of ordered particles, b is the Burgers vector and d is particle size. A is a numerical factor dependent upon the morphology of particles and is equal to 0.72 for spherical particles [159]. When precipitates are large and inter particle spacing is of the order of particle diameter (*i.e.,* $\lambda \sim d$), the trailing dislocation would easily enter into a particle before the leading dislocation leave it. The two dislocations of a pair would remain strongly coupled (*SCD*) and mechanism is termed as "shearing by strongly coupled dislocations". The *CRSS* required to shear particles by strongly coupled dislocations is given by [160].

$$\tau_{ss} = \left(\frac{\sqrt{3}}{2}\right) \cdot \left(\frac{T_l w f^{\frac{1}{2}}}{bd}\right) \cdot \left(1.28 \frac{d\Gamma}{wT_l} - 1\right)^{\frac{1}{2}} \qquad \text{...(iii)}$$

where, w is a constant that accounts for the elastic repulsion between the strongly paired dislocations [161], and is of the order of unity [159]. The line tension, T_l, is given by [158].

$$T_l = \frac{Gb^2}{2} \qquad ...(iv)$$

Obviously, operation of either of two mechanisms would be dependent upon *d,* λ and *f* of precipitates. For a given value of *f*, shearing by *WCDs* would change to by *SCDs* beyond a value of $d \cong \lambda$.

When particles are large and widely spaced (*i.e.,* for large *d* and $d<\lambda$), shear stress required for either of the two mechanisms would be rather high but dislocations can easily bow between particles according to Orowan mechanism [54]. The *CRSS* necessary for dislocations to bow around particles is given by [158].

$$\tau_{ss} = \frac{Gb}{\lambda} \qquad ...(v)$$

and, for a given volume fraction of precipitates, λ is given as

$$\lambda = \frac{2(1-f)d}{3f} \qquad ...(vi)$$

Among the aforementioned precipitation hardening mechanisms, there would always be a competition and the one with the least *CRSS* value would dominate. For a given volume fraction of precipitates, the stress required to move dislocations through precipitates would increase with increasing size of precipitates when shearing by *WCDs* is active, while it would decrease when either shearing by *SCDs* or Orowan mechanism is active. It has been shown earlier in Chapter 4 that the alloy under study, in *ST*-condition, contains fine distribution of γ'-precipitates. The coefficient of strain hardening (*i.e.*, *n*) exhibited by its stress-strain curve of *ST*-alloy (Figure 6.13) was highest (*n*~0.84) among all the aged samples studied (which will be discussed in subsequent section). This value was also close to values reported for other *Ni*-base superalloys hardened by fine coherent particles and characterized by a mechanism involving shearing of particles by dislocations (see for example, [33, 162]). Furthermore, pairs of dislocations maintain separation of about 10–50*nm* during shearing of

γ'-particles [54, 159, 163, 164]. Since the size of particles in the *ST*-alloy (< 10*nm*) was much smaller than typical separation between two dislocations of the pair, it was not unreasonable to attribute the active hardening mechanism to *WCDs*. All aged samples exhibited values of strain hardening coefficient lower than that of the *ST*-sample, as well as sizes and volume fraction of γ'-particles were different in aged samples than *ST*-sample. Hardening mechanisms in aged alloys were tried to identify from *CRSS* values, calculated from yield strength of aged alloys. Table 6.6 gives *CRSS* (τ_{ss}) values of samples in different aged conditions. These values were obtained by dividing their *YS* values (Figure 6.2 and Table 6.3) by 3.06 (the Taylor's factor for polycrystalline *fcc* material [165]). Table 6.6 also shows increase in the *CRSS* value (*i.e.,* $\Delta\tau_{ss}$), over that of the *ST*-alloy, of aged alloys during ageing.

Table 6.6. *CRSS* values of aged samples calculated on the basis of *YS* obtained by uni-axial tensile testing.

CRSS*(*ST*)=123.53 *MPa								
Time (*h*)	**Temperature(°*C*)**							
	800		**875**		**900**		**950**	
	τ_{ss} (*MPa*)	$\Delta\tau_{ss}$ (*MPa*)	τ_{ss} (*MPa*)	$\Delta\tau_{ss}$ (*MPa*)	τ_{ss} (*MPa*)	$\Delta\tau_{ss}$ (*MPa*)	τ_{ss} (*MPa*)	$\Delta\tau_{ss}$ (*MPa*)
0.5	238.39	114.86	245.85	122.32	222.87	99.34	182.42	58.89
2.0	250.10	126.57	228.59	105.06	215.10	91.57	167.75	44.22
100.0	283.56	160.03	209.96	86.43	178.87	55.34	141.69	18.16

Figure 6.11 shows these *CRSS* values plotted against particles size at a given temperature. For samples aged at 800°*C, CRSS* values increased with increasing precipitate size, indicating the shearing of particles by *WCDs*. For samples aged in the temperature regime (875–950°*C*), the *CRSS* values continuously decreased with increase in their precipitate sizes. Since these samples exhibited nearly constant volume fraction of γ'-particles, decrease in *CRSS* values

with particle size indicated that either a mechanism involving shearing of particles by *SCDs* or dislocations bowing around them was active. Though the possibility of the operation of *SCDs* during initial stages and that of the Orowan mechanism during later stages could be the most probable. The actual active mechanism was identified on the basis of comparison of theoretical estimation of the *CRSS* for above mentioned mechanisms when the alloy contained varying volume fractions of particles of different sizes (considered up to 350*nm*). Parameters required for theoretical estimation of the *CRSS* are given in Table 6.7.

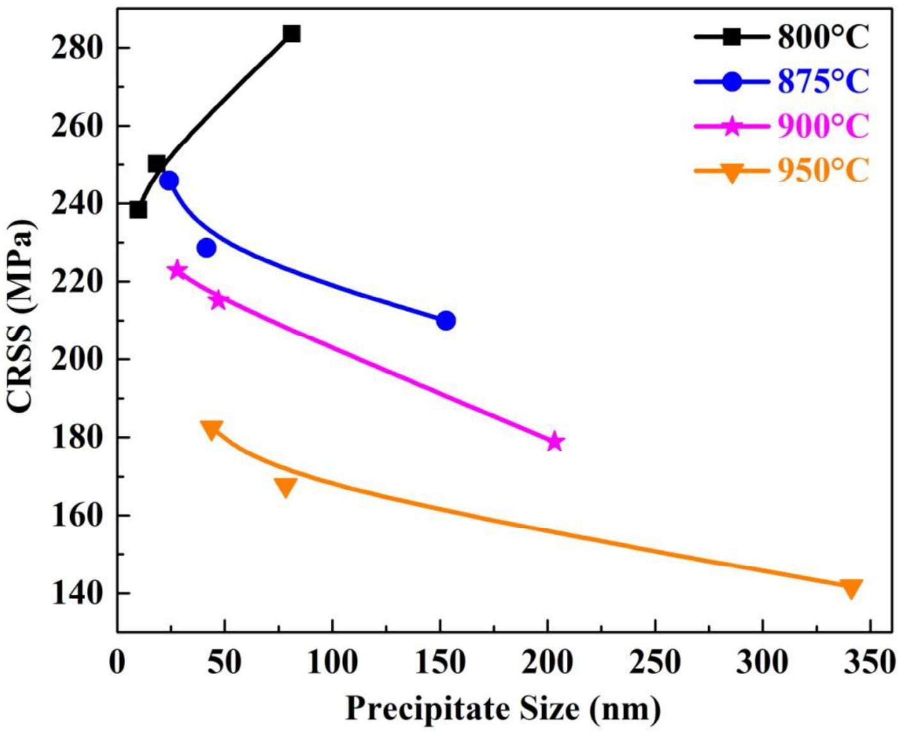

Figure 6.11. Variation in the *CRSS* values of aged samples plotted against of γ'-particles formed at different temperatures.

Representative plots of the competing mechanisms for different volume fractions, $f = 0.2$, 0.50, 0.55 and 0.80, of particles are shown in Figure 6.12. From Figure 6.12(a) it is evident that, for lower volume fractions of precipitates (*i.e.,* $f \leq 0.2$) shearing by *WCDs* was the main operative mechanism till particles grow up to an average size of 50*nm* beyond which the

Orowan bowing would dominate. However, for $f > 0.2$ (see Figure 6.12(b-d)), shearing by *SCDs* would dominate until Orowan bowing becomes operative when particles grew to very large.

Table 6.7. Parameters used for theoretical estimation of the *CRSS*.

Parameter	Value	Remark/reference
Elastic modulus (E)	196.6GPa	[2]
Poisson's ratio (υ)	0.3	[2]
Burgers vector of dislocations (b)	2.5397$Å$	Based on lattice parameters given in *ref.* [117]
APB energy on {111} plane (Γ)	180mJ/m^2	[156]

The size beyond which the Orowan mechanism would dominate was quite sensitive of the volume fraction of particles. For $f = 0.5$, the Orowan mechanism would dominate only when the size of particles d > 250nm (see Figure 6.12(b)), while it would dominate for d > 350nm if the volume fraction is increased to 0.55 (Figure 6.12(c)). On the basis of this analysis, it could be concluded that, when the volume fraction is low, for example, f <0.2 (Figure 6.12(a)), the operative mechanism of shearing by *WCDs* at small particles would be directly took over by the Orowan looping when particles would grow beyond 50nm. However, when the volume fraction is large, shearing by *SCDs* would dominate mostly. The minimum size of particles beyond which the Orowan mechanism would dominate over the shearing by *SCDs* would increase with increase in volume fraction of particles (Figure 6.12(b-c)), though for very larger volume fraction it would be practically always governed by *SCDs* (Figure 6.12(d)). On the basis of this analysis, active mechanisms of hardening in different alloys were identified and listed in Table 6.8. Mechanisms identified on the basis of this analysis appeared to be consistent as only the samples aged for 100h at 900°C and 950°C exhibited large particles where $\lambda > d$ (see Figure 4.2(i, l) of Chapter 4).

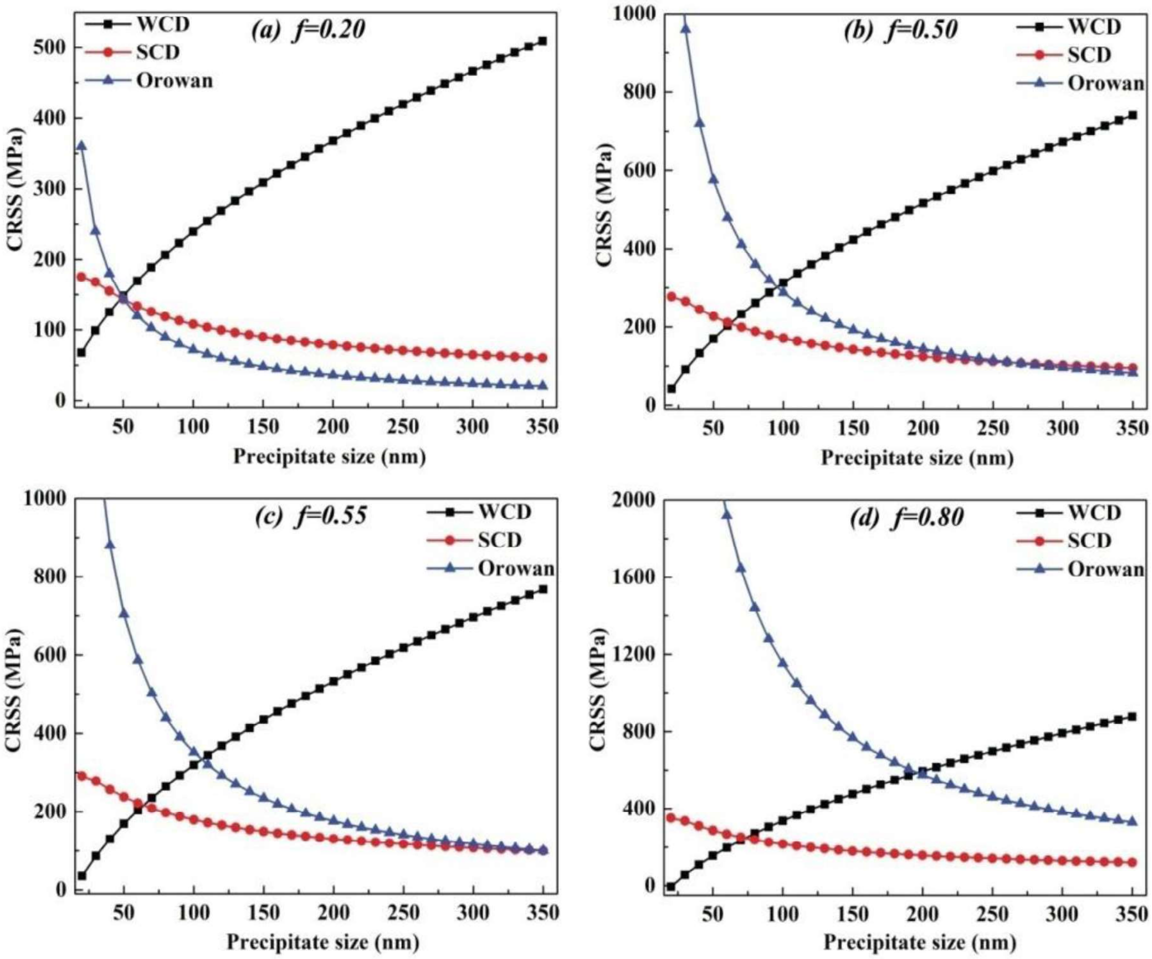

Figure 6.12. Variation in theoretically estimated *CRSS* values as a function for precipitate size for competing strengthening mechanisms involving *WCDs*, *SCDs* and Orowan bowing. The Figure shows representative plots for volume fraction: (a) $f = 0.20$; (b) $f = 0.50$; (c) $f = 0.55$; and $f = 0.80$.

Table 6.8. Strengthening mechanism identified to be active in aged alloys with different ageing treatments. In the *ST*-alloy, shearing of particles by *WCDs* was active.

Alloy State	0.5*h*	2.0*h*	100*h*
800ºC	*WCD*	*WCD*	*SCD*
875ºC	*WCD*	*WCD*	*SCD*
900ºC	*WCD*	*WCD*	Orowan
950ºC	*WCD*	Orowan	Orowan

6.4.4. Work hardening behaviour of aged alloy:

In general, strain hardening arises due to obstacles in the path of dislocation motion. These obstacle can be grain boundaries, subgrain boundaries, dislocation tangles, second phase particles, *etc*. Lattice misfit (ϵ) between matrix and second phase also indirectly affect work hardening properties of the alloys as the stress required for the passage of dislocations across precipitate/matrix interfaces would depend on it. Hence, overall work hardening in an alloy with complex microstructure would be a net result of factors mentioned above.

Table 6.9. Analytical flow relationships between true stress and true strain [28-32].

S. No.	**Flow Relationship**		**Reference**
1	**Hollomon**	$\sigma = \kappa.\ \varepsilon^n$	**[28]**
2	**Ludwik**	$\sigma = \sigma_0 + \kappa.\ \varepsilon^n$	**[30]**
3	**Voce**	$\sigma = \sigma_0 - \kappa.\ exp\ (n\ .\varepsilon)$	**[31]**
4	**Swift**	$\varepsilon = \varepsilon_0 + (\kappa.\sigma^n\ )$	**[32]**
5	**Ludwigson**	$\sigma = (\kappa.\ \varepsilon^n) + exp\ (\kappa_1 + n_1.\varepsilon)$	**[29]**

In the present case, work hardening is considered to have occurred mainly due to γ'-precipitates. In literature several flow relationships, like by Hollomon [28], Ludwigson [29], Ludwik [30], Voce [31] and Swift [32] are proposed to analyse work hardening behaviour of the material (mentioned in Table 6.9), which establish the analytical relationship between the true stress (σ_t) and true strain (ε_t). Based on the goodness of fit, flow relationship is chosen. In present study this behaviour was analysed on the basis of strain hardening exponent (n) obtained by fitting the experimentally observed RT true stress (σ_t)–true plastic strain (ε_t) flow curves for aged samples (Figure 6.13) to work hardening relationships (mentioned in Table 6.9).

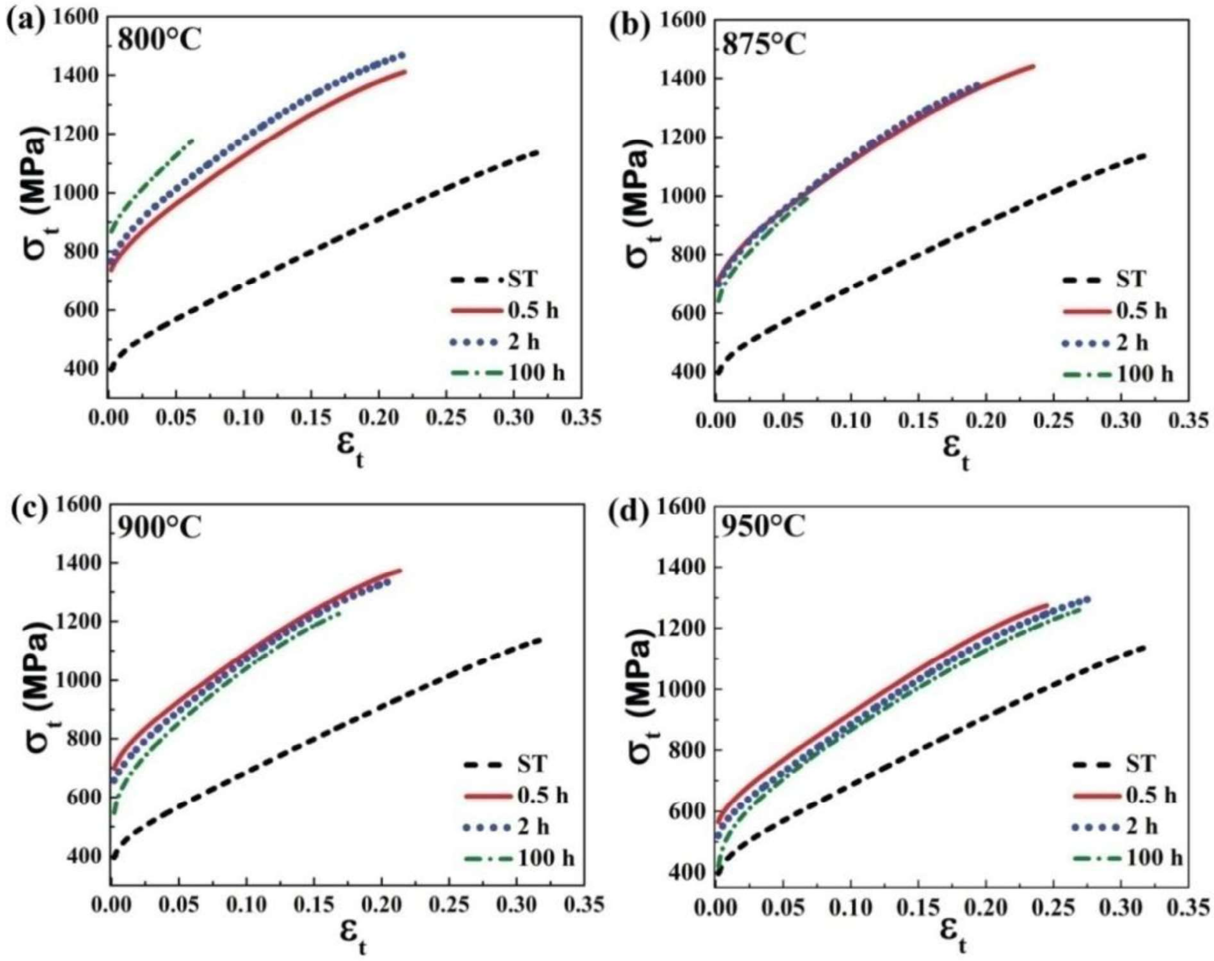

Figure 6.13. True stress (σ_t) - true plastic strain (ε_t) plots of the *ST*-sample as well as samples aged for 0.5, 2.0 and 100*h* at: (a) 800*℃*; (b) 875*℃*; (c) 900*℃*; (d) 950*℃*.

Table 6.10. Values of χ^2 (goodness of fit) for different flow relationships in fitting *RT* flow stress curves of aged alloys with different ageing treatments.

Sample State	***ST***	**800°*C***			**875°*C***			**900°*C***			**950°*C***		
Flow Relationship		**0.5*h***	**2.0*h***	**100*h***	**0.5*h***	**2.0*h***	**100*h***	**0.5*h***	**2.0*h***	**100*h***	**0.5*h***	**2.0*h***	**100*h***
Hollomon	2082.2	1885.7	1820.8	434.4	1875.5	1690.0	395.6	1895.9	1641.2	1063.1	2125.3	2005.5	1295.0
Ludwik	**13.3**	**19.8**	**28.5**	**1.2**	**22.8**	**17.9**	**3.4**	**19.6**	**39.5**	**11.6**	**23.2**	**61.2**	**23.0**
Voce	138.7	468.2	698.1	48.8	639.7	536.7	122.9	420.1	603.7	685.0	289.7	557.1	927.3
Swift	*FDC*	*FDC*	*FDC*	*FDC*	*FDC*	*FDC*	*FDC*	*FDC*	*FDC*	*FDC*	*FDC*	*FDC*	*FDC*
Ludwigson	20.1	92.4	128.3	*FDC*	111.6	89.9	*FDC*	77.1	140.6	51.0	*FDC*	177.5	80.6

****FDC***- Fit didn't converge.

Sum of residual squares (χ^2 values - which represents goodness of fit) of curves fitting are given in Table 6.10 and it is evident from these data that Ludwik flow relationship gave best fit out of all relationships [30]. Ludwik relationship is given by: $\sigma = \sigma_0 + \kappa.\ \varepsilon^n$, where, σ_0 is true stress at $\varepsilon = 0$ and κ is a constant called strength factor. Fitted values of σ_0, κ and n are given in Table 6.11. *ST*-alloy containing fine γ'-particles exhibited highest value of n, which was close to values reported for other *Ni*-base superalloys hardened by similar sized coherent particles [33]. These particles were characterized by easy shearing by dislocations and provide low resistance shear bands for subsequent dislocations. High value of n in such cases could thus be attributed to dislocation-dislocation interactions within these bands. Value of the n decreased in aged alloys *w.r.t.* *ST*-alloy.

In general, n value decreases as the volume fraction (f) increases for a given particle size (d), and it decreases with decreasing d when f is fixed. However, in the present work, f and d both changed simultaneously in most of cases (Tables 6.4 and 6.5). Above arguments are therefore not valid when microstructures change continuously. For such cases, Zhang et *al.* [34] have demonstrated that the inter-particle spacing (λ) relates better to n as the value of n increases linearly with increase in λ, irrespective of volume fraction. Observed values of n in aged samples were thus in conformity with Zhang et *al*. [34] in most of the cases. Deviations observed in some cases, as in samples aged for long durations at 900°*C* and 950°*C*, could be attributed to the precipitation of α-phase precipitates. Precipitation of α-precipitates appeared to have reduced the value of n. This effect was evident when one compares the hardening behaviour of sample aged at 950°*C* for 0.5*h* with that of the sample aged at 900°*C* for 100*h*. Volume fractions of γ'-precipitates in the two samples were nearly similar (Table 6.5), while average sizes of particles are about 45*nm* and 203*nm*, respectively (Table 6.4). The observed values of n for the two cases were 0.77 (at 950°*C* for 0.5*h*) and 0.61 (at 900°*C* for 100*h*) (Table 6.11), while it was expected to be higher for the latter. This variance of observed values could be attributed to the presence of α-particles in alloy aged at 900°C for 100h as that is the only other difference between two microstructures. Decrease in hardening coefficient due to the presence of α-particles could be related to their brittle nature, shown earlier. These particles acted as crack initiation sites, which would limit the strength of the material. During deformation tearing of these particles take place away from the matrix.

Table 6.11. Work hardening parameters obtained by fitting *RT* flow stress curves of aged alloys with different ageing treatments to Ludwik equation [30].

Alloy state		**Work hardening parameters**		
Ageing temperature (°*C*)	**Ageing time (*h*)**	σ_0 (*MPa*)	κ (*MPa*)	***n***
ST		411.81	1930.12	0.84
800	**0.5**	707.24	2053.62	0.69
	2.0	724.94	2036.40	0.65
	100.0	846.18	2620.43	0.74
875	**0.5**	676.88	2047.38	0.68
	2.0	665.71	2176.36	0.67
	100.0	615.85	2204.51	0.66
900	**0.5**	676.74	2117.33	0.71
	2.0	614.98	2111.27	0.67
	100.0	518.21	2141.67	0.61
950	**0.5**	554.32	2173.56	0.77
	2.0	496.64	2084.32	0.72
	100.0	437.72	1982.08	0.64

6.5. Summary:

On the basis of the above study it can be concluded that precipitation of γ'-particles significantly enhanced the strength of aged alloys *w.r.t.* the *ST*-alloy. Aged alloys exhibited anomalous decrease in ductility during coarsening of γ'-particles, which was attributed to α-particles that precipitated during the γ'-particle*s* coarsening period. Precipitation of the α-phase has embrittlement effect on the alloy as its precipitates act as sites for easy crack initiation due to their inherent brittle nature. Aged alloys with fine γ'-particles and low volume fraction exhibited ductile kind of fracture mechanism while with increasing size and volume fraction fracture mode changed to brittle nature. Different precipitation hardening mechanisms were active in different microstructural conditions. When the volume fraction of γ'-particles was low, the operative mechanism of shearing by *WCDs* for small particles was directly taken over by the Orowan looping beyond a certain size of particles. Shearing by *SCDs* dominates mostly when the volume fraction of particles was large. Alloy aged for $0.5h$ at $875°C$ gave best combination of strength and ductility.

CHAPTER 7

CONCLUSION AND SCOPE FOR FUTURE RESEARCH

7.1. Conclusion of work:

The present dissertation entitled "Precipitation Behaviour and its Effect on Mechanical Properties of Alloy 693" reports investigations of microstructural instabilities, *i.e.*, precipitation behaviour of the γ'- and α-phases and its effect on room temperature mechanical properties of Alloy 693. On the basis of present study, following conclusions were made:

- ✓ Alloy 693 exhibited a tendency to precipitate out homogeneously distributed fine γ'-particles during water quenching followed by solution annealing treatment. During ageing at 800-950$°C$ temperatures the size of these particles increased with ageing time and their volume fraction increased / decreased depending upon ageing temperature. For instance, at temperatures $\leq 875°C$ both size and volume fraction of γ'-particles increased with ageing time, while at higher temperatures (>875$°C$) volume fractions of the γ'-particles increased for initial ageing times and reduced during prolonged ageing. This behaviour was found to be because of under-saturated state of the γ-matrix (*w.r.t.* γ'-forming solutes) at these temperatures. Due to the under-saturated state of the γ-matrix dissolution of already formed γ'-phase particles continued till composition of the γ-matrix saturates at these temperatures.
- ✓ The morphology of γ'-particles during ageing in Alloy 693 was found to evolve continuously from spherical shape for small sizes to cuboidal shape for larger sizes. Such morphological transformation occurred at different sizes of particles at different temperatures. The lattice parameter studies and microstructural investigations suggested that variation in misfit strain between γ-γ' phases and the strain field

interaction of neighbouring particles for different number density and their volume fraction at different temperatures were responsible for such changes.

- ✓ The γ'-particles found to be coarsened more rapidly at high temperatures. The coarsening kinetics study showed that a volume controlled diffusion of solutes governed coarsening kinetics as suggested by *LSW* theory.
- ✓ In addition to γ'-precipitates, Alloy 693 also exhibited a tendency to form *Cr*-rich α-phase particles during ageing at temperatures $\geq 800°C$ in addition to γ'-phase,. The α-phase particles initially had a lath morphology which later assumed a needle shape during prolonged ageing. The precipitation of γ'-phase particles made matrix composition unstable *w.r.t.* the *Cr* concentration that caused the precipitation of *Cr*-rich α-phase particles. Crystallographic analysis revealed that α-phase particles maintained a Kurdjumov-Sachs (*KS*) type *OR* with γ-matrix.
- ✓ Strength of the Alloy 693 significantly enhanced after the precipitation of γ'-particles *w.r.t.* the solution treated alloy, though at the cost of its ductility. Strength of the aged alloy increased during the growth and decreased during the coarsening of the γ'-particles. This behaviour was explained on the basis of different strengthening mechanisms like shearing of particles by *WCDs* or *SCDs* and by the Orowan looping. Different mechanisms were active for different particle sizes and volume fractions. For lower volume fraction, strengthening due to *WCDs* for small particles was directly taken over by the Orowan looping for larger particles. Shearing by *SCDs* dominates mostly when the volume fraction of particles was large. In addition, precipitation of *Cr*-rich α-phase particles was found to embrittle the alloy as exhibited by anomalous reduction of its ductility. This was due to inherent brittle nature of the α-particles that acted as sites for easy crack initiation.
- ✓ Alloy aged for $0.5h$ at $875°C$ gave best combination of strength and ductility.

7.2. Scope for future research:

Alloy 693 require excellent combination of mechanical strength, microstructural stability and corrosion/oxidation resistance for their better performance in severe corrosive environment, *e.g.*, for management of high level nuclear waste [4] and petrochemical processing industry [2]. In such applications, alloy must withstand environmental assisted cracking mostly caused by H_2, H_2S and CO_2, and creep issues. In the present work, various microstructural parameters have been identified that contribute to changes of mechanical properties of Alloy 693 at room temperature. Further, to augment the understanding of the Alloy 693, following are few future studies:

- ✓ Mechanical properties studies of the Alloy 693 at high temperatures.
- ✓ Corrosion studies of aged Alloy 693 in different environment.
- ✓ Slow strain rate testing (*SSRT*) to evaluate the susceptibility of the alloy against environmental cracking.
- ✓ Creep behaviour of Alloy 693.

REFERENCES

[1] http://www.specialmetals.com/assets/documents/alloys/inconel/inconel-alloy-690.pdf.

[2] http://www.specialmetals.com/assets/documents/alloys/inconel/inconel-alloy-693.pdf.

[3] J. H. Hsu, J. W. Newkirk, C. W. Kim, C. S. Ray, R. K. Brow, M. E. Schlesinger, D. E. Day, "Corrosion of Inconel 690 and Inconel 693 in an iron phosphate glass melt", Corrosion Science, 75 (2013) 148-157.

[4] D. Zhu, C. W. Kim, D. E. Day, "Corrosion behavior of Inconel 690 and 693 in an iron phosphate melt", Journal of Nuclear Materials, 336 (2005) 47-53.

[5] A. Taylor, R.W. Floyd, "The constitution of nickel-rich alloys of the nickel chromium aluminium system", Journal of the Institute of Metals, 81 (1952-1953) 451-464.

[6] D. West, "Ternary equilibrium diagrams", Springer Science & Business Media, (1982) 94-99.

[7] N. Dupin, I. Ansara, B. Sundman, "Thermodynamic re-assessment of the ternary system Al-Cr-Ni", Calphad, 25 (2001) 279-298.

[8] L. Kaufman, H. Nesor, "Calculation of superalloy phase diagrams: Part I", Metallurgical Transactions, 5 (1974) 1617-1621.

[9] http://rsbweb.nih.gov/ij/.

[10] R.C. Reed, M.P. Jackson, Y.S. Na, "Characterization and modeling of the precipitation of the sigma phase in UDIMET 720 and UDIMET 720Li", Metallurgical and Materials Transactions A, 30 (1999) 521-533.

[11] ASTM E8M-04, "Standard Test Methods for Tension Testing of Metallic Materials", ASTM International, West Conshohocken PA , USA (2004).

[12] ASTM E23-05, "Standard Test Methods for Notched Bar Impact Testing of Metallic Materials", ASTM International, West Conshohocken PA , USA (2005).

[13] J.B. Singh, A. Verma, M.K. Thota, J.K. Chakravartty, "Brittle failure of Alloy 693 at elevated temperatures", Materials Science and Engineering: A, 616 (2014) 88-92.

[14] Shabana Khan, J.B. Singh, A. Verma, "Precipitation behaviour of γ′ phase in Alloy 693", Materials Characterization, 119 (2016) 24-33.

[15] R.C. Reed, "The superalloys: fundamentals and applications", Cambridge university press, (2008) 33-120.

[16] D.A. Porter, K.E. Easterling, Phase Transformations in Metals and Alloys, (Revised Reprint), VNR International, 1989, p. 46.

[17] Shabana Khan, J.B. Singh, A. Verma, "Age hardening behaviour of Alloy 693", Materials Science and Engineering: A, 697 (2017) 86-94.

[18] Shabana Khan, J.B. Singh, A. Verma, M. Karri, "Precipitation of a chromium-rich α-phase in Alloy 693 and its effect on tensile properties", Materials Science and Engineering: A, 686 (2017) 176-183.

[19] I.M. Lifshitz, V.V. Slyozov, "The kinetics of precipitation from supersaturated solid solutions", Journal of Physics and Chemistry of Solids, 19 (1961) 35-50.

[20] C. Wagner, "Theorie der Alterung von Niederschlägen durch Umlösen (Ostwald-Reifung)", Zeitschrift für Elektrochemie, Berichte der Bunsengesellschaft für physikalische Chemie, 65 (1961) 581-591.

[21] R.A. Ricks, A.J. Porter, R.C. Ecob, "The growth of γ′ precipitates in nickel-base superalloys", Acta Metallurgica, 31 (1983) 43-53.

[22] M. Doi, T. Miyazaki, "γ′ precipitate morphology formed under the influence of elastic interaction energies in nickel-base alloys", Materials Science and Engineering, 78 (1986) 87-94.

[23] S. Meher, S. Nag, J. Tiley, A. Goel, R. Banerjee, "Coarsening kinetics of γ′ precipitates in cobalt-base alloys", Acta Materialia, 61 (2013) 4266-4276.

[24] S.M. Merchant, M.R. Notis, "A review: Constitution of the Al-Cr-Ni system", Materials Science and Engineering, 66 (1984) 47-60.

[25] S. Zhao, X. Xie, G.D. Smith, S.J. Patel, "Microstructural stability and mechanical properties of a new nickel-based superalloy", Materials Science and Engineering: A, 355 (2003) 96-105.

[26] H.-y. Li, X.-p. Song, Y.-l. Wang, G.-l. Chen, "Coarsening and age hardening behaviors of γ' particles in GH742 during high temperature treatment", Journal of Iron and Steel Research, International, 16 (2009) 81-86.

[27] J.H. Westbrook, "Chromium and chromium alloys", in Kirk-Othmer Encyclopedia of Chemical Technology, 3rd ed. (M. Grayson, Ed.), John Wiley and Sons, New York, 6 (1979) 54-62.

[28] J.H. Hollomon, "Tensile deformation", AIME Transactions, 12 (1945) 1-22.

[29] D. Ludwigson, "Modified stress-strain relation for FCC metals and alloys", Metallurgical and Materials Transactions B, 2 (1971) 2825-2828.

[30] P. Ludwik, "Elemente der technologischen Mechanik", Springer-Verlag, 2013.

[31] E. Voce, "The relationship between stress and strain for homogeneous deformation", J Inst Met, 74 (1948) 537-562.

[32] H.W. Swift, "Plastic instability under plane stress", Journal of the Mechanics and Physics of Solids, 1 (1952) 1-18.

[33] M. Sundararaman, P. Mukhopadhyay, S. Banerjee, "Deformation behaviour of γ'' strengthened Inconel 718", Acta Metallurgica, 36 (1988) 847-864.

[34] Z. Fan, H. Mingzhi, S. Deke, "The relationship between the strain-hardening exponent n and the microstructure of metals", Materials Science and Engineering: A, 122 (1989) 211-213.

[35] H. Kim, S. Chun, X. Yao, Y. Fang, J. Choi, "Gamma prime (γ′) precipitating and ageing behaviours in two newly developed nickel-base superalloys", Journal of Materials Science, 32 (1997) 4917-4923.

[36] T. Wang, G. Sheng, Z.-K. Liu, L.-Q. Chen, "Coarsening kinetics of γ′ precipitates in the Ni–Al–Mo system", Acta Materialia, 56 (2008) 5544-5551.

[37] A.R.P. Singh, S. Nag, S. Chattopadhyay, Y. Ren, J. Tiley, G.B. Viswanathan, H.L. Fraser, R. Banerjee, "Mechanisms related to different generations of γ′ precipitation during continuous cooling of a nickel base superalloy", Acta Materialia, 61 (2013) 280-293.

[38] B. Reppich, W. Kühlein, G. Meyer, D. Puppel, M. Schulz, G. Schumann, "Duplex γ′ particle hardening of the superalloy Nimonic PE 16", Materials Science and Engineering, 83 (1986) 45-63.

[39] A.D. Sequeira, H.A. Calderon, G. Kostorz, J.S. Pedersen, "Bimodal size distributions of γ′ precipitates in Ni-Al-Mo—I. Small-angle neutron scattering", Acta Metallurgica et Materialia, 43 (1995) 3427-3439.

[40] R. Radis, M. Schaffer, M. Albu, G. Kothleitner, P. Pölt, E. Kozeschnik, "Multimodal size distributions of γ′ precipitates during continuous cooling of UDIMET 720 Li", Acta Materialia, 57 (2009) 5739-5747.

[41] A.R.P. Singh, S. Nag, J.Y. Hwang, G.B. Viswanathan, J. Tiley, R. Srinivasan, H.L. Fraser, R. Banerjee, "Influence of cooling rate on the development of multiple generations of γ′ precipitates in a commercial nickel base superalloy", Materials Characterization, 62 (2011) 878-886.

[42] R. Halder, R.S. Dutta, P. Sengupta, I. Samajdar, G.K. Dey, "Microstructural studies on Alloy 693", Journal of Nuclear Materials, 453 (2014) 91-97.

[43] B.A. Baker, G.D. Smith, V.W. Hartmann, L.E. Shoemaker, S. McCoy, "Nickel-base material solutions to metal dusting problems", Corrosion NACE Conference NACE (2002) Paper No. 02394.

[44] J.R. Davis, "ASM specialty handbook: heat-resistant materials", ASM International (1997) 03-30.

[45] Matthew J. Donachie, Stephen J. Donachie, "Superalloys: a technical guide", ASM International USA, New York (2002) 11-22.

[46] C. T. Sims, N. S. Stoloff, W. C. Hagel, "Superalloys II", John Wiley & Sons (1987) 03-26.

[47] W. S. Walston, "Coating and surface technologies for turbine airfoils", K.A. Green, T.M. Pollock, H. Harada, T.E. Howson, R.C. Reed, J.J. Schirra, S. Walston (Eds.), Superalloys 2004, The Minerals, Metals and Materials Society (TMS), Warrendale (PA, USA) (2004) 579-588.

[48] Matthew J. Donachie, Stephen J. Donachie, "Superalloys: a technical guide", ASM International USA, New York (2002) 287-322.

[49] Monika Losertova, "Advanced Materials", Technical University of Ostrava (2014) 17-42.

[50] P. Caron, "High γ' solvus new generation nickel-based superalloys for single crystal turbine blade applications", K.A. Green, T.M. Pollock, H. Harada, T.E. Howson, R.C. Reed, J.J. Schirra, S. Walston (Eds.), Superalloys 2000, The Minerals, Metals and Materials Society (TMS), Warrendale (PA, USA) (2000) 737-746.

[51] Matthew J. Donachie, Stephen J. Donachie, "Superalloys: a technical guide", ASM International USA, New York (2002) 25-40.

[52] G. Sabol, R. Stickler, "Microstructure of nickel-based superalloys", physica status solidi (b), 35 (1969) 11-52.

[53] C. T. Sims, N. S.Stoloff, W. C. Hagel, "Superalloys II", John Wiley & Sons (1987) 99-133.

[54] R.W. Kozar, A. Suzuki, W.W. Milligan, J.J. Schirra, M.F. Savage, T.M. Pollock, "Strengthening mechanisms in polycrystalline multimodal nickel-base superalloys", Metallurgical and Materials Transactions A, 40 (2009) 1588-1603.

[55] S. Zhao, X. Xie, G.D. Smith, S.J. Patel, "Research and improvement on structure stability and corrosion resistance of nickel-base superalloy INCONEL alloy 740", Materials & Design, 27 (2006) 1120-1127.

[56] C.J. Cowen, P.E. Danielson, P.D. Jablonski, "The microstructural evolution of inconel Alloy 740 during solution treatment, aging, and exposure at 760°C", Journal of Materials Engineering and Performance, 20 (2011) 1078-1083.

[57] Matthew J. Donachie, Stephen J. Donachie, "Superalloys: a technical guide", ASM International USA, New York (2002) 211-286.

[58] G.K. Dey, "Physical metallurgy of nickel aluminides", Sadhana, 28 (2003) 247-262.

[59] A.S. Tapia, "Computational design of nickel based superalloys for industrial gas turbine components", (M.S. thesis) University of Florida, (2006).

[60] P.S. Kotval, "The microstructure of superalloys", Metallography, 1 (1969) 251-285.

[61] Y. Mishima, S. Ochiai, T. Suzuki, "Lattice parameters of Ni(γ), $Ni_3Al(\gamma')$ and $Ni_3Ga(\gamma')$ solid solutions with additions of transition and B-subgroup elements", Acta Metallurgica, 33 (1985) 1161-1169.

[62] V. Guttman, "Phase stability in high temperature alloys", Applied Science Publishers Ltd. London, (1981) 126-127.

[63] A.J. Bradley, "Microscopical studies on the Iron-Nickel-Aluminium system. Part II-the breakdown of the body-centred cubic lattice", Journal of the Iron and Steel Institute, 168 (1951) 233-244.

[64] M. Palm, W. Sanders, G. Sauthoff, "Phase equilibria in the Ni-Al-Ta system", Zeitschrift für Metallkunde, 87 (1996) 390-398.

[65] P. Nash, "Phase diagrams of binary nickel alloys", ASM International(USA), (1991) 394.

[66] A.K. Sinha, "Close-packed ordered AB_3 structures in ternary alloys of certain transition metals", Trans Met Soc AIME, 245 (1969) 911-917.

[67] Y.Q. Chen, E. Francis, J. Robson, M. Preuss, S.J. Haigh, "Compositional variations for small-scale gamma prime (γ′) precipitates formed at different cooling rates in an advanced Ni-based superalloy", Acta Materialia, 85 (2015) 199-206.

[68] M. Doi, T. Miyazaki, "Microstructural developement under the influence of elastic energy in Ni-base alloys containing γ′ precipitates", S. Reichman, D.N. Duhl, G. Maurer, S. Antolovich, C. Lund (Eds.), Superalloys 1988, The Metallurgical Society, Warrendale (PA, USA) (1988) 663-672.

[69] M. Doi, T. Miyazaki, T. Wakatsuki, "The effect of elastic interaction energy on the morphology of γ′ precipitates in nickel-based alloys", Materials Science and Engineering, 67 (1984) 247-253.

[70] G.N. Maniar, J.E. Bridge, H.M. James, G.B. Heydt, "Correlation of gamma-gamma prime mismatch and strengthening in Ni/Fe-Ni base alloys containing aluminum and titanium as hardeners", Metallurgical Transactions, 1 (1970) 31-42.

[71] Y. Wang, Z.K. Liu, L.Q. Chen, "Thermodynamic properties of Al, Ni, NiAl, and Ni_3Al from first-principles calculations", Acta Materialia, 52 (2004) 2665-2671.

[72] A. Royer, P. Bastie, D. Bellet, CME Zeyen, "Relation between structural properties and morphology of the γ′ precipitates of the monocrystalline nickel-based superalloy AM1", Journal de Physique IV, 4 (1994) 105-110.

[73] A. Royer, P. Bastie, D. Bellet, J.L. Strudel, "Temperature dependence of the lattice mismatch of the Am1 superalloy influence of the γ' precipitates morphology", Philosophical Magazine A, 72 (1995) 669-689.

[74] S. Mannan, S. Patel, J. Debarbadillo, "Long term thermal stability of Inconel alloys 718, 706, 909 and Waspaloy at 593°C and 704°C", Ninth International Symposium on Superalloys (2000) 449-458.

[75] D. Mukherji, R. Gilles, B. Barbier, D.D. Genovese, B. Hasse, P. Strunz, T. Wroblewski, H. Fuess, J. Rösler, "Lattice misfit measurement in Inconel 706 containing coherent γ′ and γ″ precipitates", Scripta Materialia, 48 (2003) 333-339.

[76] A.J. Ardell, "The effect of volume fraction on particle coarsening: theoretical considerations", Acta Metallurgica, 20 (1972) 61-71.

[77] D.J. Chellman, A.J. Ardell, "The coarsening of γ' precipitates at large volume fractions", Acta Metallurgica, 22 (1974) 577-588.

[78] A.J. Ardell, V. Ozolins, "Trans-interface diffusion-controlled coarsening", Nat Mater, 4 (2005) 309-316.

[79] A.M. Ges, O. Fornaro, H.A. Palacio, "Coarsening behaviour of a Ni-base superalloy under different heat treatment conditions", Materials Science and Engineering: A, 458 (2007) 96-100.

[80] M.J. Donachie, S.J. Donachie, Superalloys: a technical guide, ASM international, 2002.

[81] R.F. Miller, G.S. Ansell, "Low temperature mechanical behavior of Ni-15Cr-Ai-Ti-Mo alloys", Metallurgical Transactions A, 8 (1977) 1979-1991.

[82] D.A. Grose, G.S. Ansell, "The influence of coherency strain on the elevated temperature tensile behavior of Ni-15Cr-AI-Ti-Mo alloys", Metallurgical Transactions A, 12 (1981) 1631-1645.

[83] M. Sundararaman, "The role of refractory metal additions in precipitation processes in superalloys", Mineral Processing and Extractive Metallurgy Review, 22 (2001) 681-700.
[84] W.E. Quist, R. Taggart, D.H. Polonis, "The influence of iron and aluminum on the precipitation of metastable Ni_3Nb phases in the Ni-Nb system", Metallurgical Transactions, 2 (1971) 825-832.
[85] J.K. Chakravartty, J.B. Singh, M. Sundararaman, "Microstructural and mechanical properties of service exposed Alloy 625 ammonia cracker tube removed after 100000 h", Materials Science and Technology, 28 (2012) 702-710.
[86] F. Long, Y.S. Yoo, C.Y. Jo, S.M. Seo, Y.S. Song, T. Jin, Z.Q. Hu, "Formation of η and σ phase in three polycrystalline superalloys and their impact on tensile properties", Materials Science and Engineering: A, 527 (2009) 361-369.
[87] C. T. Sims, N. S. Stoloff, W. C. Hagel, "Superalloys II", John Wiley & Sons (1987) 165-188.
[88] M.J. Donachie, S.J. Donachie, "Superalloys: a technical guide", ASM international (2002) 25-41.
[89] H. Eiselstein, "Metallurgy of a columbium-hardened nickel-chromium-iron alloy", in: Advances in the technology of stainless steels and related alloys, ASTM International, STP 369 (1965) 62-79.
[90] M. Sundararaman, P. Mukhopadhyay, S. Banerjee, "Precipitation of the δ-Ni_3Nb phase in two nickel base superalloys", Metallurgical transactions A, 19 (1988) 453-465.
[91] R. Moshtaghin, S. Asgari, "Growth kinetics of γ' precipitates in superalloy IN-738LC during long term aging", Materials & Design, 24 (2003) 325-330.
[92] H. Kitaguchi, "Microstructure-property relationship in advanced Ni-based superalloys", in: Metallurgy-advances in materials and processes, InTech Open, (2012)19-42.

[93] W. Sun, X. Qin, J. Guo, L. Lou, L. Zhou, "Thermal stability of primary MC carbide and its influence on the performance of cast Ni-base superalloys", Materials & Design, 69 (2015) 81-88.

[94] J.J. Ruan, N. Ueshima, K. Oikawa, "Phase transformations and grain growth behaviors in superalloy 718", Journal of Alloys and Compounds, 737 (2018) 83-91.

[95] P. Bala, J. Morgiel, G. Cios, K. Wieczerzak, T. Tokarski, "Ni-Cr-Ta-Al-C complex phase alloy – Design, microstructure and properties", Materials Science and Engineering: A, 711 (2018) 99-108.

[96] B. Hu, G. Trotter, Z. Wang, S. Chen, Z. Cai, I. Baker, "Effect of boron and carbon addition on microstructure and mechanical properties of the aged gamma-prime strengthened alumina-forming austenitic alloys", Intermetallics, 90 (2017) 36-49.

[97] J. Yang, Q. Zheng, X. Sun, H. Guan, Z. Hu, "Topologically close-packed phase precipitation in a nickel-base superalloy during thermal exposure", Materials Science and Engineering: A, 465 (2007) 100-108.

[98] Y.-H. Cheng, J.-T. Chen, R.-K. Shiue, L.-W. Tsay, "The evolution of cast microstructures on the HAZ liquation cracking of Mar-M004 weld", Metals, 8 (2018) 35.

[99] B. Du, L. Sheng, C. Cui, J. Yang, X. Sun, "Precipitation and evolution of grain boundary boride in a nickel-based superalloy during thermal exposure", Materials Characterization, 128 (2017) 109-114.

[100] O.P. Sinha, M. Chatterjee, V.V.R.S. Sarma, S.N. Jha, "Effect of residual elements on high performance nickel base superalloys for gas turbines and strategies for manufacture", Bulletin of Materials Science, 28 (2005) 379-382.

[101] M. Durand-Charre, "The microstructure of superalloys", CRC press, 1998.

[102] P. Kumar, "Role of niobium and tantalum in superalloys", in: Advances in high temperature structural materials and protective coatings, A.K. Koul, V.R. Parameswaran, J.-

P. Immarigeon, and W. Wallace, eds., National Research Council of Canada, Ontario (Canada), (1994) 73-94.

[103] M. Simonetti, P. Caron, "Role and behaviour of μ phase during deformation of a nickel-based single crystal superalloy", Materials Science and Engineering: A, 254 (1998) 1-12.

[104] B.J. Piearcey, F.L. VerSnyder, "A new development in gas turbine materials-The properties and characteristics of PWA 664", Journal of Aircraft, 3 (1966) 390-397.

[105] J.R. Mihalisin, D.L. Pasquine, "Phase transformations in nickel-base superalloys", Superalloys 1968, (1968) 134-170.

[106] B. Geddes, H. Leon, X. Huang, "Superalloys: alloying and performance", Asm International (2010) 25-48.

[107] G.E. Dieter, "Mechanical metallurgy", SI metric edition, McGraw-Hill, ISBN 0-07-100406-8 (1988) 184-240.

[108] P.B. Hirsch, F.J. Humphreys, "Plastic deformation of two-phase alloys containing small nondeformable particles", In: Physics of strength and plasticity (Ed. A. S. Argon). Cambridge, Massachusetts: MIT Press, (1969) 189-216.

[109] M.E. Bush, P.M. Kelly, "Strengthening mechanisms in bainitic steels", Acta Metallurgica, 19 (1971) 1363-1371.

[110] P.M. Kelly, "The effect of particle shape on dispersion hardening", Scripta Metallurgica, 6 (1972) 647-656.

[111] Z. Guo, W. Sha, "Quantification of precipitation hardening and evolution of precipitates", Materials transactions, 43 (2002) 1273-1282.

[112] K. Mills, J.R. Davis, J.D. Destefani, "ASM handbook: metallography and microstructures", vol. 9, ASM, Metals Park, OH, (2004).

[113] J. Rodrigues-Carvajal, "FULLPROF: a Rietveld refinement and pattern matching analysis program", Laboratoire Leon Brillouin, CEA-CNRS, France, (2000).

[114] E.H. Kisi, C.J. Howard, "Applications of neutron powder diffraction", Oxford University Press, (2012) 155-178.

[115] K.C. Russell, "Nucleation in solids: The induction and steady state effects", Advances in Colloid and Interface Science, 13 (1980) 205-318.

[116] D.A. Porter, K.E. Easterling, "Phase Transformations in Metals and Alloys", Second edition, Springer-Science+Business Media, B.Y., (1992) 185-262.

[117] Shabana Khan, S.D. Kaushik, A. Verma, J.B. Singh, V. Siruguri, D. Srivastava, "Lattice parameter instabilities during multi-phase precipitation in Alloy 693", Journal of Alloys and Compounds, 700 (2017) 149-154.

[118] E.W. Ross, C.T. Sims, "Nickel-base alloys", in: Superalloys II--High Temperature Materials for Aerospace and Industrial Power, A Wiley-Interscience publication, John Wiley and Sons, (1987) 97-133.

[119] G. Muralidharan, H. Chen, "Coarsening kinetics of coherent γ' precipitates in ternary Ni-based alloys: the Ni–Al–Si system", Science and Technology of Advanced Materials, 1 (2000) 51-62.

[120] W.B. Pearson, "The constitution and structure of nickel vanadium alloys in the region 0-60 at.% vanadium", Journal of the Institute of Metals, 80 (1952) 641-652.

[121] J.B. Singh, A. Verma, B. Paul, J.K. Chakravartty, "Failure of Alloy 625 tube stub ends – effect of primary nitrides", Engineering Failure Analysis, 32 (2013) 236-247.

[122] K.P. Gupta, "Phase diagrams of ternary Ni alloys- Part 1", in: Indian Institute of Metals Calcutta, India, 1990.

[123] G.V. Raynor, V.G. Rivlin, "Phase equilibria in iron ternary alloys: a critical assessment of the experimental literature", The Institute of Metals, London UK, (1988) 143-156.

[124] G. Kurdjumow, G. Sachs, "Über den mechanismus der stahlhärtung", Zeitschrift für Physik, 64 (1930) 325-343.

[125] G.R. Speich, R.A. Oriani, "Rate of coarsening of copper precipitate in an alpha-iron matrix", Transactions of the Metallurgical Society of AIME, 233 (1965) 623-631.

[126] E. Hornbogen, "Precipitation from binary substitutional solid solutions of α-Fe", in: Proceedings of a symposium 'Precipitation from Iron-Base Alloys', edited by G. R. Speich and J. B. Clark, (Met. Soc. Conf. No 28), (Amer. Inst. MM. Met. Eng.) New York, (1965).

[127] M. Tanino, T. Nishida, K. Aoki, "The crystallographic orientation relationship between Mo_2C and ferrite matrix", JAP INST METALS J, 30 (1966) 894-895.

[128] G.C. Weatherly, R.B. Nicholson, "An electron microscope investigation of the interfacial structure of semi-coherent precipitates", Philosophical Magazine, 17 (1968) 801-831.

[129] M.H. Jacobs, "The structure of the metastable precipitates formed during ageing of an Al-Mg-Si alloy", Philosophical Magazine, 26 (1972) 1-13.

[130] M.G. Hall, H.I. Aaronson, K.R. Kinsma, "The structure of nearly coherent fcc: bcc boundaries in a Cu-Cr alloy", Surface Science, 31 (1972) 257-274.

[131] R.W. Knights, P. Wilkes, "Precipitation of chromium in copper and copper-nickel base alloys", Metallurgical Transactions, 4 (1973) 2389-2393.

[132] D.R. Clarke, W.M. Stobbs, "The crystallography of phase interfaces in the unidirectionally solidified Cu-Cr eutectic alloy", MET SCI, 8 (1974) 242-246.

[133] Y. Komem, J. Rezek, "Precipitation at coherency loss in Cu-0.35 wt% Cr", Metallurgical Transactions A, 6 (1975) 549-551.

[134] K.A. Bywater, D.J. Dyson, "The Precipitation of Cr_2N in 17% Cr Steels", Metal Science, 9 (1975) 155-162.

[135] G.C. Weatherly, P. Humble, D. Borland, "Precipitation in a Cu-0.55wt.% Cr alloy", Acta Metallurgica, 27 (1979) 1815-1828.

[136] A. Crosky, P.G. McDougall, J.S. Bowles, "The crystallography of the precipitation of α rods from β Cu-Zn alloys", Acta Metallurgica, 28 (1980) 1495-1504.

[137] A. Crosky, P.G. McDougall, J.S. Bowles, "Relief effects associated with the precipitation of α rods from β Cu-Zn alloys", Acta Metallurgica, 31 (1983) 603-607.

[138] U. Dahmen, P. Ferguson, K.H. Westmacott, "Invariant line strain and needle-precipitate growth directions in Fe-Cu", Acta Metallurgica, 32 (1984) 803-810.

[139] T.J. Headley, J.A. Brooks, "A new bcc-fcc orientation relationship observed between ferrite and austenite in solidification structures of steels", Metallurgical and Materials Transactions A, 33 (2002) 5-15.

[140] E.C. Bain, N.Y. Dunkirk, "The nature of martensite", Trans. AIME, 70 (1924) 25-47.

[141] G. Wassermann, "Influence of the transformation of an irreversible Ni steel onto crystal orientation and tensile strength", Arch. Eisenhüttenwes, 16 (1933) 647.

[142] Z. Nishiyama, "X-ray investigation of the mechanism of the transformation from face centered cubic lattice to body centered cubic", Sci. Rep. Tohoku Univ, 23 (1934) 637-664.

[143] A.B. Greninger, A.R. Troiano, "The mechanism of martensite formation", Trans. AIME, 185 (1949) 590-598.

[144] W. Pitsch, "The martensite transformation in thin foils of iron-nitrogen alloys", The Philosophical Magazine: A Journal of Theoretical Experimental and Applied Physics, 4 (1959) 577-584.

[145] J.W. Christian, "Some comments on the Burgers and Bogers-Burgers transformation mechanisms and their relation to mathematical theories of martensite crystallography", Journal of the Less Common Metals, 28 (1972) 67-74.

[146] R.E. Smallman, A.H.W. Ngan, "Physical metallurgy and advanced materials", 7th ed., Butterworth-Heinemann, (2007) 385-446.

[147] D. Fournier, A. Pineau, "Low cycle fatigue behavior of inconel 718 at 298 K and 823 K", Metallurgical Transactions A, 8 (1977) 1095-1105.

[148] W.M. Garrison, N.R. Moody, "Ductile fracture", Journal of Physics and Chemistry of Solids, 48 (1987) 1035-1074.

[149] A. Das, "Fracture complexity of pressure vessel steels", Philosophical Magazine, 97 (2017) 3084-3141.

[150] A. Das, J.K. Chakravartty, "Fractographic correlations with mechanical properties in ferritic martensitic steels", Surface Topography: Metrology and Properties, 5 (2017) 045006.

[151] A. A. Griffith, "VI. The phenomena of rupture and flow in solids", Philosophical transactions of the royal society of london. Series A, containing papers of a mathematical or physical character, 221 (1921) 163-198.

[152] G.E. Dieter, "Mechanical metallurgy", SI metric edition, McGraw-Hill, ISBN 0-07-100406-8 (1988) 241-274.

[153] T.H. Courtney, "Mechanical behavior of materials", Waveland Press, (2005) 175-243.

[154] D. Raynor, J.M. Silcock, "Strengthening mechanisms in γ' precipitating alloys", Metal Science Journal, 4 (1970) 121-130.

[155] V. Munjal, A.J. Ardell, "Precipitation hardening of Ni-12.19 at.% Al alloy single crystals", Acta Metallurgica, 23 (1975) 513-520.

[156] C. T. Sims, N. S. Stoloff, W. C. Hagel, "Superalloys II", John Wiley & Sons (1987) 61-96.

[157] P. Veyssiere, J. Douin, P. Beauchamp, "On the presence of super lattice intrinsic stacking faults in plastically deformed Ni_3Al", Philosophical Magazine A, 51 (1985) 469-483.

[158] L.M. Brown, R.K. Ham, "Dislocation-particle interactions", In: A. Kelly and R.B. Nicholson (Eds.) Strengthening Methods in Crystals, Elsevier Publishing Company Ltd., Amsterdam, London, New York, (1971) 9-135.

[159] B. Reppich, "Some new aspects concerning particle hardening mechanisms in γ' precipitating Ni-base alloys—I. Theoretical concept", Acta Metallurgica, 30 (1982) 87-94.

[160] W. Huther, B. Reppich, "Interaction of dislocations with coherent, stree-free ordered particles", Zeitschrift fur Metallkunde, 69 (1978) 628-634.

[161] J.-H. Oh, I.-C. Choi, Y.-J. Kim, B.-G. Yoo, J.-i. Jang, "Variations in overall-and phase-hardness of a new Ni-based superalloy during isothermal aging", Materials Science and Engineering: A, 528 (2011) 6121-6127.

[162] J.B. Singh, J.K. Chakravartty, M. Sundararaman, "Work hardening behaviour of service aged Alloy 625", Materials Science and Engineering: A, 576 (2013) 239-242.

[163] M.P. Jackson, R.C. Reed, "Heat treatment of UDIMET 720Li: the effect of microstructure on properties", Materials Science and Engineering: A, 259 (1999) 85-97.

[164] H. Gleiter, E. Hornbogen, "Precipitation hardening by coherent particles", Materials Science and Engineering, 2 (1968) 285-302.

[165] R.E. Stoller, S.J. Zinkle, "On the relationship between uniaxial yield strength and resolved shear stress in polycrystalline materials", Journal of Nuclear Materials, 283 (2000) 349-352.